Positronium Ionisation in Collision with He Atoms.

A thesis submitted to the University of London for the degree of Doctor of Philosophy

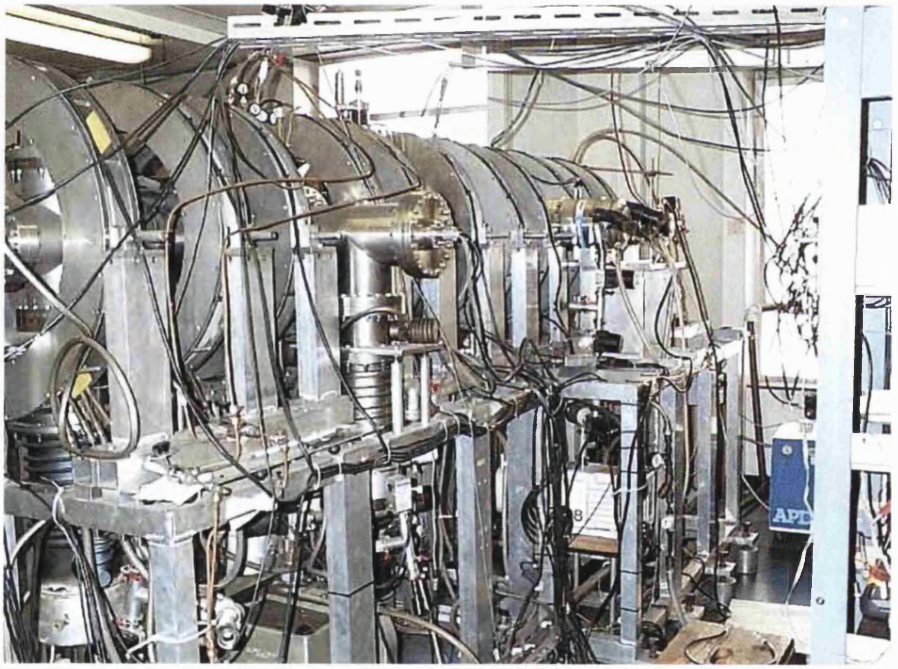

Simon Armitage

Department of Physics and Astronomy
University College London

May 2002

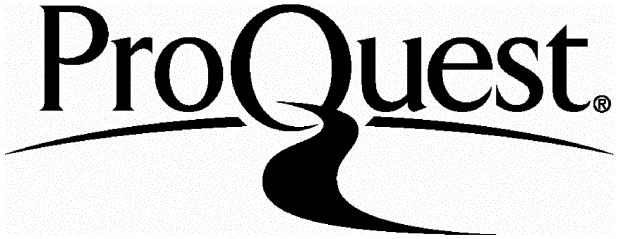

Abstract

Positronium is the lightest known atom, consisting of an electron and its antiparticle the positron. Because of its light mass (comparable with that of the electron and positron, rather than conventional atoms), recoil effects are expected to play an important role in its scattering from atomic and molecular targets. In Positronium the centres of charge and mass coincide, leading to a zero-static interaction and enhancing the relative importance of electron-exchange effects. Up until now, Positronium beam experiments have been restricted to total cross-section measurements from simple target atoms and molecules i.e. H_2, He and Ar. Significant discrepancies exist among various (theoretical and experimental) determinations of the Positronium-He total cross-section. In addition to their intrinsic interest, Positronium-atom partial-cross-sections are expected to provide a more sensitive test of our understanding of this collision system.

In this work, the ionisation cross-section of Positronium has been measured for the first time. A monoenergetic Positronium beam has been created through charge exchange of positrons in a gaseous target and positrons, originating from the break-up of positronium in collision with He atoms, have been detected with a time-of-flight system. Measurements are presented in the energy range 10 – 40eV and absolute break-up cross-section values have been achieved by measuring explicitly both the positron and Positronium detection efficiencies.

From the measured times-of-flight, longitudinal energy spreads of the residual positrons have also been obtained. The distributions have been found to be peaked at around 50% of the residual energy, suggesting a strong correlation between the residual particles.

The present work is expected to stimulate further theoretical and experimental activity in the study of Positronium-atom interactions. Possible future new directions are discussed.

CONTENTS

Figure	Caption	Page
	Chapter 1: Introduction	
1.1	*Feynmann diagrams for (a) one, (b) two, (c) three and (d) four photon decay modes.*	21
1.2	*The energy distribution of the γ-ray emission from o-Ps decay.*	23
1.3	*Energy level diagrams for H and Ps.*	24
1.4	*The decay scheme for ^{22}Na and ^{58}Co.*	25
1.5	*Energy distribution of β^+ particles emitted from a ^{58}Co radio-isotope.*	28
1.6	*The interaction of a high energy ($E \leq 100keV$) positron beam with the near-surface region of a solid (Schultz and Lynn, 1988).*	29
1.7	*Single-particle potential for a thermalised positron near a metal surface, where V_{corr} is due to the conduction electrons and V_0 is due to the ion cores.*	31
1.8	*The variation of the slow positron yield from Al and Cu, with changing positron work function, ϕ_+ (Murray and Mills, 1980).*	32
1.9	*Source and moderator geometries.*	33
1.10	*The triply differential electron spectrum for positron collision with H_2.* (a) *100eV incident positrons; hollow squares, experimental results, Kövér and Laricchia (1998); curves, theory of Berakdar et al (1998). Inset shows the experimental data on a linear plot.*	37

(b) 50eV incident positrons; circles, experimental results, Kövér et al (2001); curves, theory of Fiol et al (2000).

1.11 **38**

(a) Cross-section for excitation of the v_1 vibrational mode of CO, Full circles – experimental data, solid line – Gianturco et al (1997a), dot-dash line – Jain (1986) and dashed line – Jain multiplied by two.

(b) Cross-section for excitation of the v_2 and v_3 vibrational modes of CO_2, Open and closed circles – experimental data for v_2 and v_3 modes respectively, Solid and dashed line – Kimura et al (1998).

(c) Cross-section for excitation of the v_1 mode of H_2, Circles – experimental data, solid line – Sur and Ghosh (1985), dotted line – Baille and Darewych (1974) and dashed line – corrected theory of Gianturco and Murkerjee (1997).

1.12 **39**

(a) Integral cross-sections for the excitation of the $3p^5(^2P_{3/2,1/2})$ 4s states of Ar, open circles – 1/2 states, closed circles – 3/2 states.

(c) Integral cross-section for the sum of the two 4s (J=1) states of Ar, solid circles – trap data, open squares – Coleman et al (1982), open diamonds – Mori et al (1994) and dashed line – Parcell et al (2000).

1.13 **40**

(a) Integral cross-section for the excitation of the $B^1\Sigma$ state of H_2, solid circles – trap data, straight line – Murkherjee et al (1991) and dash line – Lino et al (1994).

(b)Integral cross-section for electronic excitation of N_2. Solid circles- $a'^1\Sigma$ and open circles - $A^1\Pi$.

1.14 **40**

Positron annihilation rate, Z_{eff}, for (a) butane, (b) propane and (c) ethane, as a function of positron energy. The vibrational modes are indicated by vertical lines along the abscissa.

Chapter 2: Equipment and Detection Systems

Chapter 3: Positronium Beam Techniques

Chapter 4: Positron and Positronium Detection Efficiencies

Chapter 5: Positronium Break-up in Collision with He Atoms

Chapter 4: Ps Detection Efficiency

Chapter 5: Ps Break-up in Collisions with He Atoms

Acknowledgements

I would like to thank a number of people who have helped, supported or put-up with me during my PhD years: Firstly to my supervisor, Dr Nella Laricchia for her guidance and endless enthusiasm. Thanks also to Dr Andrew Garner and Dr Aysun Özen for their assistance throughout my term. To all I have shared an office with, but in particular to Marta, Dawn and Vanita. To Ted Oldfield and Ivan Rangué for technical help and for making/repairing what I need, for when I want it. To all from F10 for providing suitable distractions. My family and friends for their endless support (financial and emotional) and a special final mention to my house-mates, Sue, Lucy, Elaine and Eamonn for putting up with me for all these (three-ish) years.

Chapter 1
Introduction

1.1 Historical Background

The prediction of the positron, the antimatter counterpart of the electron, was made by Dirac (1930a) through the solution of the relativistic wave equation used to describe the motion of free electrons in the presence of an electromagnetic field. This yielded both positive and negative energy solutions and Dirac interpreted the latter through his 'hole theory'. He proposed that the vacuum be considered as a totally filled sea of electrons occupying negative energy levels ($-m_0c^2$). Pauli's exclusion principle would then prevent electrons with positive energy from falling into the negative energy states. According to Dirac's theory, if an electron is excited from a negative energy level to a positive one, it leaves behind a 'hole', which would behave exactly like an electron but with a positive charge. Dirac initially considered this positive electron to be the proton, however it was later shown by Weyl (1931) that the mass of this particle had to be exactly the same as that of the electron.

The positron was first observed by Anderson (1932a, 1932b, 1933) in cosmic-ray tracks in a cloud chamber. Definitive identification came a year later when Blackett and Occhialini (1933) showed that the mass to charge ratio of the positron was of the same magnitude as that of the electron.

The Coulomb attraction between the positron and electron leads to the formation of a quasi-stable bound state known as positronium (Ps). The first quantum mechanical description of Ps was put forward by Ruark (1945), whilst Wheeler (1946) calculated its binding energy and lifetimes. The first observation of Ps was made by Deutsch (1951) through measurements of the positron lifetime in gases.

Positron emission from radio-isotopes has enabled a range of laboratory-based experiments. Early experiments were similar to electron swarm experiments in dense gases. The advent of monoenergetic positron beams have enabled comparative studies of positrons with electron, proton and anti-proton scattering from various targets, yielding information on the effect of mass, charge, electron exchange, polarisation and electron-capture process (see e.g. Knudsen and Reading, 1992 for a review). The characteristic annihilation radiation of positrons has been observed in solar flares and

emissions from the centre of our galaxy (Brown and Leventhal, 1987). Positron emission tomography (PET) is an established medical technique (e.g. Phelps *et al*, 1975) for dynamic imaging e.g. of blood flow and more recently, whole-body PET scans have become an accepted clinical tool for diagnosing cancer (Czernin and Brown, 2002).

In the following sections of this chapter, fundamental properties of positrons and positronium are described and an overview of experimental methods relevant to this work are introduced. Finally, recent positron-atom (molecule) scattering experiments are discussed and a review of the present status on Ps-atom (molecule) experiments is presented.

1.2 Fundamental Properties of Positrons and Positronium

1.2.1 Positrons

The positron is stable in vacuum, with a lifetime greater than 2×10^{22} years (Belloti *et al*, 1983). It has the same mass and spin as the electron, but opposite electrical charge and magnetic moment. A positron can annihilate with an electron, which, in terms of the 'hole theory', is equivalent to an electron in a positive energy state falling into a vacant negative energy state. The result is the emission of photons, the total energy of which, in their rest-frame, is equal to the total rest-mass energy of the positron/electron pair, i.e. 1.022MeV. The number of emitted photons is governed by the charge parity, P_c, of the annihilating system, which must be conserved through the annihilation process. As the charge parity of the photon is negative, for a system containing n photons:

$$P_c = (-1)^n. \tag{1.1}$$

By symmetry arguments Yang (1950) has shown that the charge parity of the electron-positron system is given by:

$$P_c = (-1)^{L+S}, \tag{1.2}$$

where L and S are the total orbital angular momentum and the total spin of the positron/electron system respectively. Hence, an odd or even number of annihilation photons is released depending on the total angular momentum of the positron/electron pair.

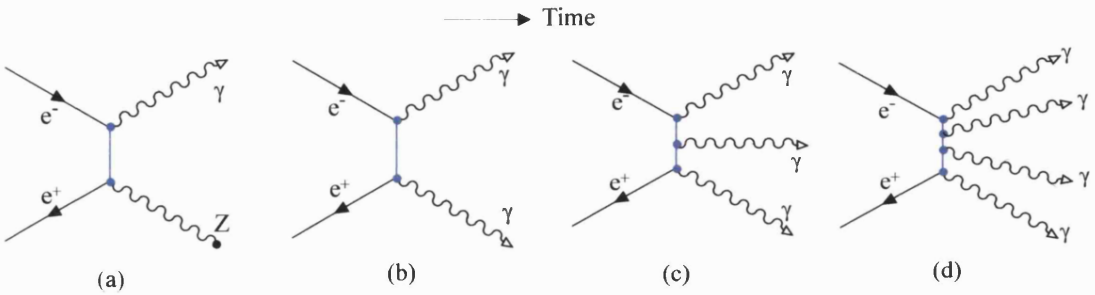

Figure 1.1 Feynmann diagrams for (a) one, (b) two, (c) three and (d) four photon decay modes.

In figure 1.1, Feynmann diagrams for annihilation resulting in one, two, three and four photons are shown. It should be noted that mode (a) requires the nearby presence of a third body (Z) to conserve momentum. The cross-section, for a given decay mode, is directly proportional to α^m, where $\alpha = e^2/2\varepsilon_0 hc \approx 1/137$ is the fine structure constant and m is the number of vertices in the corresponding Feynmann diagram. Therefore, the most probable mode of annihilation is into 2 photons, as one requires the presence of a third body and three has three corresponding vertices. All the decay modes shown in figure 1.1 have now been observed by: (a) Palathingal *et al* (1991), (b) Klemperer *et al* (1934), (c) Chang *et al* (1982 and 1985) and (d) Adachi *et al* (1990).

The cross-section for two photon annihilation of a non-relativistic positron with a free electron is given by Dirac (1930b) as

$$\sigma_{2\gamma}(e^-) = \frac{\pi r_0^2 c}{v}, \tag{1.3}$$

where c is the speed of light, v is the velocity of the positron with respect to the electron and $r_0 = e^2/(4\pi\varepsilon_0 m_0 c^2)$ is the classical electron radius. This equation has been adapted for positron annihilation in an atomic or molecular gas of number density n, as follows:

$$\sigma_{2\gamma}(A) = \frac{\pi r_0^2 c n Z_{eff}(v)}{v}, \tag{1.4}$$

where Z_{eff} is the effective number of electrons per atom/molecule available for annihilation with the positron (e.g. Heyland *et al*, 1982). In the energy range typically employed in positron scattering measurements, Bransden (1969) determined the two photon annihilation cross section to be on average of the order of $10^{-26}m^2$. Therefore, direct annihilation of the positron would be expected to be negligible in comparison to most other atomic processes, i.e. excitation, ionisation, etc.

1.2.2 Positronium

Positronium is the bound state of a positron and an electron and can be formed in two states, depending on the spin configuration of its constituent particles. Ortho-Ps (or o-Ps) comprises an electron and positron with parallel spins. Therefore, the total angular momentum (J=L+S) of ground-state o-Ps is 1, with three substates that arise from magnetic quantum numbers, m=0, ±1. Para-Ps (or p-Ps) is formed with an electron and positron of opposite spins and therefore has only one substate (m=0). Due to the relative number of substates for the two Ps spin states, formation of o-Ps is three times more likely than p-Ps. Characteristics for the two spins states are given in table 1.1.

	Ortho-Ps	***Para-Ps***
Ground state, spectroscopic terms	1^3S_1	1^1S_0
Sub-states	m=0,±1	m=0
Ground state decay rates (μs^{-1})	Exp: 7.0398±0.0029[a]	Exp: 7990.9±1.7[c]
	Theory: 7.0420[b]	Theory: 7989.5[d]

Table 1.1 Positronium properties, [a]Asai et al (1995), [b]Adkins et al (1992) and Mil'stein and Khriplovich (1994), [c]Al-Ramadhan and Gidley (1994) and [d]Khriplovich and Yelkhovskey (1990).

The Ps atom is unstable against annihilation and, in accordance with Equation 1.2, ground-state o-Ps (p-Ps) will decay into an odd (even) number of photons. As

stated, ground-state p-Ps decays into two photons with equal energies (~511keV) and is emitted back-to-back in the centre-of-mass frame. On the other hand, ground state o-Ps, at rest, decays into three coplanar photons with a distribution of energies from zero to 511keV. Figure 1.2 shows the energy distribution of the three coplanar photons from o-Ps decay, calculated by Ore and Powell (1949) and Adkins (1983), in comparison with the experimental determination of Chang *et al* (1985).

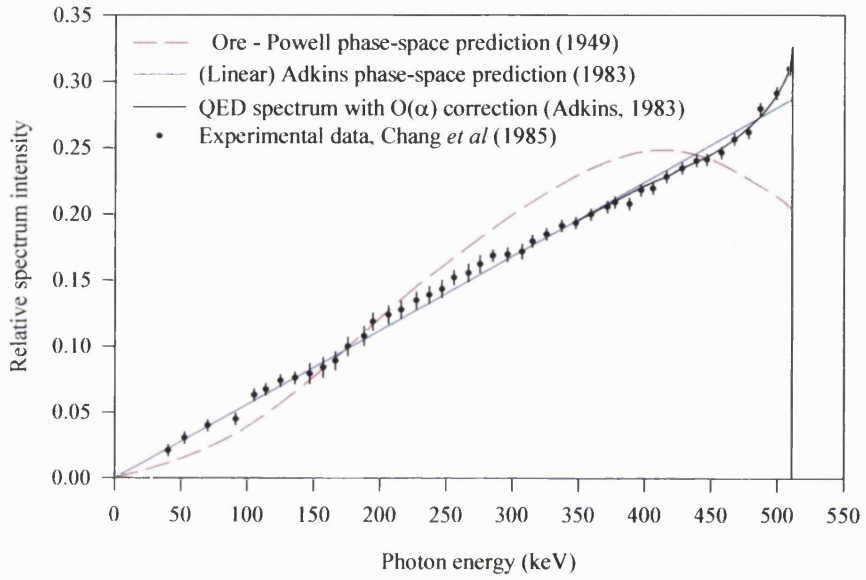

Figure 1.2 The energy distribution of the γ-ray emission from o-Ps decay.

Ps is structurally equivalent to H with half the reduced mass. Hence, it also has half of the binding energy (6.8eV) and twice the Bohr radius (1.05Å). Figure 1.3 shows a comparison of the energy levels for both H and Ps, calculated by Fulton and Martin (1954).

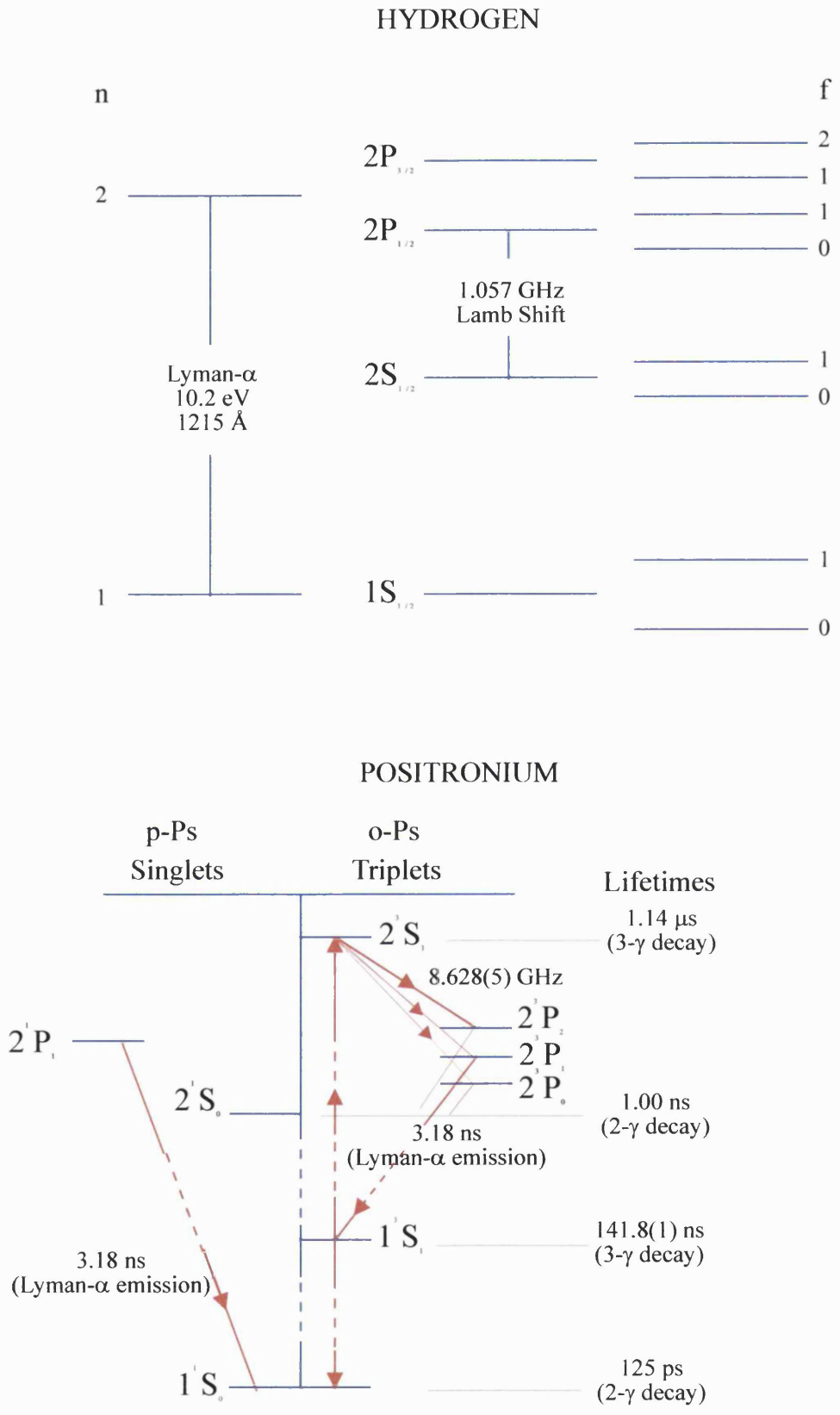

Figure 1.3 Energy level diagrams for H and Ps.

1.3 Early Techniques

Early experiments with positrons were based around immersing a positron-emitting isotope in solids, liquids and gases. The techniques most relevant to the present work involve the detection of the photons emitted through positron annihilation: firstly, a positron lifetime technique, utilizing a ^{22}Na source from which the 1.28MeV photon released following the emission of a β^+ particle is detected, in delayed coincidence with an annihilation photon; secondly, by measuring the angular deviation from co-linearity of the two γ-rays emitted upon positron annihilation, i.e. Angular Correlation of Annihilation Radiation (ACAR) and lastly, a Doppler broadening technique, based on the red/blue shift in the energy of the annihilation quanta. Each technique is described in more detail below.

1.3.1 Lifetime technique

Figure 1.4 shows the decay scheme for two radio-isotopes frequently used in positron lifetime studies.

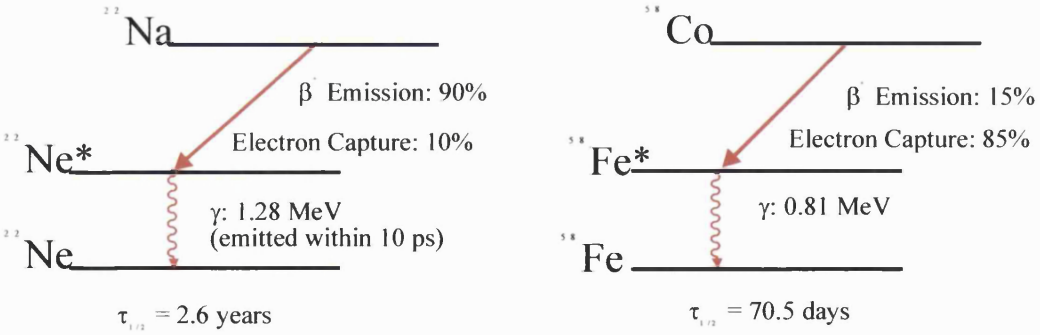

Figure 1.4 The decay scheme for ^{22}Na and ^{58}Co.

As can be seen from figure 1.4, in the case of ^{22}Na the emission of a β^+ particle is followed by the release of a 1.28MeV photon (0.81MeV for ^{58}Co). Lifetime spectra are obtained by utilizing this photon in coincidence with the annihilation photon from the positron in the sample under investigation. This technique was first introduced by Shearer and Deutch (1949) and since then has been used to gather a wealth of information on positron and positronium lifetimes in matter in all its phases. A concise summary of techniques applicable to positron annihilation in gases is given in Charlton (1985).

1.3.2 ACAR

The ACAR technique measures the angular deviation from co-linearity of two γ-rays emitted upon positron annihilation. Positrons emitted into a sample rapidly thermalise and annihilate with an electron, emitting two back-to-back γ-rays in the centre-of-mass frame. In the laboratory frame, the angle θ between the two γ-rays gives a measure of the momentum of the annihilating electron/positron pair and is given by

$$\theta = \frac{P_x}{mc}, \tag{1.5}$$

where P_x is the x-component of the centre-of-mass momentum and m and c are the positron mass and speed of light respectively. Relevant to the present work are the 2-D ACAR work of Coleman *et al* (1994), where Ps-atom elastic scattering cross-sections, σ_{el}, below 6.8eV have been determined for the noble gases. An empirical expression for the elastic scattering cross-section, i.e. $\sigma_{el} = (9\text{-}0.5E)\pi a_0^2$ where E is the energy, was found to be consistent with the experimental results for He, Ne and Ar. Nagashima *et al* (1998) used a 1-D ACAR technique to determine the momentum-transfer cross-section, σ_m, for Ps scattering from He (see section 1.7.2 for further discussion). A thermalisation model, which includes σ_m as an adjustable parameter, was utilised to obtain a value of $\sigma_m = (13\pm4)\ \pi a_0^2$ in the Ps energy range below 0.3eV.

1.3.3 Doppler Broadening

The γ-rays released through positron annihilation, in which the centre-of-mass of the electron-positron pair is at rest, each have energy of 511keV. However, the motion of the centre-of-mass gives rise to a Doppler shift in the γ-ray energies. The shift ΔE in the energy of the γ-rays is given by

$$\Delta E = mcv_{cm}\cos\phi, \tag{1.6}$$

where v_{cm} is the speed of the centre-of-mass of the electron/positron pair and ϕ is the angle between the direction of motion of the centre-of-mass and that of one of the γ-rays.

Positrons have a high affinity for trapping in open-volume defects. Consequently, the positron Doppler broadening technique is widely used for the analysis of composition and structure of materials (for a review see Van Veen *et al*, 1999 and references therein).

Rice-Evans *et al* (1992) have used this technique to investigate Ps formation from a carbon-oxygen interface. Iwata *et al* (1997) have utilised this method to measure γ-ray spectra from positron annihilation from atoms and molecules in traps. Noteworthy to the work described in this thesis are the time-resolved Doppler broadening measurements of Skalsey *et al* (1998), whereby an annihilation photon is observed in a single high-resolution Ge detector. The broadening here is a measure of the longitudinal momentum of the annihilating Ps atoms and timing information (provided by detection of the emitted β^+ particle) enables the determination of the correlation between the age and energy of Ps, in order to determine the momentum transfer cross-section (see section 1.5.3 for further discussion).

1.4 Slow Positron Beam Development

Although these early techniques continue to yield valuable information about positron and Ps interactions with matter, precise studies of energy dependent phenomena are impractical with them due to the large energy distribution of β^+ particles emitted from radio-isotopes. Figure 1.5 shows the energy distribution of β^+ particles emitted from a ^{58}Co source.

It was soon realised that in order to produce a beam of monoenergetic positrons, the use of a velocity selector would be inefficient in comparison with the yield of moderated positrons reemitted from some materials. In the next subsections, positron interactions with solids are briefly described and their role in the development of efficient moderators for slow positron beams discussed.

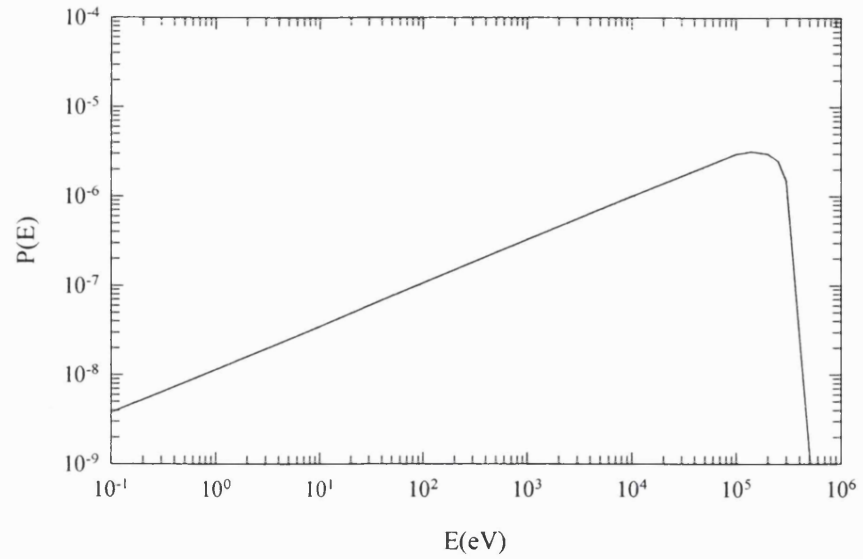

Figure 1.5 Energy distribution of β^+ particles emitted from a ^{58}Co radio-isotope.

1.4.1 Positrons in Solids

Figure 1.6 indicates the time scales associated with the possible interactions that a positron, implanted into a solid, can undergo.

When fast positrons are implanted into a solid, they rapidly lose energy initially via inelastic collisions to reach thermal equilibrium (within ~10ps). The implantation depth of β^+ particles emitted from a radioactive source is ~0.1mm in a defect-free metallic solid, compared with typical diffusion lengths of ~1000Å for a thermalised positron in one mean lifetime (Schultz and Lynn, 1988). Therefore, most of the positrons, which diffuse back to the metal surface, will be thermalised. If energetically allowed, these positrons may be emitted into the vacuum. The probability of emittance depends on the material bulk and surface properties. Once thermalised, the positron de Broglie wavelength (~60 Å at room temperature) is greater than the interatomic distances (typically a few Å). A thermalised positron therefore behaves like a propagating wave in the solid. Upon reaching the surface, the positron may become localised and annihilate or be emitted into the vacuum as a free positron or Ps. Table 1.2 summarises the time-scales for positron and Ps processes.

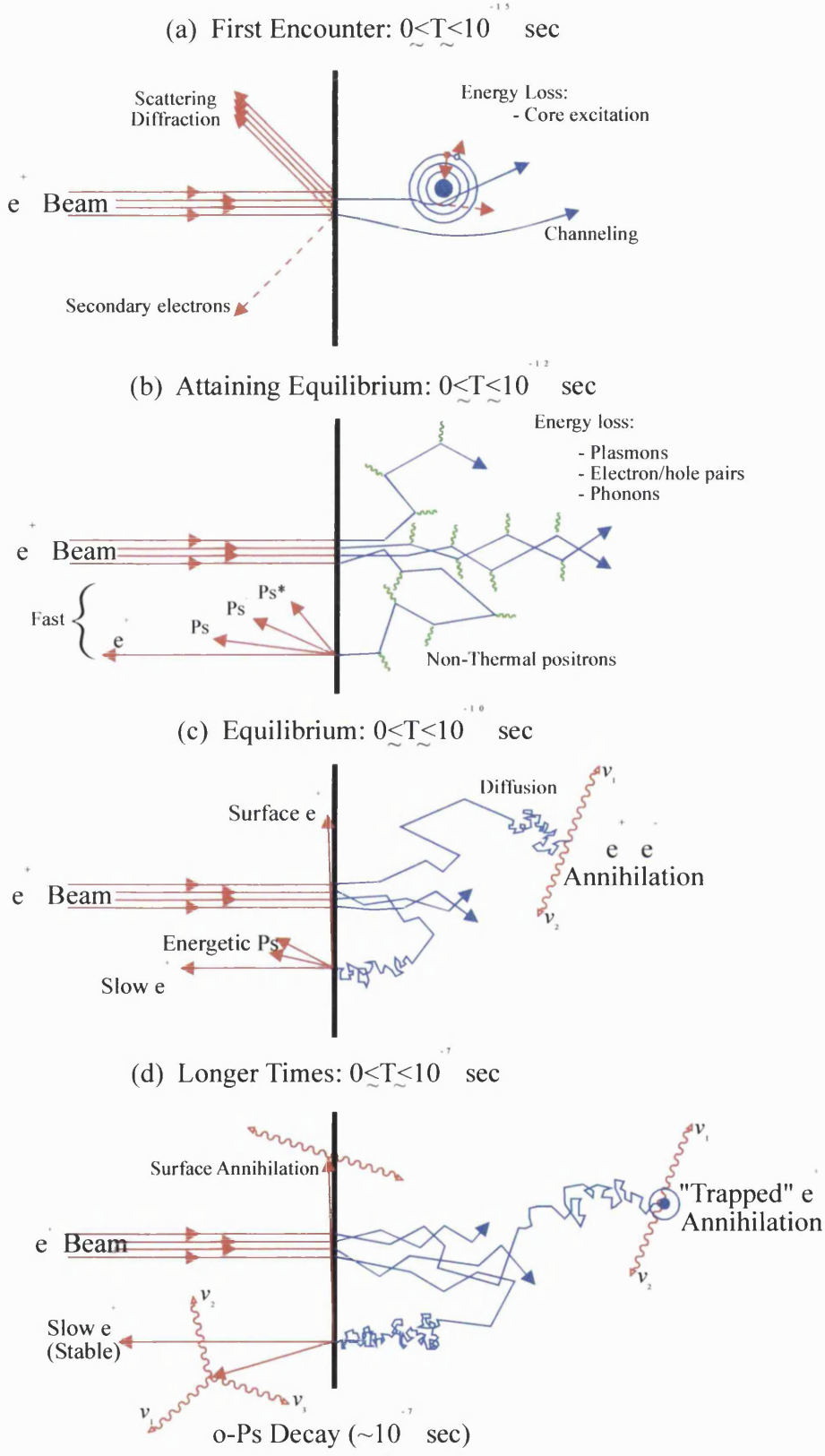

Figure 1.6 Illustration of he interaction of a high energy (E≤100keV) positron beam with the near-surface region of a solid (Schultz and Lynn, 1988).

Process	*Time*	*Reference*
Thermalisation	$\sim 10^{-12}$s	Perkins and Carbotte, 1970
Trapping (after thermalisation)	$\sim 10^{-15}$s	Hodges, 1970
Positron Lifetimes		
Freely diffusing	$\sim 1\times10^{-10}$s	West, 1973
Monovacancy trapped	$\sim 2\times10^{-10}$s	West, 1973
Multivacancy/void trapped	$\sim 4\times10^{-10}$s	Hautojärvi, 1979
Surface state	$\sim 4\text{-}6\times10^{-10}$s	Lynn *et al*, 1984 Kögel *et al*, 1988
Ps Lifetimes		
o-Ps, in solids	$\leq 10^{-9}$s	Dupasquier, 1981

Table 1.2 Time scales for positron and Ps in matter.

1.4.2 Positron Moderators

The positron diffusion studies of DeBenedetti *et al* (1950), Madansky and Rasetti (1950) suggested that it might be possible to create beams of slow positrons through thermalisation in solids. The first observation of moderated positrons was made by Cherry (1958) using a chromium-coated mica moderator bombarded with β^+ particles from a ^{64}Co source, who obtained an efficiency of 3×10^{-8}. Groce *et al* (1968) observed a peak in their time-of-flight spectra for positrons emitted from a mica sheet (coated with a 150Å-thick gold surface layer) with an energy of 1-2eV. Tong (1972) later explained this reemission phenomenon theoretically in terms of the negative work function for positrons.

The work function of a material is the minimum energy required to remove a positron/electron from a point inside, to one outside the bulk. Lang and Kohn (1971) defined the work function for an electron as:

$$\phi_- = \Delta\varphi - \mu_-, \tag{1.7}$$

where $\Delta\varphi$ is the surface dipole and μ_- is the bulk chemical potential of the electrons with respect to the mean electrostatic potential in the metal. The surface dipole is

caused by the tailing of the conduction electron gas from the bulk and the net positive ion-core potential.

The positron work function, ϕ_+, was defined by Tong (1972) as:

$$\phi_+ = -\Delta\varphi - \mu_+, \tag{1.8}$$

where μ_+ is the positron bulk chemical potential (ion-core potential and correlations with the electron gas), and the surface dipole, $-\Delta\varphi$, is equal and opposite to the electron surface dipole. Positron emission from a surface is energetically allowed for negative values of ϕ_+. The potentials, which a thermalised positron experiences close to a metal surface, are shown in figure 1.7.

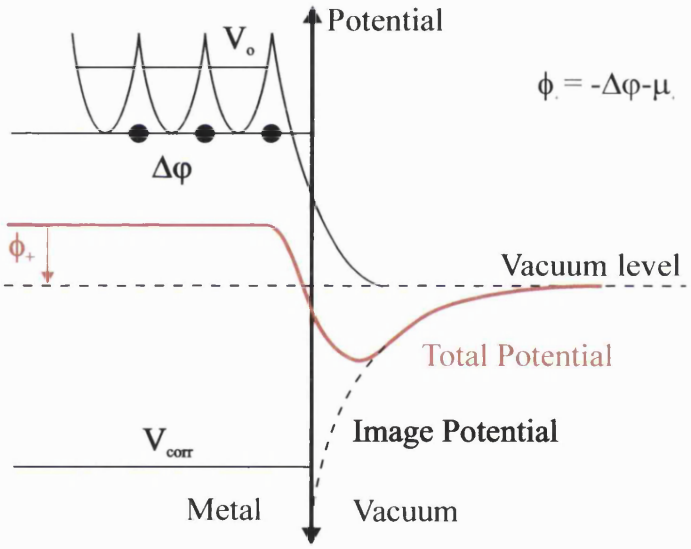

Figure 1.7 Single-particle potential for a thermalised positron near a metal surface, where V_{corr} is due to the conduction electrons and V_0 is due to the ion cores.

High purity samples were first systematically studied as moderators by Mills *et al* (1978). They found that variation in the moderator temperature resulted in a change in the slow positron yield. Murray and Mills (1980) measured the positron moderation efficiency of Al and Cu for various values of the work function, ϕ_+. This variation was realised by controlling the temperature, surface coverage of S atoms and the orientation of the crystal lattice. From the results shown in figure 1.8, it can be seen that as the magnitude of the negative positron work function increases, so does the yield of slow positrons.

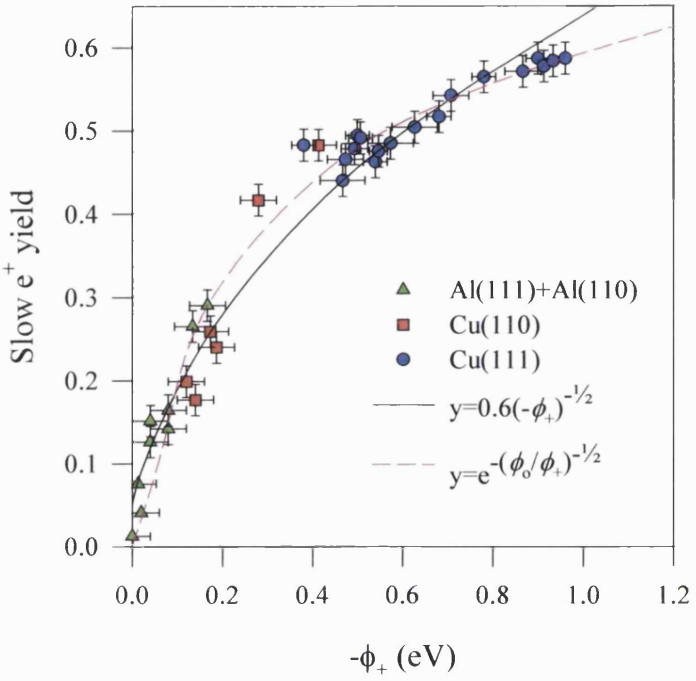

Figure 1.8 The variation of the slow positron yield from Al and Cu, with changing positron work function, ϕ_+ (Murray and Mills, 1980).

Dale *et al* (1980) found that annealing a moderator increased the moderator efficiency. Polycrystalline W vanes were found to be the most efficient after being chemically etched and heated to 2200^0C. The increase in the slow positron yield was attributed to two processes that occurred due to annealing. Firstly, the heat treatment reduces the concentration of lattice defects, which may act as positron traps, allowing more thermal positrons to diffuse to the surface. Secondly, for W moderators, the annealing process serves to extract the majority of adsorded O from the surface.

In 1986, Gullikson and Mills discovered that rare gas solids, RGS (Ne, Ar, Kr and Xe), are very effective β^+ particle moderators because of the slow thermalisation process once below the band gap energy of the solid. Hence, the only mechanism for positron energy loss is through phonon excitation, which removes only a few meV per collision and thus leads to a large positron diffusion length in the RGS. In practice, this process results in a considerable amount of epi-thermal positrons reaching the moderator surface from where they may escape into the vacuum.

The geometry of the source and moderator arrangement greatly affects the efficiency of the positron beam. Figure 1.9 shows examples of the principal arrangements used for moderating β^+ particles.

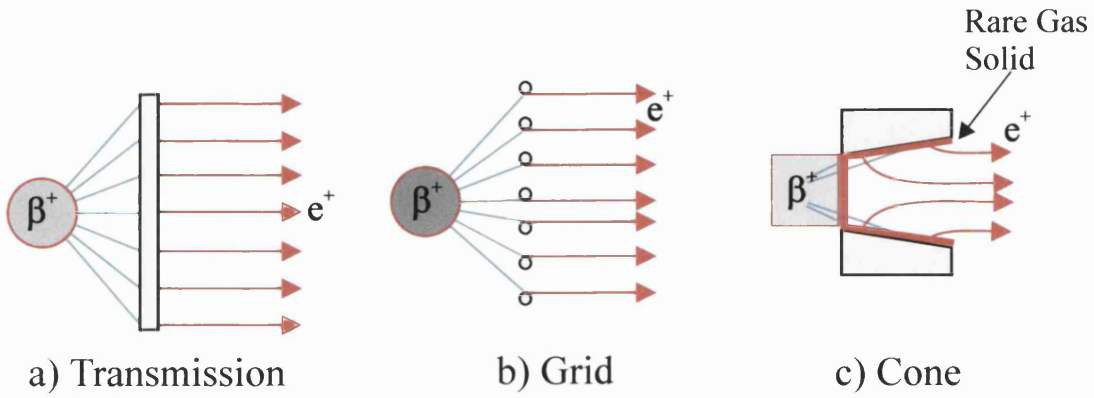

Figure 1.9 Source and moderator geometries.

In the transmission geometry, positrons are extracted from the surface opposite to that of implantation, as illustrated in figure 1.9 (a). Single crystal moderators of thickness 10^3-10^4 Å may be used in this mode. In 1989, Zafar *et al* obtained an efficiency of 6.5×10^{-4} and an energy spread of 0.3eV from a single-crystal Ni(100) moderator. Jacobsen *et al* (1990), investigated the slow positron reemission probability from thin W(100) films, where the moderators were laser annealed. In this way, they attained an energy distribution of 0.15-0.3eV.

Figure 1.9 (b) depicts the grid moderator geometry. In this mode, the positrons are reemitted from the same side as entered by the β^+ particles. With this geometry, there are large open areas through which the β^+ particles can be transmitted and the slow positrons extracted. From these moderators, the positrons may be emitted from surfaces that are not perpendicular to the beam axis, which results in a larger angular distribution than from flat single crystal moderators.

The moderator geometry for a rare-gas solid moderator is shown in figure 1.9 (c). In principle, rare-gas solid moderators can be made by freezing the respective moderator directly onto the surface of the source of β^+ particles. It has been shown however, that rare-gas solid moderators in conical and parabolic configurations give the highest moderation efficiencies (Khatri *et* al, 1990 and Greaves and Surko, 1996).

Table 1.3 lists the key landmarks in the development of moderators from 1950 to the present date.

Moderator and Mode	***Moderation Efficiency***	***Energy Spread ΔE (eV)***	***References***
Pt, K, Ga, glass - transmission	0	-	Madansky and Rasetti, 1950
Cr Plated mica - transmission	3×10^{-8}	-	Cherry, 1958
Au plated mica - transmission	10^{-7}	2	Costello *et al,* 1972a
MgO coated Au vanes - backscattering	3×10^{-5}	2.3	Canter *et al,* 1972
B - self-moderator	10^{-7}	0.15	Stein *et al,* 1974
Al(100) - backscattering	3×10^{-5}	0.1	Mills *et al*, 1978
Cu(111)+H_2S- backscattering	1.5×10^{-3}	0.6	Mills, 1980
W vanes - backscattering	7×10^{-4}	1.3	Dale *et al,* 1980
W(110) - backscattering	3×10^{-3}	0.7	Vehanen *et al,* 1983
W(100) - transmission	4×10^{-4}	3	Lynn *et al*, 1985
Ne -transmission/backscattering	7×10^{-3}	0.58	Mills and Gullikson, 1986
W(100)	9×10^{-4}	-	Gramsch *et al*,
Ni(100) -transmission	6.6×10^{-4}	-	1987
W, Ni cone- backscattering	1.5×10^{-3}, 1.0×10^{-3}	-	Lynn *et al*, 1989
Ar -field assisted transmission	6×10^{-3}	-	Merrison *et al*,
Kr -field assisted transmission	6×10^{-3}	-	1992
Ne, parabolic cup - transmission/backscattering	5×10^{-3}	~1.9	Greaves and Surko, 1996
Ar, cone cup - transmission/backscattering	9.5×10^{-4}	-	Jääskelainen *et al*, 1997

Table 1.3 A summary of the positron moderator development.

An alternative method of increasing the slow positron flux is to increase the number of β^+ particles which are incident upon the moderator. This can be done by using sources of very high specific activity, such as ^{64}Cu (Lynn and Jacobsen, 1994). Properties of isotopes, used in positron experiments, are given in table 1.4.

Isotope	*Half-Life*	*β^+ fraction (%)*	*Maximum specific activity (Cig^{-1})*
^{58}Co	71 days	15	16.6
^{22}Na	2.6 yrs	90	1.25
^{64}Cu	12.8 hrs	19	600
^{68}Ge	288 days	88	6
^{11}C	20 min	99	-

Table 1.4 Properties of some β^+ emitting isotopes (Dupasquier and Zecca, 1985).

The most common radio-isotope used in laboratory-based experiments is ^{22}Na due to its large branching ratio, but predominantly due to its relatively long half-life.

1.5 Positron and Positronium Interactions with Atoms and Molecules

In this section, positron and Ps interactions with atoms and molecules are discussed. Particular attention is given to studies related to this work and to recent developments in the field of positron physics.

1.5.1 Positron Interactions with Atoms and Molecules

Since the realisation of slow positron beams, a wide range of atomic processes have been studied, such as: elastic scattering, excitation, Ps formation and ionisation. Slow positron beam interactions with atoms and molecules have been reviewed by Laricchia and Charlton (1999) and, more recently, by Charlton and Humberston (2001) and Laricchia (2002). Table 1.5 summarises the status on experimental studies for positron collisions with atoms and molecules.

Interaction	*Experimental Status*
Total cross-section $e^+ + A \rightarrow all$	σ_T for many atomic and molecular targets, including H, He, alkali and Mg.
Elastic scattering $e^+ + A \rightarrow e^+ + A$	Some σ_{el} and $d\sigma_{el}/d\Omega$.
Electron capture $e^+ + A \rightarrow Ps + (z-1)e^- + A^{z+}$	σ_{Ps} between 1 and 100eV, including H, alkali, Mg; some $d\sigma_{Ps}/d\Omega$
Target excitation $e^+ + A \rightarrow e^+ + A^*$	First state-resolved σ_{ex} for electronic and vibrational excitations.
Direct ionisation $e^+ + A \rightarrow e^+ + ze^- + A^{z+}$	σ_I^{z+} for 1 to 1000eV; including H, some $d\sigma_I^+/d\Omega$, $d^2\sigma_I^+/d\Omega_1 dE_i$ and first $d^3\sigma_I^+/d\Omega_1 d\Omega_2 dE_i$
Annihilation $e^+ + A \rightarrow 2\gamma + A^+$	First energy dependent measurements.
Formation of compounds $e^+ + A \rightarrow (PsC) + D^+$	Only PsH observed – failed search for PsCl and PsF.

Table 1.5 Status on experimental collision studies with positrons (Laricchia, 2002).

Kövér and Laricchia (1998) have reported the first measurements of $d^3\sigma_I^+/d\Omega_1 d\Omega_2 dE_i$, the triple differential cross-section, for 100eV positrons from molecular Hydrogen. A small peak was observed close to 42eV in the ejected-electron-energy-spectrum, see figure 1.10 (a), corresponding to both the electron and positron being emitted at small angles to the forward direction. This phenomenon arises from the Coulomb attraction between the two outgoing particles in the final state and is known as electron-capture-to-the-continuum (ECC) or, in the positron case, also as Ps formation in the continuum. The work was extended to 50eV positrons by Kövér *et al* (2001), see figure 1.10 (b), where a shift of –1.6eV is seen in comparison with a theory by Fiol *et al* (2001) which does not include the molecular structure of the target.

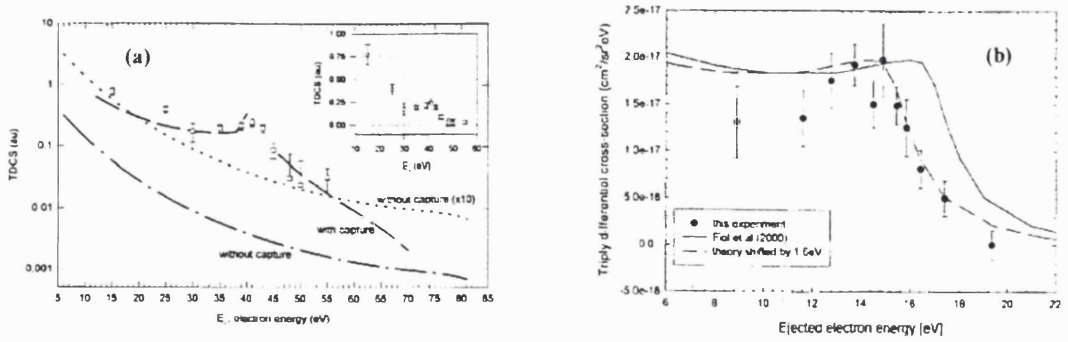

Figure 1.10 The triply differential electron spectrum for positron collision with H_2.

(a) 100eV incident positrons; hollow squares, experimental results, Kövér and Laricchia (1998); curves, theory of Berakdar et al (1998). Inset shows the experimental data on a linear plot.

(b) 50eV incident positrons; circles, experimental results, Kövér et al (2001); curves, theory of Fiol et al (2000).

Absolute cross-sections for the vibrational excitation of CO, CO_2 and H_2 by positron impact have been determined in the energy range 0.5eV (Sullivan *et al,* 2001a) to several electronvolts. The measurements use a novel technique that exploits the adiabatic motion of a positron beam in a strong magnetic field, where the translational energy of the scattered positron beam is measured using a retarding field analyser. Figure 1.11 (a) shows the vibrational excitation cross-section for positron collisions with CO. There is excellent agreement with the calculations of Gianturco *et al* (1997a), who suggested that the sharp onset, from threshold, might be due to the presence of an e^+-CO resonance, while the calculations of Jain (1986) are lower by a factor of approximately two. Figure 1.11(b) shows the cross section for excitation of the v_2 and v_3 modes of CO_2 at 0.08 and 0.29eV respectively. The data are compared to the calculations of Kimura *et al* (1998) where an excellent agreement is found for the v_3 mode, at energies where a comparison is possible. The cross section for vibrational excitation of H_2 are much lower than for CO and CO_2, which is suggested to be due to the lack of dipole coupling to the mode in H_2, see figure 1.11(c). The experimental data are in good agreement with the calculations of Sur and Ghosh (1985).

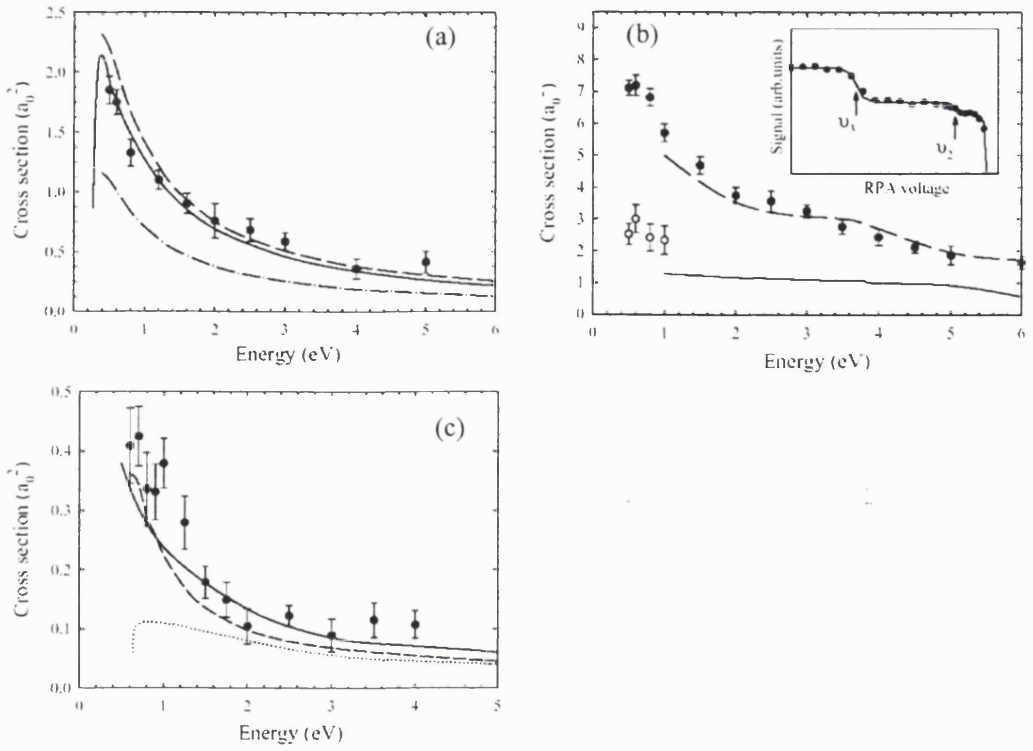

Figure 1.11

(a) Cross-section for excitation of the v_1 vibrational mode of CO, Full circles – experimental data, solid line – Gianturco et al (1997a), dot-dash line – Jain (1986) and dashed line – Jain multiplied by two.

(b) Cross-section for excitation of the v_2 and v_3 vibrational modes of CO_2, Open and closed circles – experimental data for v_2 and v_3 modes respectively, Solid and dashed line – Kimura et al (1998).

(c) Cross-section for excitation of the v_1 mode of H_2, Circles – experimental data, solid line – Sur and Ghosh (1985), dotted line – Baille and Darewych (1974) and dashed line – corrected theory of Gianturco and Murkerjee (1997).

The first state-resolved, absolute cross-sections for positron excitation of electronic states of an atom or molecule have been made using the retarding field analyser technique developed by Sullivan *et al* (2001b). Figure 1.12(a) shows the measured cross-section for the two excited 4s (J=1) states of Ar. The cross-sections are small, but similar in magnitude to their electron scattering counterparts (Chutjian *et al*, 1981). In figure 1.12(b) the sum of the cross-sections for the two 4s (J=1) states are shown and are compared with two previous measurements (Coleman *et al,* 1982 and Mori *et al*, 1994). A comparison is made to the LS-coupling calculation of Parcell

et al (2000), which provides a reasonable estimate of the magnitude of the summed cross-section at around 17eV, but is approximately 50% higher than the trap experiment at 30eV.

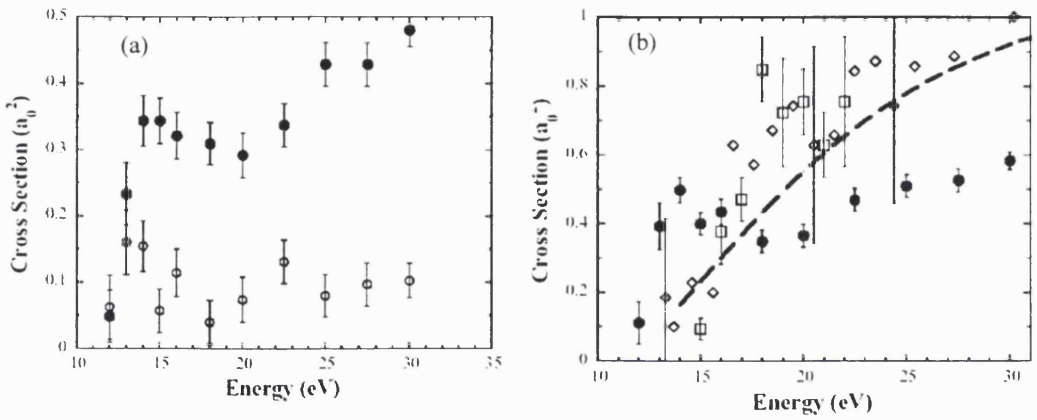

Figure 1.12

(a) Integral cross-sections for the excitation of the $3p^5(^2P_{3/2,1/2})$ 4s states of Ar, open circles – 1/2 states, closed circles – 3/2 states.

(c) Integral cross-section for the sum of the two 4s (J=1) states of Ar, solid circles – trap data, open squares – Coleman et al (1982), open diamonds – Mori et al (1994) and dashed line – Parcell et al (2000).

The cross-section for the $B^1\Sigma$ state of H_2 is shown in figure 1.13(a). The cross-section rises relatively slowly from threshold to a maximum value of about $1.5a_0^2$ near 20eV. Also shown in figure 1.13(a) are two theoretical calculations for this process, one a close-coupling (CC) approach (Murkherjee *et al,* 1991) and the other using a Schwinger multichannel (SMC) theory (Lino *et al,* 1994). The trap measurements are in reasonably good agreement with the SMC calculation, which in turn, places them a factor of 5-10 below the CC cross section.

Figure 1.13 (b) shows the cross-section for the excitation of the $a'^1\Sigma$ and $A^1\Pi$ states of N_2 at energies up to 20eV. There are no theoretical calculations for comparison, however, in both cases the near-threshold cross-sections are larger by approximately a factor of two than their electron counterparts (Campbell *et al*, 2001).

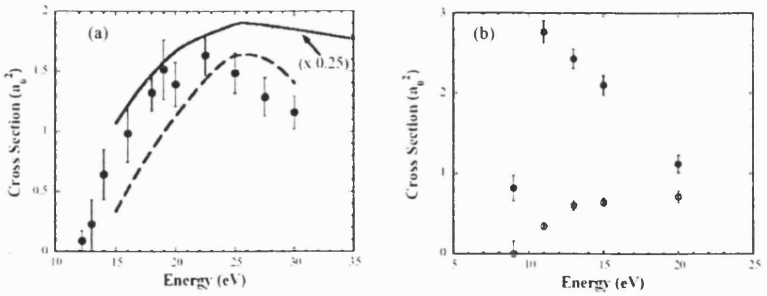

Figure 1.13

(a) Integral cross-section for the excitation of the $B^1\Sigma$ state of H_2, solid circles – trap data, straight line – Murkherjee et al (1991) and dash line – Lino et al (1994).

(b)Integral cross-section for electronic excitation of N_2. Solid circles- $a'^1\Sigma$ and open circles - $A^1\Pi$.

The first energy-resolved measurements for the annihilation rate of low-energy positrons in molecules, have been performed by Gilbert *et al* (2002). Figure 1.14 shows the positron annihilation rate, Z_{eff}, for butane, propane and ethane as a function of positron energy. For all the alkane molecules, a large annihilation signal in the region of the molecular vibrational modes is seen, suggesting the importance of vibrational resonances in producing large Z_{eff} values.

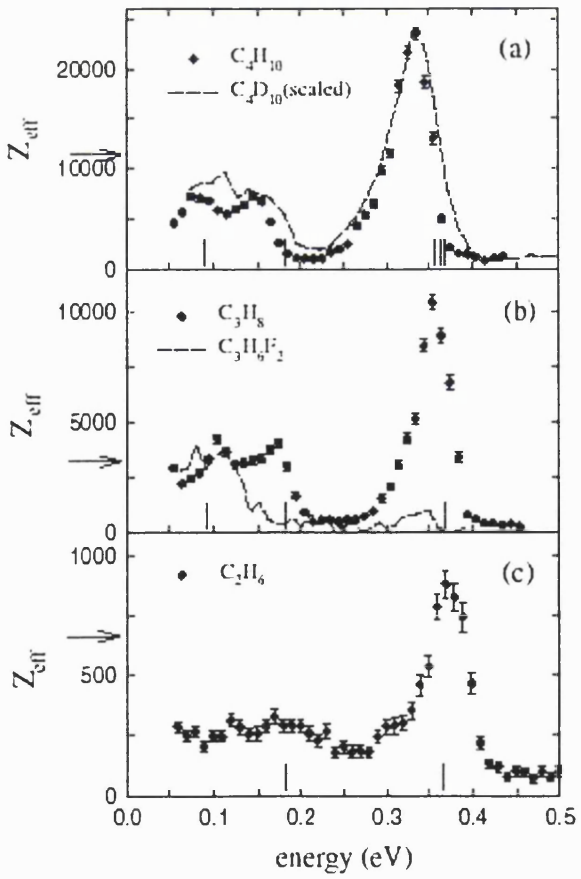

Figure 1.14

Poitron annihilation rate, Z_{eff}, for (a) butane, (b) propane and (c) ethane, as a function of positron energy. The vibrational modes are indicated by vertical lines along the abscissa.

1.5.2 Development of Ps Beams

Ps can be formed by neutralizing a positron beam in a gaseous target, A, via the charge exchange reaction

$$e^+ + A \rightarrow Ps + A^+. \tag{1.9}$$

The Ps kinetic energy, E_{Ps}, is given to a first approximation (Laricchia *et al*, 1992) by,

$$E_{Ps} = E_{e^+} - I + B, \tag{1.10}$$

where I is the ionisation potential of the target atom/molecule and $B = 6.8/n^2$eV is the Ps binding energy of a Ps atom in a state of principle quantum number n.

The Ps beam production efficiency, ε_{Ps}, depends on the relative magnitudes of the Ps formation cross-section, σ_{Ps}, and the total cross-sections for both positron and Ps scattering (Laricchia *et al*, 1992) according to the following expression,

$$\varepsilon_{Ps} \propto \{1 - \exp(-\rho l_+ \sigma_{T+})\}\left\{\frac{1}{\sigma_{T+}} \int_0^{\theta'} \frac{d\sigma_{Ps}}{d\Omega} \sin\theta d\theta\right\} \exp(-\rho l_{Ps} \sigma_{TPs}), \tag{1.11}$$

where the subscripts + and Ps denote quantities relevant to positrons and Ps respectively. The first term in Equation 1.11 is the fraction of scattered positrons, the second term is the Ps formation probability within a solid angle Ω' and the last term is the Ps transmission probability through a target of density ρ and length l_{Ps}. The first production of energy tuneable Ps was observed by Brown (1985, 1986), who identified the Doppler shifted annihilation γ-rays of p-Ps formed in collision with He atoms. Two annihilation spectra, for Ps energies of 35eV and 55eV, are shown in figure 1.15.

Monoenergetic tunable beams of o-Ps were first produced by Laricchia *et al* (1986, 1987) from charge-exchange collisions with He and Ar atoms. These results were extended by Zafar *et* al (1991), whereby ground and excited states of Ps were resolved from positron collisions with He and Ar atoms and Garner *et al* (1996), who

systematically measured the Ps beam production efficiency for a number of targets, pressures and Ps energies.

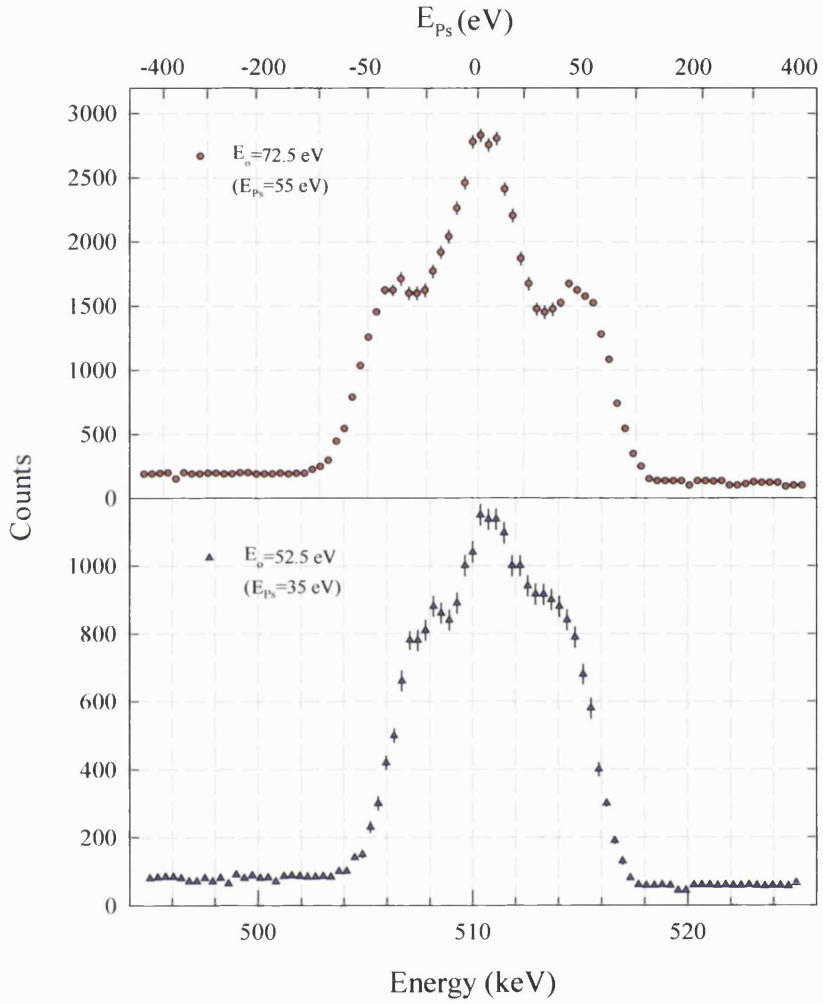

Figure 1.15 Annihilation spectra showing monoenergetic Ps formed in He (Brown, 1986).

The Ps beam production efficiency, ε_{Ps}, is given by:

$$\varepsilon_{Ps} = \frac{N_{Ps}}{\Omega N_{e^+}} D, \tag{1.12}$$

where N_{Ps} and N_{e^+} are the number of o-Ps atoms and incident positrons respectively. D corrects for the in-flight decay of Ps and Ω takes into account the detection solid angle. The results for ε_{Ps} from Ar, He and H_2 are plotted in figure 1.16 versus gas

pressure and Ps energy (Garner *et al*, 1996). At 30eV, H_2 is found to be the most efficient converter gas by a factor of ~2. With increasing energy, the efficiency of Ar and He tend to that of H_2 and at 90eV all three gases give approximately the same efficiency. At 120eV Ar is the most efficient converter by about 40%. In most cases ε_{Ps} reaches saturation with increasing gas pressure, as previously observed (Zafar *et* al, 1991 and Laricchia *et al*, 1992). This feature arises from the competition between the formation of Ps and its scattering from the neutralizing gas, according to Equation 1.11. Hence, the plateau region is less noticeable in He due to its Ps total cross-section being 2-4 times less than for the other converter gases.

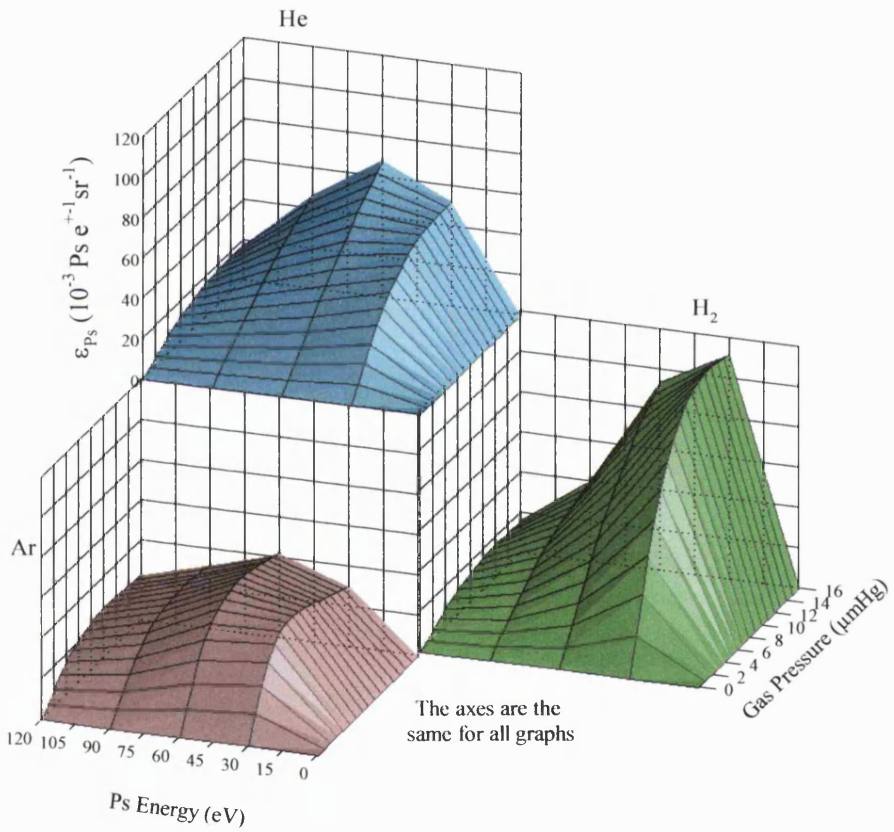

Figure 1.16 Ps beam production efficiencies from H_2, He and Ar.

H_2 was chosen as the positron converter gas in this work, as it is the most efficient positron to Ps converter gas across the Ps energies required for this study (0-40eV).

1.5.3 Scattering of Ps

Table 1.6 shows some of the processes available to Ps in collision with atoms and molecules.

Interaction	Experimental status
Total cross-section $Ps + A \rightarrow all$	Direct measurements for He, Ar, H_2 and O_2. Some indirect.
Ps elastic scattering $Ps + A \rightarrow Ps + A$	Coleman et al (1994), Nagashima et al (1998), Skalsey et al (1998), limited energy range.
Ps Ionisation $Ps + A \rightarrow e^+ + e^- + A$	This study.
Ps excitation $Ps + A \rightarrow Ps^* + A$	None.

Table 1.6 Some of the processes available to Ps in collision with atoms and molecules.

In this subsection, the total cross-sections, σ_T, for Ar, H_2 and He measured with the Ps beam (using the method described in section 3.3) are compared with available theories and alternative experimental determinations. The total cross-sections measured with the beam show the same general trend with energy for all three gases, namely a rapid increase, thought to be due to Ps break-up, followed by a broad maximum and then a slow decrease at higher energies. As stated in section 1.3.2, Coleman *et al* (1994) have measured the elastic cross-section, but as pointed out by Blackwood *et al* (2002) their measurement more accurately reflects the momentum-transfer-cross-section, σ_m, that is obtained from the differential-elastic-cross-section. Due to the large number of assumptions made in extracting their cross-section, Coleman *et al* have advised that their results should only be used as a guide.

The σ_T from Ar obtained with the Ps beam is shown in figure 1.17, compared with theory and alternative experiments. In Ps-Ar scattering, the coupled pseudostate calculations by McAlinden *et al* (1996) do not agree with experiment in shape nor magnitude, except at the highest energies. The results of a 22-state frozen

target approximation of Blackwood *et al* (2002), whilst intercepting the beam data around 20eV, show an upturn in the cross-section at lower energies much smaller than the experimental peak.

The low-energy coupled-channel calculations by Biswas and Adhikari (2000) are in excellent agreement with the 2-D ACAR measurement by Coleman *et al* (1994) and the Doppler broadening measurement by Skalsey *et al* (1998) for σ_m. It should be noted that at sufficiently low energies, where the scattering is purely *S*-wave, σ_m is the same as the elastic-cross-section and therefore σ_T. At increasing energies σ_m deviates from σ_{el}, up to 70% by 1eV (Blackwood *et al*, 2002). Hence, without knowledge of the energy dependence of σ_m, detailed comparison between measurements at different energies is highly speculative (Skalsey *et al*, 1998).

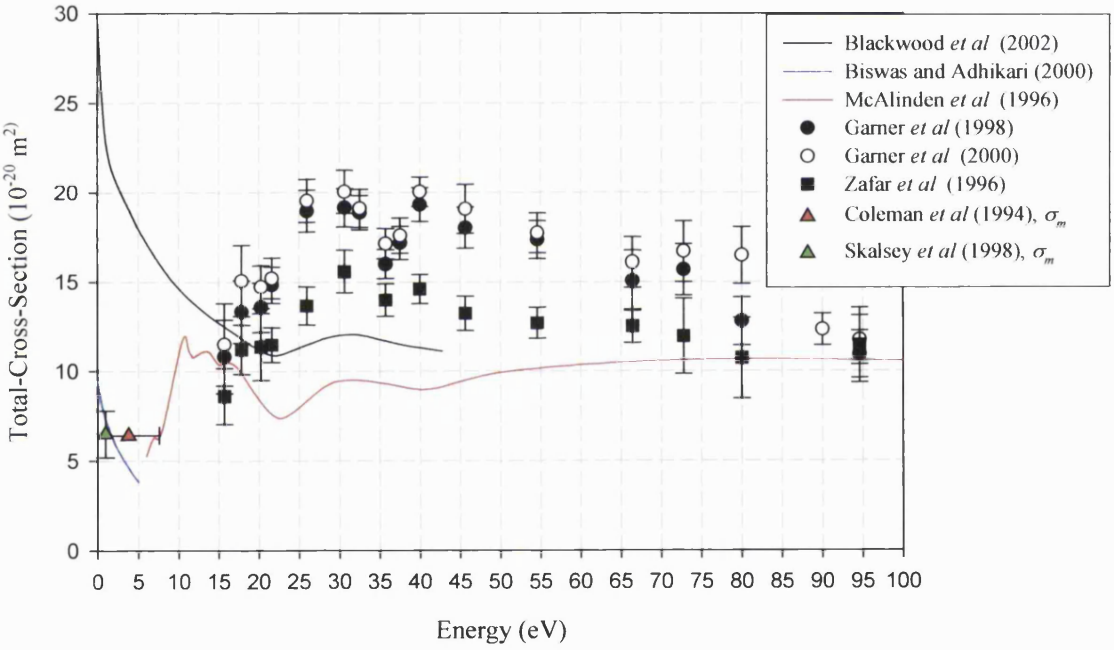

Figure 1.17 Ps-Ar total and momentum transfer cross-section comparison.

Figure 1.17 includes three sets of beam data. The beam measurements made by Zafar *et al* (1996) were taken with a $\pm 6^{\circ}$ detection angle as compared with Garner *et al* (1998) who used a $\pm 1.5^{\circ}$ detection angle. With the latter, a 30% increase in the total-cross-section was observed. The effect has been interpreted as arising from forward-angle scattering effects and has been evaluated in a study by Garner *et al* (2000) by varying the detection angle and interpolating the measured cross-section to zero-detection angle. It can be seen in figure 1.17 that the

extrapolated data broadly agree with the data of taken with a $\pm 1.5^{\circ}$ detection angle, suggesting that for Ar the effect of forward scattering at an acceptance angle of $\pm 1.5^{\circ}$ is almost negligible within experimental errors (Garner *et al*, 1998).

The Ps σ_T from H_2 is shown in figure 1.18. In Ps-H_2, the theory by Biswas and Adhikari (2001), using a three-Ps-state coupled-channel model and the Born approximation for target excitations and the excitation and ionisation of Ps, shows a similar energy trend to the beam data although the peak is shifted to lower energies by approximately 10eV. The theory is also seen to undercut experiment from 20eV onwards. The Doppler broadening measurement of Skalsey *et al* (1998) for σ_m is in excellent agreement with the theory of Biswas and Adhikari (2001), unlike the σ_m value determined by Nagashima *et al* (1995), which is higher by around a factor of 7. As in the case of Ar, the extrapolated σ_T for H_2 are in broad agreement with the values obtained by Garner *et al* (1998) at $\pm 1.5^{0}$.

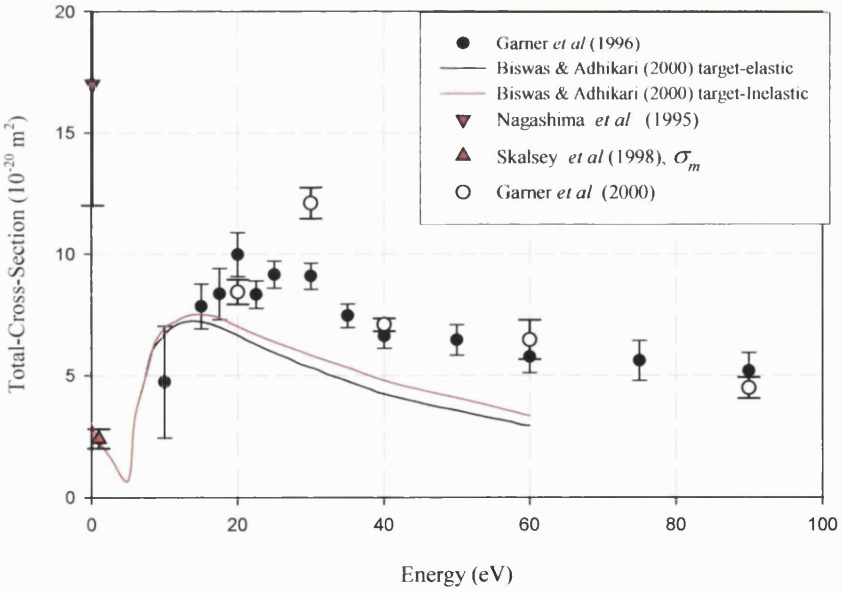

Figure 1.18 Ps-H_2 total and momentum transfer cross-section comparison.

Considerable discrepancies are present amongst both the theoretical and experimental results for the Ps-He total cross-section, shown in figure 1.19, the simplest system that has been addressed by both experiment and theory. The theory of Biswas and Adhikari (1999) is in very good agreement with the beam data, showing a down-turn in the cross-section for decreasing energy to join up with the Doppler

Broadening measurement for σ_m by Skalsey *et al* (1998) and the zero-energy σ_{el} of Adhikari (2001), calculated from the Ps-He scattering length. The close-coupled method employed by Basu *et al* (2001), using two basis sets, shows good agreement with the beam data in the energy range 20-30eV but shows no significant down-turn in the cross-section at lower energies. It also agrees with the estimate of σ_m obtained from the 2D- ACAR study of Coleman *et al* (1994). The theory of Sarkar *et al* (1997) overlaps the beam data in the energy range 20-30eV but is higher at lower energies where it joins up with σ_m of Nagashima *et al* (1998). The results of a 22-state close-coupling method employed by Blackwood *et al* (1999) are in excellent agreement with σ_m of Nagashima *et al* (1998) and Coleman *et al* (1994) but drop below the beam data in the energy range 20-40eV. Recently, using the schocastic variational method, Ivanov *et al* (2001) have calculated a value of $9.15\times10^{-20}m^2$ for the threshold cross-section.

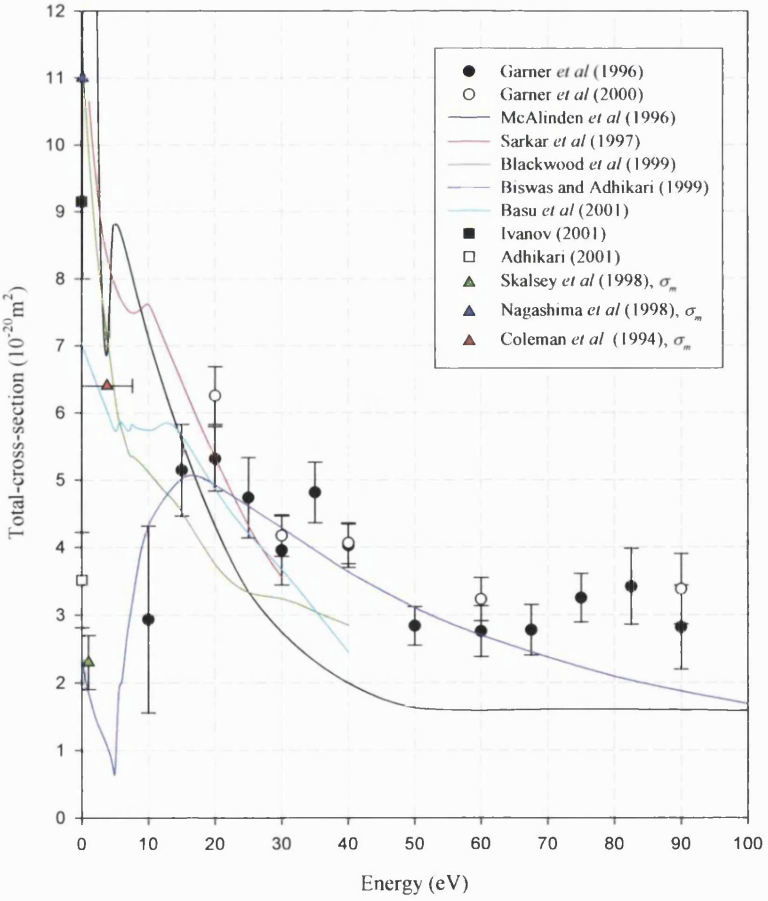

Figure 1.19 Comparison of theoretical and experimental determinations of the Ps-He total cross-sections.

1.6 Motivation for the Present Work

Up until now, Ps beam experiments have been restricted to total cross-section measurements from simple target atoms and molecules i.e. H_2, Ar and He. Theoretically Ps-atom scattering is a difficult problem to treat in atomic collision theory, due to the fact that both projectile and target are composite objects with internal structure. Theorists have hence addressed primarily simple target atoms and molecules and, in some cases, they have been able to extend their computations to a variety of partial cross-sections in advance of experimental determinations. In addition to their intrinsic interest, measurements of Ps-target partial cross sections are currently desirable as they might assist in resolving serious discrepancies among theories, theories and experiments, and among experiments, as discussed in section 1.5.3.

For these reasons, detailed measurements have been performed for Ps ionisation (break-up) in collision with He atoms. In order to ascertain the absolute magnitude of the Ps-He break-up cross-section, a determination of both the positron and Ps detection efficiencies also had to be performed. A study into the detection efficiency, for both projectiles, is described in chapter 4 and extended to determine absolute Ps-He break-up cross-sections in chapter 5.

Longitudinal energy spreads for the residual positrons from Ps break-up have also been obtained by using a time-of-flight detection system. The calibration technique employed to convert the time-of-flight to energy spectra is described in chapter 3. The technique has been used to determine the positron and Ps beam kinetic energy and extended in chapter 5 to determine the longitudinal energy spreads of the residual positrons.

Overall conclusions are drawn in chapter 6, which includes a discussion on the outlook in the field.

Chapter 2
Equipment and Detection Systems

2. 1 Overview

In this chapter, the experimental apparatus and detection techniques for both positrons and Ps are described. The apparatus, shown schematically in fig 2.1, was initially designed by Zafar *et al* (1992) and developed by Garner (1997) and Özen (2000) prior to the work described in this thesis.

The system can be divided into two distinct sections: the *source* side, which provides a beam of monoenergetic positrons and the *experimentation* side, which houses the detectors and interaction region.

The source side comprises a radioisotope of sodium (Na^{22}) as the source of fast β^+ particles. These are thermalised using an Ar gas solid moderator and accelerated to the required energy by providing a positive bias to the source with respect to the chamber ground. The positrons are radially confined by an axial magnetic field generated by eleven Helmholtz coils. A Wien filter and collimator are used to remove fast particles emanating from the source and to prevent a line of sight between the source and detectors. A pneumatic valve, situated after the Wien filter, is used to isolate the two halves of the system.

The experimentation side contains two gas cells. Ps is produced in the first ("production") cell via positron charge exchange in H_2, whilst the Ps beam is scattered from gaseous targets in the second (" scattering") cell. Situated between the two gas cells is a retarding arrangement, such that any residual positrons exiting the production cell are reflected away from the detectors and the scattering cell.

In this work, various detection systems have been utilised to investigate Ps scattering. Time-of-flight measurements were achieved via a Tagger (CEMA1), placed before the production cell and a second detector (CEMA2), situated at the end of the Ps flight path. Coincidences between the two detectors yielded an improved signal-to-background rate, as well as enabling an analysis of the energy spreads of both the positron and Ps beams.

An alternative coincidence detection system, incorporating a CsI

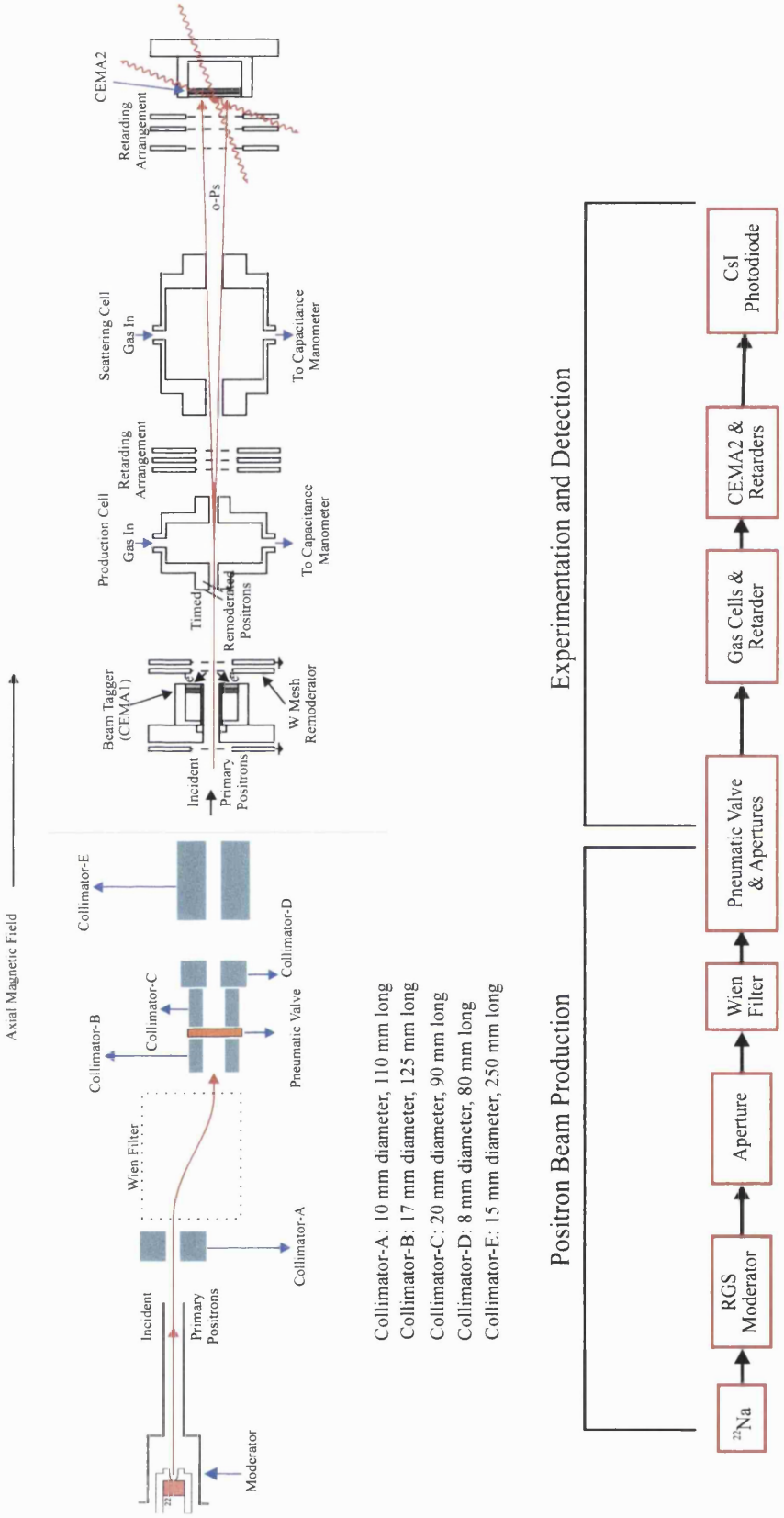

Figure 2.1 Schematic of the Ps beam.

photodiode γ-ray detector in coincidence with CEMA2, has also been used in this work. The advantage of this latter arrangement being that no remoderation of the positron beam is required, hence enabling the use of the full intensity primary positron beam.

Every component of the experimental apparatus and each detection system are described in detail in the following sections.

2.2 Positron Beam Production

2.2.1 β^+ Source

The radioisotope used as the source of β^+ particles for this study was ^{22}Na, with a half-life of 2.6 years, supplied by Du Pont plc. The source had an initial activity of 137.4mCi, when installed, decaying to 77.6mCi by the end of this study. A manipulator was designed for the installation of this new source, such that installation could be carried out safely with minimum exposure (for the protocol on the source installation see appendix A). An extra 15mm of Pb were placed around the source chamber for radiation protection before this new source was installed.

2.2.2 Rare Gas Solid Moderator

As shown in figure 2.2, the ^{22}Na source is mounted on the cold-finger attached to the cold-head of a two-stage closed-cycle refrigerator (APD model DE-204SLB). The temperature is monitored with a Cr-AuFe 0.07% type thermocouple, attached to the end of the cold-head, registering an ultimate temperature of ~7K. The cold-head temperature may be increased by means of two heater coils (running a current of 0-1A) wrapped around the cold-head. Between the cold head and the cold finger a sapphire disc (0.5mm diameter) (Al_2O_3, 99.9% pure) is placed to achieve electrical isolation (such that the cold finger, and hence source, may be biased) whilst maintaining good thermal conductivity at low temperatures. The cold-finger is made from an alloy (70% W + 30% Cu) and connected to the cold-head via a machinable glass-ceramic M6 screw.

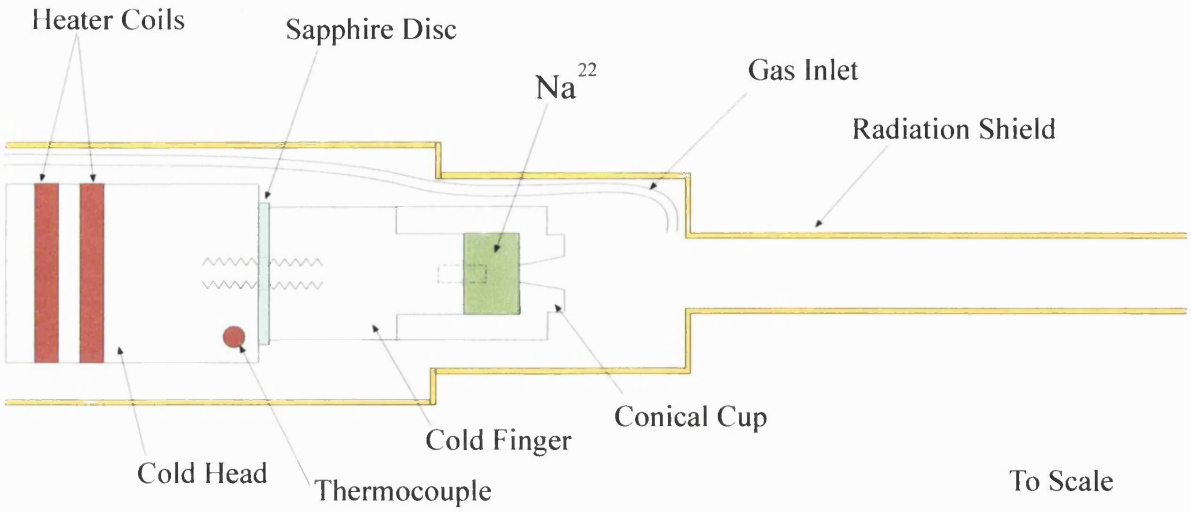

Figure 2.2 Schematic of the cryostat cold head and cold finger.

The cup (70% W + 30% Cu) on which the moderator is grown has a conical exit aperture. No difference in performance has been observed between the conical cup used in this work and the parabolic cup used by Özen *et al* (2000), for similar growing conditions. Previous works on cup geometries have shown that conical and parabolic cups give the highest comparable yields (Khatri *et* al, 1990 and Greaves and Surko, 1996 respectively) by providing a large surface area, whilst allowing good penetration of the electric field for slow positron extraction. Electrical contact with the moderator cup is achieved via a tungsten wire (0.075mm diameter, 99.9% pure) connected to the cold finger with an OFHC copper screw from a feed-through on the cryostat miniflange. The wire is insulated with fibreglass and wrapped around the cold head several times. A 1mm thick infrared radiation shield (OFHC copper) extends 90mm beyond the source, surrounding the whole moderator assembly. The radiation shield is grounded via the cryostat to extract positrons from the positively biased moderator. Ar gas is admitted inside the radiation shield through a stainless steel pipe (1.75mm inside diameter and an OFHC copper pipe (1.3 mm inside diameter), separated by a PTFE connector. The temperature of the cold head is monitored by a Lakeshore temperature controller, allowing the temperature to be varied from 7K-320K by providing the current to the heater coils.

2.3 Positron Beam Transport

2.3.1 Magnetic Guidance

The positron beam is magnetically confined to the beam axis by eleven Helmholtz coils. These have an outer diameter of 700mm and are water cooled to avoid over heating. In order to maximise the transport efficiency of the beam, the coils can be rotated about both the y- and z-axes and moved along the x-axis. The magnetic field strength varies along the beam axis (25 - 120 Gauss) in order to squeeze the beam through apertures and the tagger, whilst reducing spiralling of the positron beam in the scattering region. When the time-of-flight detection system is employed, the highest **B**-field is situated around the tagger. This serves to focus the primary positron beam through the tagger aperture and to achieve a degree of parallelisation of the remoderated beam in the interaction region via the drop in the **B**-field strength after the tagger (Kruit and Read, 1983) by reducing the positron pitch angle. The pitch angle, α, is defined as the angle between the longitudinal direction and the emission vector. As the positrons move from one field region to another the pitch angle changes according to:

$$\frac{B_1}{B_2} = \frac{\sin^2 \alpha_1}{\sin^2 \alpha_2}. \qquad (2.1)$$

2.3.2 Wien Filter

The moderated positron beam is separated from the flux of fast particles and γ-rays emanating from the source by deflection through a Wien filter, see figure 2.3.

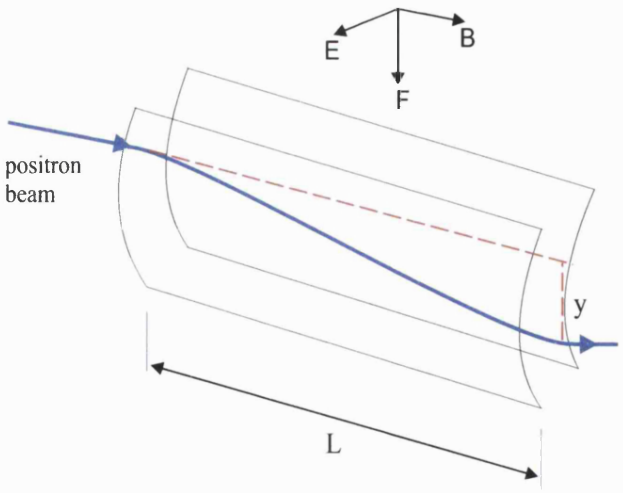

Figure 2.3 Schematic of the Wien filter.

The Wien filter consists of a pair of plates (curved following the design of Hutchins *et al*, 1986), across which an electrostatic field **E** is applied perpendicular to the axial magnetic field **B**, generated by the Helmholtz coils. This causes charged particles with a velocity, υ, to drift by a distance y where

$$y = \frac{\mathbf{E} \times \mathbf{B}}{\mathbf{B}^2}\left(\frac{L}{\upsilon_Z}\right). \tag{2.2}$$

Here L is the length of the plates and υ_z is the particle velocity parallel to **B**. In this way, the axis of the positron beam is lowered by approximately 3.5cm, whilst the fast particles and γ-rays are dumped into a Pb block.

2.4 Vacuum System

Figure 2.4 shows a schematic diagram of the vacuum system. The two halves of the apparatus are pumped differently and will be described separately.

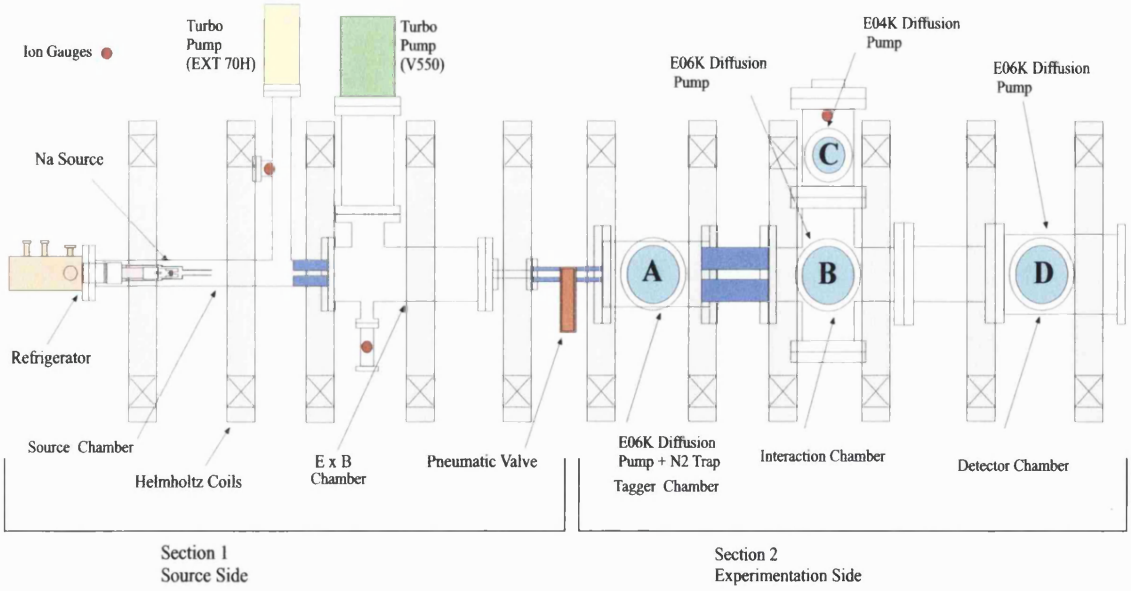

Figure 2.4 Schematic of the Ps beam vacuum system.

2.4.1 Source Side

The source chamber is evacuated by an Edwards turbo drag pump (EXT 70H), aided by a Varian turbo pump (V550) connected to the E×B chamber. Both turbo pumps are water-cooled and backed by one Edwards two-stage rotary-pump (E2M28). Between the backing and turbo pumps, the backing pressure is monitored with a Pirani gauge. The backing pump can be isolated using either a magnetic or manual valve. Two ion gauges, one in each chamber, are used to monitor the system pressure. Whilst growing RGS moderators, the ion gauge in the source chamber is switched off due to the high pressures at which they are grown (greater than 10^{-5} Torr in source chamber). The growing pressure is hence monitored with the ion gauge in the E×B chamber.

2.4.2 Experimental Side

On the experimentation side of the system, four oil-based diffusion pumps (One Edwards E04K and three E06K) are used to provide high-vacuum. The diffusion pumps are water-cooled to avoid overheating. Two of them (pumps A and D, see figure (2.4)) are backed by Varian SD-300 rotary pumps, whilst the remaining E06K

(pump B) and the E04K (pump Ç) are both backed by an Edwards ED-660 rotary pump. Pirani gauges, magnetic valves and isolation taps are placed between each diffusion pump and corresponding backing pump. A LN_2 trap is situated above diffusion pump A to reduce diffusion of oil and water vapours into the source side. However, no difference in moderator efficiency has been observed without LN_2 in the trap. Instead, a slight depreciation of positron yield with time is noticed after opening/closing the pneumatic valve, due to a small leak through the valve bellows. We were unable to repair the pneumatic valve during the course of this study, therefore, unless absolutely necessary, the pneumatic valve was left open. An ion gauge is situated in the cell chamber in order to check the system base pressure (approximately 10^{-7} Torr).

2.5 System Protection Devices

A number of safety devices are incorporated in the system in order to prevent damage due to water or electrical failure. The water-cooled diffusion pumps, turbo pumps, cryostat and Helmholtz coils are protected by a series of six water-circuits, each comprising a flowtron, a switch which relies on the water pressure to maintain a closed circuit. If this connection is broken, due to a reduction of water pressure, leakages or blockages, the trips are activated. Once activated, the two sides of the system are isolated via closure of the pneumatic valve and the power to the coil supplies, diffusion and turbo pumps as well as the high-voltages are switched off. The magnetic valves, situated between each respective pump and its backing pump, are also closed to stop backstreaming into the system through the backing line.

Protection circuits based upon the pressure in the backing lines are also present in case of pump failure, leaks in the vacuum chamber or an uncontrolled influx of gas. The safety level on the backing pressure gauge controller is set to 6×10^{-2} Torr, at which point the protection devices would be activated, shutting down the system as described above.

2.6 Experimental Region

2.6.1 Beam Tagger (CEMA1)

In order to achieve time-of flight measurements, a 'tagger', from which a 'start' pulse could be obtained, is lowered into the positron beam before the gas cells. The tagger incorporates a remoderation technique (Laricchia *et al*, 1988). A schematic of the present arrangement is shown in figure 2.5.

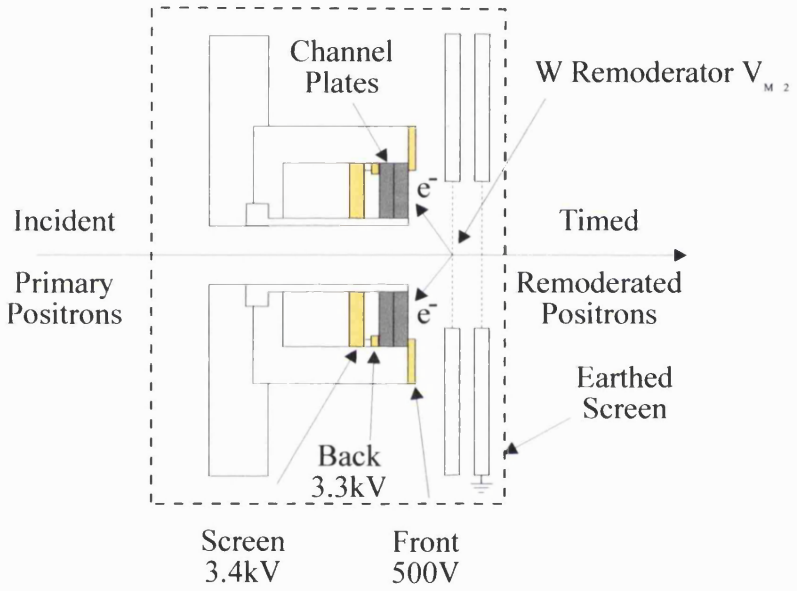

Figure 2.5 Schematic of the positron beam tagger.

Secondary electrons released from the W mesh remoderator, by positron impact, are extracted electrostatically to a Channel-Electron-Multiplier-Array (CEMA1). The detector array consists of two 'channel-plates', discs of tightly packed glass tubes of internal diameter 25μm. The channel-plates have a central hole through which the positron beam passes to reach the remoderator. Particles incident upon the front of the channel-plates can cause the release of secondary electrons that are accelerated through the channel-plates by the potential difference (~3kv) placed across them. Within the plates, the micro-channels are set at an angle of 51°, such that the secondary electrons collide with the walls creating more secondary electrons, resulting in an avalanche effect. The two channel-plates are aligned such that the channels form a chevron arrangement. This arrangement prevents secondary electrons

from traversing the plates without hitting the walls and serves to reduce ionic feedback, whereby residual gas at the output of the plates can be ionised by the electron avalanche. The resulting ion may be accelerated back through the plates, causing the release of secondary electrons, giving rise to spurious signals. At the output of the channel plates, the charge created by the electron avalanche is drawn by a small potential difference to a collector ('screen'), consisting of a brass disc. The pulses obtained from the screen are fed into the external electronics, described later. The tagger is situated at the end of a manipulator, allowing linear and rotary motions. The manipulator allows the tagger to be positioned for maximum count rate and also to be moved out of the beam when other detection techniques are in use. The remoderator consists of four annealed W meshes, positively biased with respect to the earth grid in order to set the positron beam energy. The whole tagger assembly is encased in a grounded wire mesh in order to minimise stray electric fields.

When using the tagger, the initial positron beam-energy is set to 300eV at the RGS moderator. At this energy, epithermal emission from the remoderator contributes around 15% to the beam composition. Additionally, possible contributions from Ps formed by the primary beam in the production cell will be small since the Ps formation cross-section at this energy is negligible. This is confirmed by the absence of a corresponding peak in the time-of-flight spectrum.

2.6.2 Gas Cells

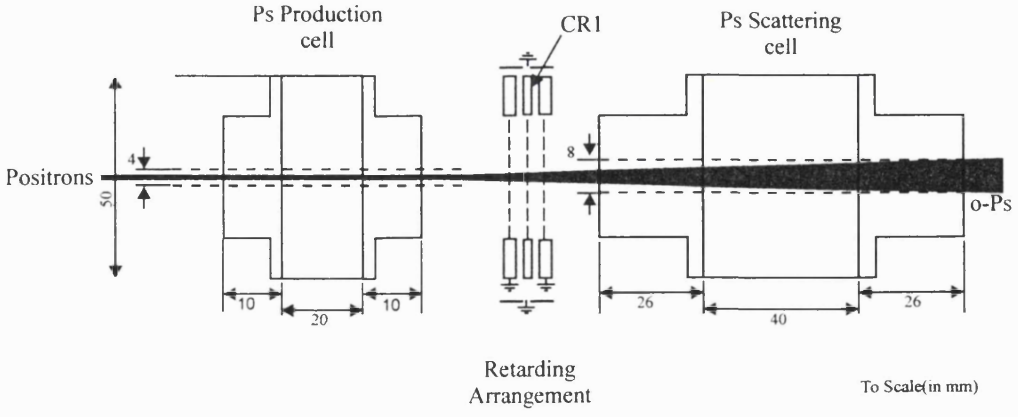

Figure 2.6 Schematic diagram of the gas cells used in this study.

Two differentially pumped gas-cells have been used in this study. The production cell is employed to create Ps via charge exchange of positrons in H_2

(typical pressure = 10μmHg, Garner *et al*, 1996), whilst in the second cell Ps scattering occurs. The gas cells, shown schematically in figure 2.6, are both made from aluminium cylinders with brass apertures and the gas cell pressure is monitored by an external capacitance manometer (Chell MK 7893, with a range of up to 1 Torr). A retarding arrangement is placed between the two cells in order to stop residual positrons exiting the Ps production cell from entering the scattering cell. The retarding arrangement consists of 3 grids (90% transmission), the middle grid being positively biased to 500V (when working with Ps), whilst the outer two grids are grounded, shielding the interacting region from stray electric fields.

2.6.3 End-of-flight Detector (CEMA2)

A second channel-electron-multiplier-array (CEMA2), shown in figure 2.7, is placed at the end of the flight path to detect e^+/Ps. The channel-plates at CEMA2 are exactly the same as for the tagger, but without the central hole.

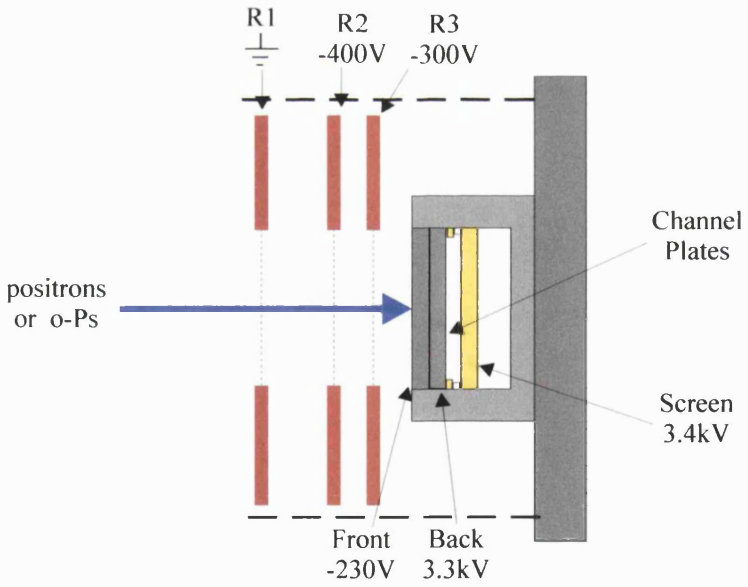

Figure 2.7 Schematic diagram of the end-of-flight detector CEMA2.

A retarding assembly consisting of three grids (90% transmission) is situated in front of CEMA2. The first grid, R1, is grounded when detecting positrons and positively biased when detecting Ps to prevent any residual positrons emanating from the

scattering cell to be detected at CEMA2. The grids R2 and R3 are used to increase the detection efficiency of CEMA2 by returning any secondary electrons emitted away from the surface of CEMA2. The grid potentials are shown in figure 2.7. The whole array is surrounded by an earthed wire mesh to reduce stray electric fields and mounted on a linear manipulator such that the flight-length may be varied.

2.6.4 CsI γ - ray Detector

In this study, an alternative coincidence circuit to the time-of-flight system was made by utilising the annihilation γ-ray of either a positron or Ps. The required coincidence being between CEMA2 and a γ-ray detector situated outside the vacuum chamber, see figure 2.8. This system had the advantage of utilising the entire initial positron beam, as no remoderation was required.

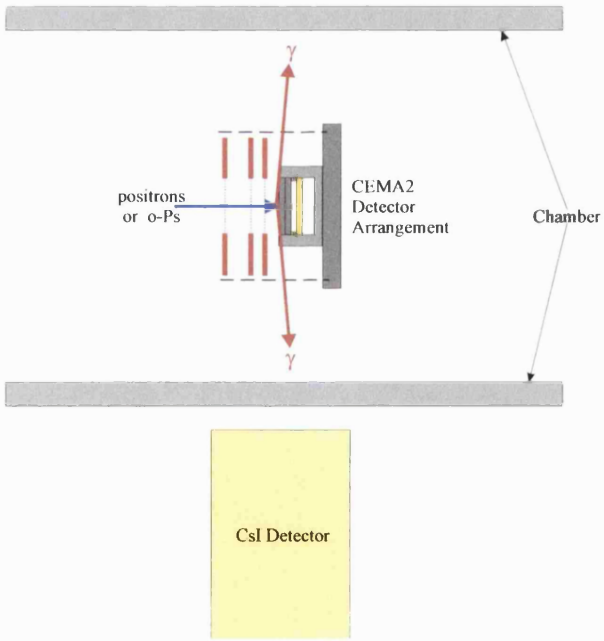

Figure 2.8 Schematic diagram of the position of the CsI detector with respect to CEMA2.

The γ-ray detector used was a CsI crystal scintillator (eV products, Model No. eV-251-03), 40mm thick with a diameter of 40mm, coupled to a photodiode.

2.7 Detection Systems

2.7.1 Time-of-Flight Detection System

The time-of-flight detection system employed both the tagger (as described in section 2.6.1) and CEMA2 (described in section 2.6.3). These two detectors provided stop and start signals respectively for an inverted timing sequence. This was done as the number of pulses from the tagger was approximately 8 times that of CEMA2 when detecting positrons, hence a reduction in the dead time was achieved (Davis, 1987). The pulses, typically 9mV, from each detector were obtained from the screen via a capacitor, terminated by a 3.5kΩ resistor. The pulses were then fed to fast (x10) pre-amplifiers. After the pre-amplifiers, the pulses were passed through a constant fraction discriminator (CFD). The signal from the tagger CFD was delayed by 754ns and then inputted, together with signals from CEMA2, into a time-to-amplitude converter (TAC). The TAC output was fed directly into a PC-based Ortec multichannel analyser (MCA). A block diagram of the time-of-flight electronics is shown in figure 2.9.

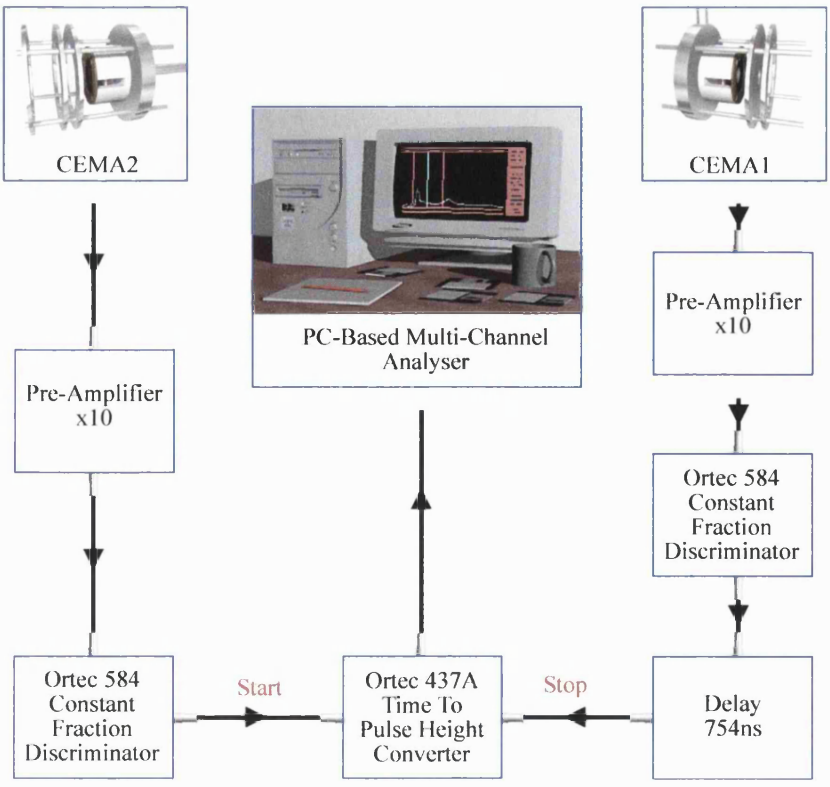

Figure 2.9 Block diagram for the time-of-flight electronics.

Examples of time-of-flight spectra for the incident positron beam, incident Ps beam and background (obtained with vacuum in both gas cells) are shown in figure 2.10. Spectrum a) was taken using a 44eV positron beam. Spectrum b) was obtained by neutralising the positron beam in the production cell via H_2 to form Ps. Spectrum c) was taken with vacuum in both gas cells. In spectrum a) two peaks are seen, the positron peak corresponds to remoderated positrons detected at CEMA2. Peak (A) corresponds to electrons, which have been released through positron impact at CEMA2, that travel back down the beam line to be detected at the tagger. In spectrum b) various peaks are seen: the peak corresponding to Ps is observed around channel 540 and a *t=0* peak, corresponding to positrons annihilating at the remoderator, is found at channel 840. The *t=0* peak relies on either the back-to-back photons from positron annihilation being detected at the Tagger and CEMA2, or an electron liberated at the remoderator being detected at the Tagger, and one of the annihilation photons detected at CEMA2. The peaks marked (B) correspond to positrons and Ps annihilating at the cells and CR1. In spectrum c) similar structure to that in the Ps spectrum is visible, with the notable exception of the Ps peak itself.

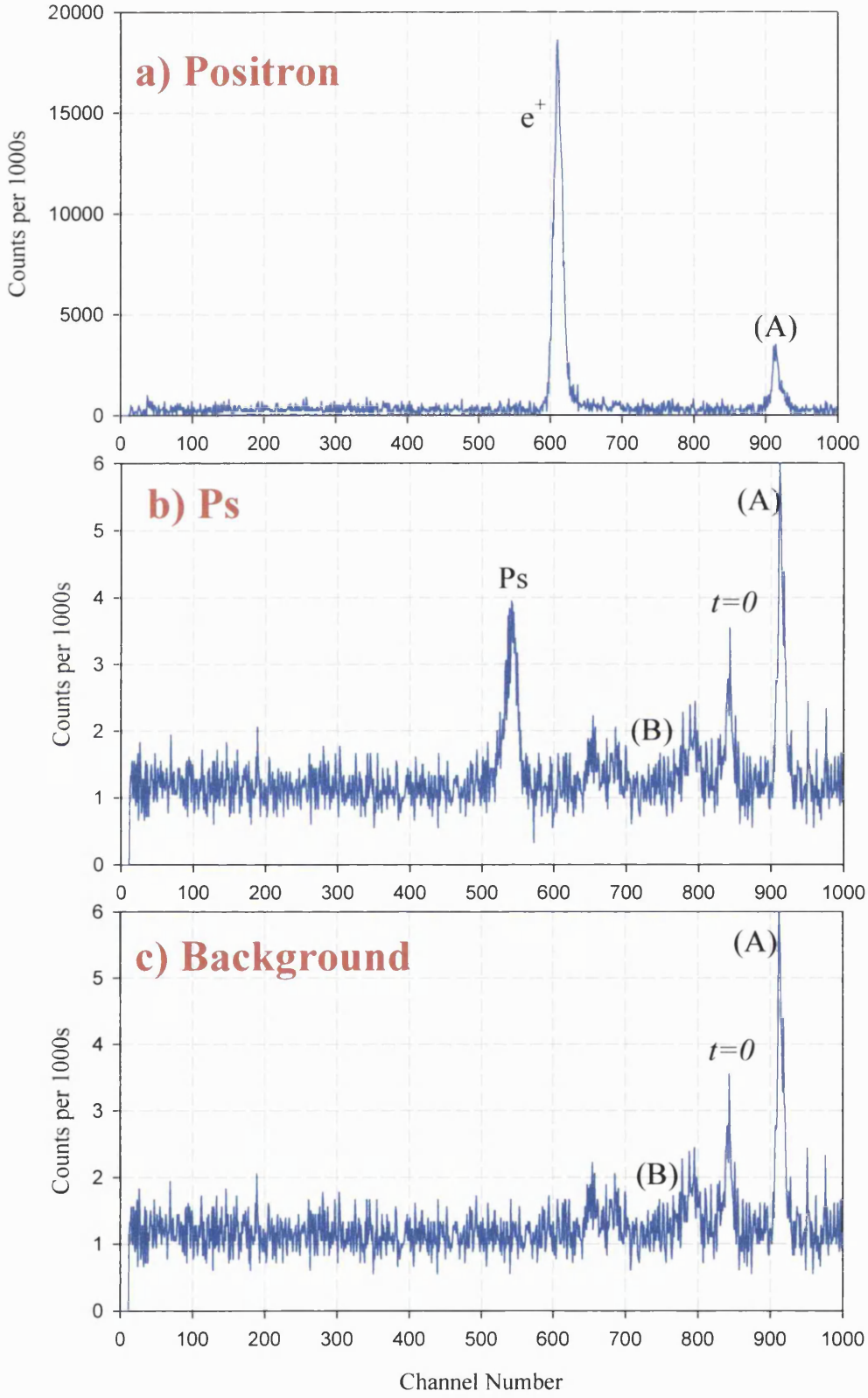

Figure 2.10 Typical time-of-flight spectra for a) incident positron beam, b) incident Ps beam and c) background.

2.7.2 CEMA2/CsI Coincidence System

The experimental set up for the CEMA2/CsI coincidence system is similar to that of the time-of-flight detection system, with the CsI detector replacing the Tagger, see figure 2.11. The CsI pulses were internally amplified before being fed into an Ortec 570 amplifier. These modified pulses were then inverted in an Ortec 474 Timing Filter Amplifier (TFA), such that they could be fed into a CFD. Finally, this signal was used as the stop pulse for the TAC, where the output was fed directly to a PC-based MCA.

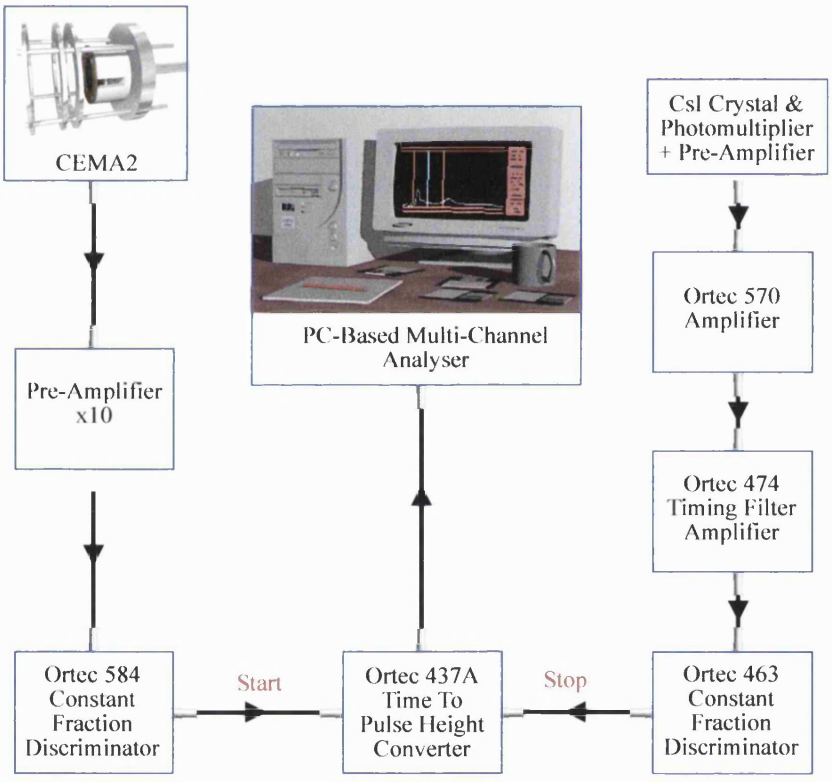

Figure 2.11 Block diagram for the CEMA2-CsI coincidence electronics.

The resulting spectra, for the incident positron beam, incident Ps beam and background are shown in figure 2.12. Spectrum a) was taken with a 44eV energy positron beam. This was neutralized in the production cell, to produce a 35eV Ps beam (spectrum b)). Once again the background spectrum c) was taken with vacuum in both gas cells. The intrinsic width of the coincidence peaks are a function of the time taken for the secondary electrons to traverse the channel plates, the intrinsic

timing resolution of the CsI detector and the time delays introduced within the electronics.

Since, using this method, it is not possible to distinguish between different states of Ps atoms (as opposed to the time-of-flight detection system) this CEMA2/CsI detection system was put into practice only after characterisation of the Ps beam had taken place using the time-of-flight system. Further discussion on the characterisation of the Ps beam can be found in section 3.2.4.

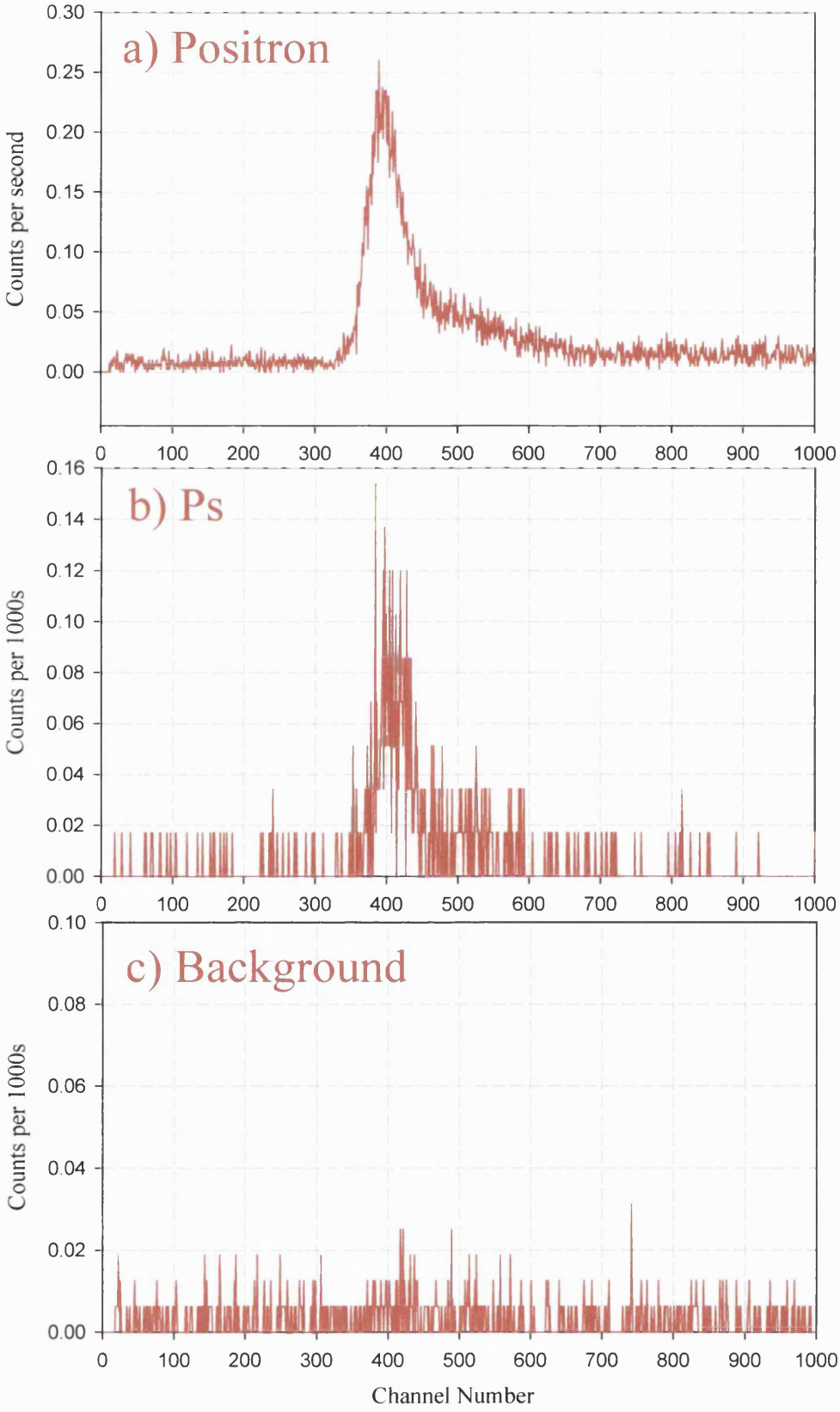

Figure 2.12 Typical CEMA2/CsI coincidence spectra for a) incident positron beam, b) incident Ps beam and c) background.

Chapter 3
Positronium Beam Techniques

In this chapter, the techniques used to produce a beam of monoenergetic Ps atoms and its application to total-cross-section measurements are described. The methods for preparing, growing and annealing a rare gas solid moderator (Gullikson and Mills, 1986) are outlined. The positron moderation efficiencies obtained in this work are compared with previous values, obtained both with the same apparatus (Özen *et al*, 1999) and with alternative experimental set-ups. The energy spread of the positrons emitted from the rare gas solid moderator has been found to be sensitive to the moderator thickness, even after the efficiency has saturated. The energy distribution is compared with previous measurements, whereby the epi-thermal contribution to the energy spreads are found to be large in comparison with this study.

With suitable calibration, the time-of-flight time spectra may be converted into energy distributions. The calibration technique is described here and applied to determine the Ps energies employed in this study.

3.1 Slow Positron Beam Production

3.1.1 Experimental Procedure for Growing Rare Gas Solid Moderators

As described in section 1.4.2, rare gas solid moderators have been found to be the most efficient positron moderators and have thus become widely used by research groups around the world. Among the rare gas solids, Ne has been found to be the most efficient moderator by approximately a factor of 5 (Mills and Gullikson, 1986). Previous work by Özen *et al* (thesis, 1999) found that sufficiently low temperatures of the cold-head could not be achieved with the present cryostat. These are required to produce Ne moderators with reliably stable high efficiencies. Therefore in the present work, we have restricted ourselves to using a solid Ar moderator.

Ultra-high-vacuum conditions are required for moderator stability (Petkov *et al*, 1997). To achieve this, before growing each moderator, the system was baked until base pressures of ~1×10^{-10} torr and ~1×10^{-9} torr were achieved in the E×B chamber and source chamber respectively. After baking and before switching on the cryostat, the gas line and system were flushed to reduce impurity concentrations.

Once the cryostat had reached its ultimate temperature (7K), Ar gas was admitted through the gas line, such that a pressure of 1×10^{-8} torr was achieved in the E×B chamber. Whilst growing the moderators, the positron beam intensity was monitored using CEMA2. The pressure (P_m), measured with the ion gauge in the E×B chamber, was corrected for the gas under study according to:

$$P_T(true) = P_m(measured)/K, \tag{3.1}$$

where K is the normalisation constant for the gas (equal to 1.4 for Ar). From this pressure, P_T, an estimate of the pressure inside the heat shield was calculated via the equation:

$$P_I = P_T\left(\frac{S_2}{C}+1\right), \tag{3.2}$$

where S_2 is the pumping speed for the system and C is its conductance. From the calculations, the ratio between the two pressures (P_T/P_I) was found to be 1.0×10^{-3}. Figure 3.1 shows a typical plot for moderator growth.

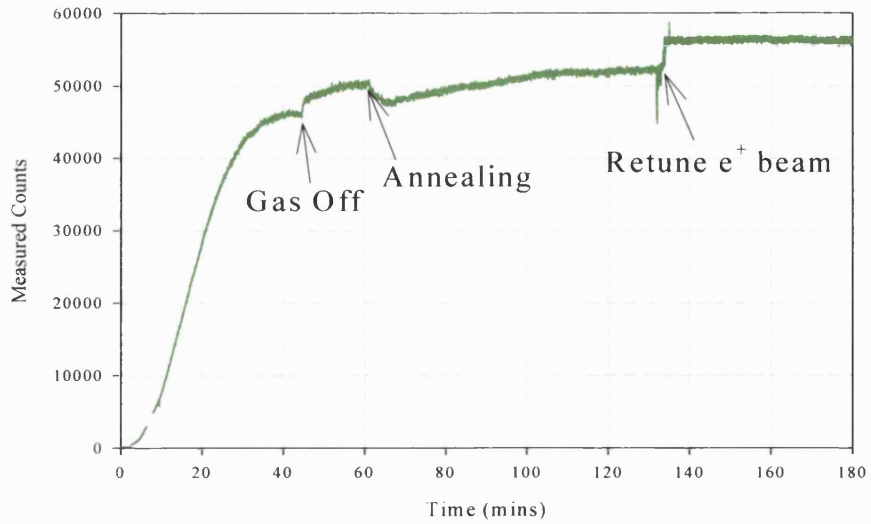

Figure 3.1 Typical Ar moderator growth at a temperature of 7K and pressure of 1.5×10^{-5} Torr.

As shown in figure 3.1, the number of slow positrons increases with increasing thickness of moderator, until saturation, at which point the gas is shut off. After the gas valve is closed, a marked increase in positron beam intensity is observed, as fewer positrons are attenuated by the residual gas. After shutting the gas off, the moderator is annealed at 35K for 3 minutes. Annealing the moderator has the effect of realigning the lattice, as crystals grown at low temperatures and high pressures may be highly defective (Klein and Venables, 1977). No sharp increase in slow positron yield is observed in figure 3.1, suggesting a low defect concentration from a moderator grown at this pressure (1.5×10^{-5} Torr). It should be noted however, that Ar moderators grown at higher pressures have resulted in a rapid increase in positron yield directly after annealing. These effects are, at comparable growing pressures, the same as those seen by Özen *et al* (2000). A secondary effect of annealing the moderator is to remove residual Ar frozen onto the cold head, resulting in a lower base pressure and hence a more stable moderator efficiency.

3.1.2 Comparison with Other Work

The moderation efficiency is defined here as the ratio of low-energy positrons emitted from the moderator to the total number of positrons produced by the radio-nuclide. For this reason, the number of detected positrons must be corrected for the efficiency of the detector (see section 4.4) and, where possible, the transport efficiency. Within the work of Özen *et al* (1999), the positron beam intensity was measured with and without the various collimators and gas cells along the beam line, in order to determine the transport efficiency of the system. Without the collimators and cells, the beam intensity was higher by a factor of four. This same number has been used in this study to correct the moderator yields for the transport efficiency. No corrections have been applied for the attenuation caused by the source window (estimated to be <10%).

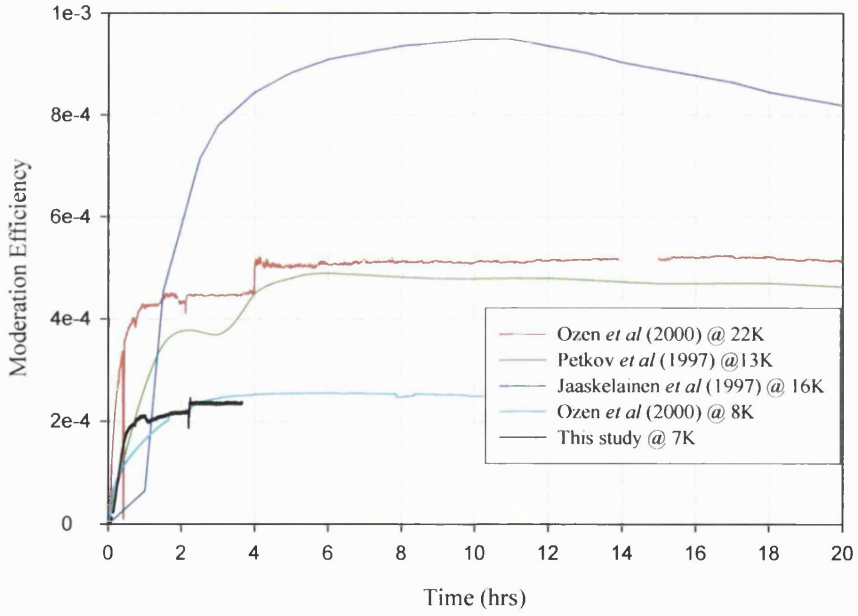

Figure 3.2 Comparison of Ar moderators.

As can be seen in figure 3.2, there is a reasonable agreement between the moderator efficiencies obtained in this study and those of Özen *et al* (2000) grown at 8K. Any discrepancy between the efficiencies determined by Özen *et al* may be down to the different beam tuning and hence different transport efficiency. Although Özen *et al* found the moderator efficiency to double for moderators grown at 22K, within this

study we had to limit our growing temperature to the base temperature of the cryostat, i.e. 7K, due to constraints on the cryostat heaters. An unambiguous comparison with Petkov *et al* (1997) and Jääskelainen *et al* (1997) is not possible due to their unknown detection, source and transport efficiencies.

3.1.3 Energy Spread of the Positron Beam obtained from an Ar Moderator

The energy spread, ΔE, of the positron beam from the Ar moderator was measured, once the efficiency had saturated, by applying a retarding potential to R2 (see section 2.6.3) in front of CEMA2. ΔE was found to be ~5eV, larger than that of ~2eV reported by Mills and Gullikson (1986) and Petkov *et al* (1997). To try and reduce ΔE, extra Ar was deposited at the same temperature and pressure, and energy spreads were measured after every few hours. Figure 3.3 shows the variation of the energy distributions full-width-half-maximum (FWHM) thus measured.

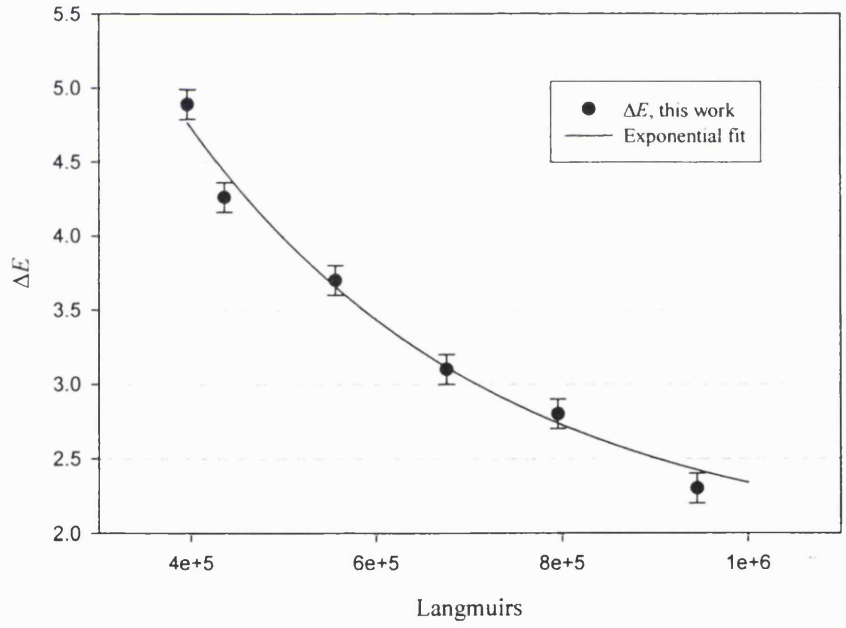

Figure 3.3 Ar moderator energy distribution FWHM.

Gullikson and Mills (1986) explained the relatively wide energy spreads obtained from RGS moderators in terms of epithermal positron emission. In a RGS, as stated in section 1.4.2, when the positron kinetic energy falls below the threshold for Ps

formation, energy loss is dominated by phonon emission. Therefore, the energy of the emitted positron may be between the threshold for Ps formation and zero, depending on the implantation depth and phonon emission rate. As the moderator thickness increases, a decrease in the epithermal positron contribution to the moderator energy spread would be expected, due to the effective increase in the implantation depth. Gullikson and Mills (1986) have reported a value of 9.95±0.05 eV for the Ps formation threshold, E_{th}, within solid Ar. Figure 3.4 shows a typical retarding spectrum for an Ar moderator. As can be seen from the figure, E_{th} is in agreement with the value quoted above. Gullikson and Mills investigation of RGS as remoderators found that, at higher implantation energies, the emitted positrons had narrower energy spreads, suggesting that as positrons penetrate deeper into the solid the epi-thermal contribution to the energy spread is reduced.

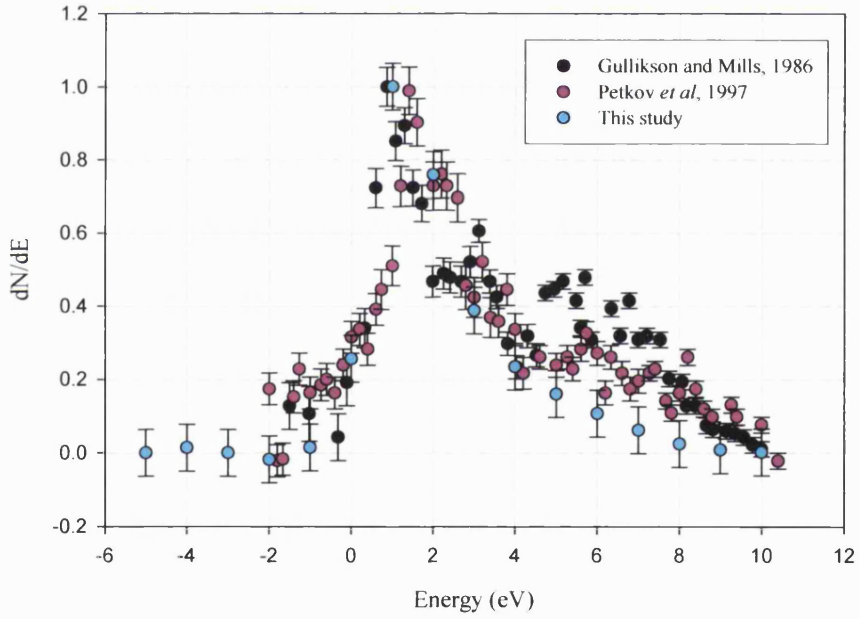

Figure 3.4 Comparison of the slow positron energy distributions obtained in this work, compared to those obtained by Gullikson and Mills (1986) and Petkov et al (1997).

Mills and Gullikson (1986) and Petkov *et al* (1986) have quoted values for the FWHM for the energy distribution of an Ar moderator as 1.7±0.2eV and 2.0 eV respectively, but both have large epithermal contributions, as shown in figure 3.4, and in the case of Petkov *et al*, only 50% percent of the moderated positrons are found to

be within the FWHM of the energy distribution. In figure 3.4, the slow positron energy distribution, obtained in this work, has been shifted by –1.5eV for comparison due to unknown contact potentials both in this and the work of Gullikson and Mills and Petkov *et al.*

By plotting a simple exponential decay curve through the measurements, we found that the ultimate Ar ΔE to be 1.9±0.4eV, which is comparable with those quoted in previous works but with a lower high-energy tail (Mills and Gullikson, 1986, Petkov *et al*, 1997 and Özen *et* al, 1999).

3.2 Energy Spread of the Ps Beam

3.2.1 Introduction

A measure of the Ps beam energy distribution may be ascertained by converting the time-of-flight spectrum from the MCA (see section 2.7.1). In order to calibrate the MCA, the time-per-channel, t_{ch}, is measured as described below. From this and measurements of the positron time-of-flight peak channel versus positron energy, the sum of the magnitude of the workfunction and contact potential of the remoderator, $|W| + C$, may be ascertained.

3.2.2 Time-per-channel, t_{ch}

To determine the time-per-channel for the MCA spectra, known time delays are inserted into the time-of-flight electronics between the CEMA1 CFD and the stop on the TAC (see section 2.7.1). For each time delay the channel number at which the positron peak occurs is recorded. A linear plot of the time delay versus channel number may then be made, from which the time per channel, t_{ch}, is calculated from the gradient. Figure 3.5 shows the time-per-channel measurements made for two remoderator potentials, V_m. The greater uncertainty inherent with the V_m=10V measurements is due to the larger time spread associated with lower beam energies on a time-of-flight spectrum.

V_m (V)	t_{ch} (ns)
10	0.959±0.002
100	0.962±0.001

Table 3.1 Time per channel values obtained at two values of the remoderator potential.

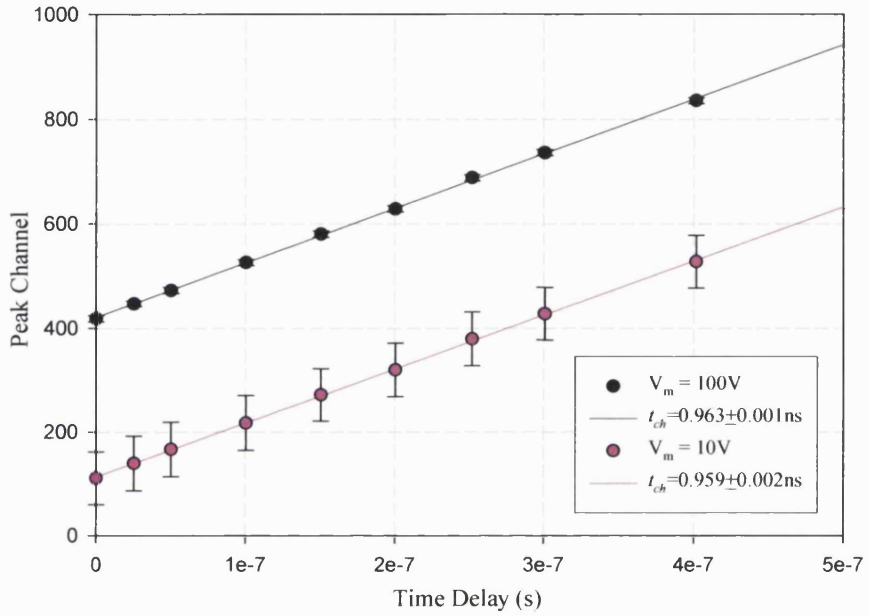

Figure 3.5 Time per channel calibration plot.

Table 3.1 shows the t_{ch} values obtained in this study. As can be seen from table 3.1, there is an excellent agreement between the t_{ch} values determined for the two moderator potentials.

3.2.3 Determination of the Absolute Positron Energy

In order to determine the absolute energy of the positron and Ps beams, the sum of the magnitude of the remoderator workfunction and contact potential, $|W| + C$, are required. The expected position of the positron peak, P_+, on the time-of-flight spectrum, is given by

$$P_+ = t0 - \frac{t_+}{t_{ch}}, \tag{3.3}$$

where $t0$ is the $t=0$ peak channel number (see section 2.7.1), t_+ is the time between the tagger and CEMA2 pulses respectively and can be written as

$$t_+ = t_{const} - t_{e^-} + t_{e^+} + t_{rets}, \tag{3.4}$$

where with reference to figure 3.6, t_{e^-} and t_{e^+} are respectively the acceleration times for secondary electrons and remoderated positrons at the tagger, t_{rets} is the time taken for acceleration through the grids in front of CEMA2 and t_{const} corresponds to the time for a positron of constant velocity ($v_+ = \sqrt{2E_+/m}$) to traverse the distance between the tagger earth grid and R1.

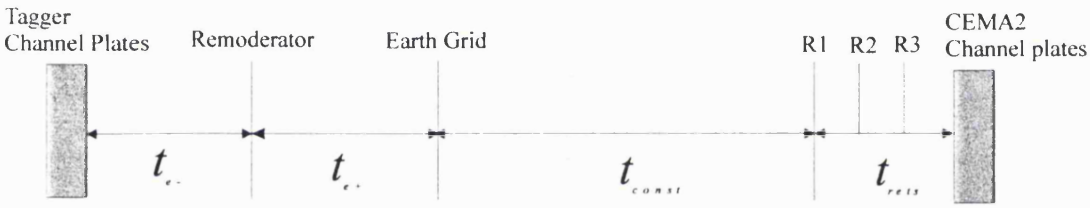

Figure 3.6 Schematic definition of the times relevant to the determination of $|W|+C$.

The positron kinetic energy, E_+, is determined by the remoderator potential, V_m, and the remoderator workfunction and contact potential, $|W|+C$, i.e.

$$E_+ = eV_m + |W| + C. \tag{3.5}$$

Therefore, a value for $|W|+C$ may be determined by comparing the calculated P_+ values with corresponding measurements for differing V_m and iterating over $|W|+C$ to fit to the measured data. The full fitting equation is given in Appendix B. Figure 3.7 shows the comparison of the measured peak positions to the calculated values, from which a value for $|W|+C$ of 1.0 ± 0.1eV has been determined.

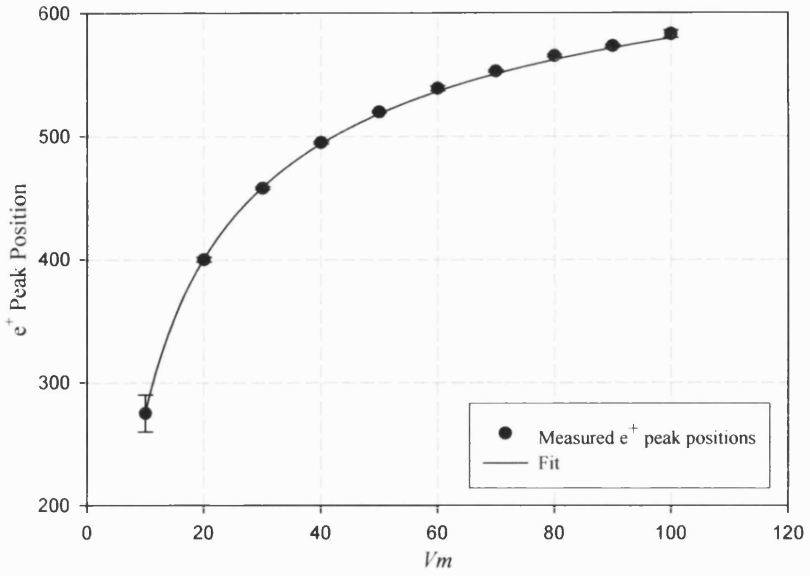

Figure 3.7 Calculated positron peaks fitted to experimentally determined positions.

Figure 3.8 shows the positron energy distributions determined from the time-of-flight spectra, using values for t_{ch} and $|W|+C$ determined above. The time-of-flight peak energy and FWHM of these plots are given in table 3.2. As can be seen from the table, the distribution peaks are in fairly good agreement with values determined using Equation 3.5. Any slight deviation can be attributed to small drifts on the remoderator potential.

V_m (V)	*Peak Energy* (eV)	*FWHM* (eV)
21	22.2±0.1	3.0±0.1
27	27.8±0.1	2.8±0.1
34	34.9±0.1	3.0±0.1
42	42.9±0.1	3.0±0.1

Table 3.2 Summary of the remoderated positron time-of-flight peak energies and FHWM.

The FWHM of the positron energy distributions obtained from the time-of-flight spectra are widened with respect to that obtained by a retarding field analyser by the

system resolutions. For a discussion on the time-of-flight timing resolutions see section 5.6.

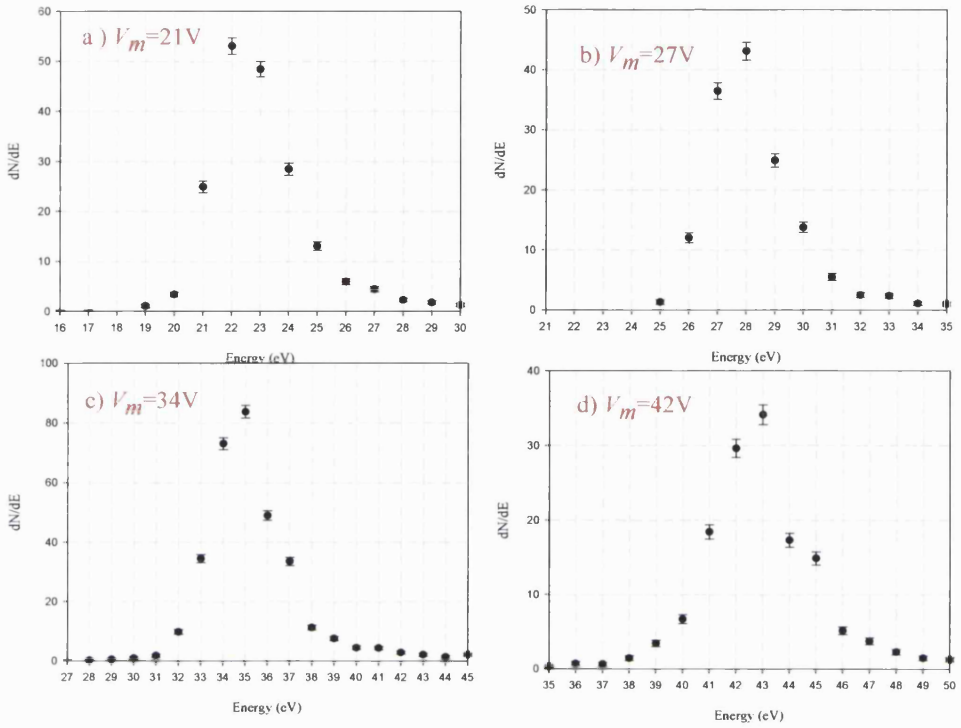

Figure 3.8 Remoderated positron energy distributions determined with the time-of-flight system.

3.2.4 Ps Energy Distributions

The Ps energy spread is calculated from the time-of-flight spectrum using

$$E_{Ps} = m\left(\frac{L_{Ps}}{t_{Ps}}\right)^2, \tag{3.6}$$

where m is the mass of the positron, L_{Ps} is the Ps flight-length and t_{Ps} corresponds to the flight-time for a Ps atom to travel from the middle of the production cell to CEMA2 and is given by

$$t_{Ps} = t_{tof} - t_{e^-} + t_{e^+} - t_{cell}, \tag{3.7}$$

where with reference to figure 3.9, t_{e^-} and t_{e^+} are the acceleration times for secondary electrons and remoderated positrons at the tagger, t_{cell} corresponds to the time taken for a remoderated positron, with energy E_+, to reach the middle of the production cell, t_{tof}, is the measured time between the tagger and CEMA2 pulses respectively and is given by

$$t_{tof} = (t0 - chn_{Ps}) \times t_{ch}, \tag{3.8}$$

where $t0$ is the t=0 channel number (see section 2.7.1), chn_{Ps} is the corresponding Ps peal channel number and t_{ch} is the time-per-channel. A schematic definition of the times needed to determine the Ps absolute energy are shown in figure 3.9.

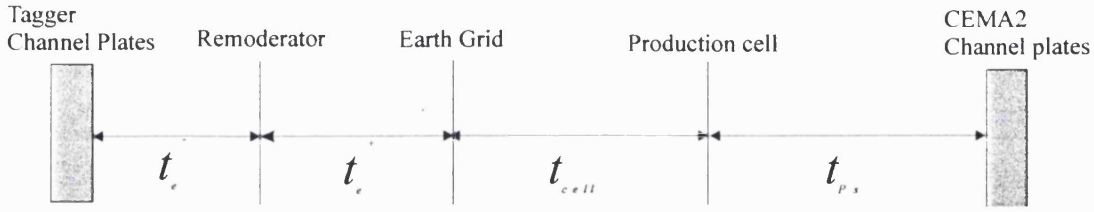

Figure 3.9 Schematic definition of the times relevant to the determination of the Ps absolute energy.

Unlike the positron case (Equation 3.4), no acceleration through the retarding arrangement in front of CEMA2 is required, as Ps is a neutral particle. Figure 3.10 shows an average of all the Ps energy spreads obtained using the time-of-flight detection system. The remoderator potential, V_m, is shown in the upper left hand corner of each plot.

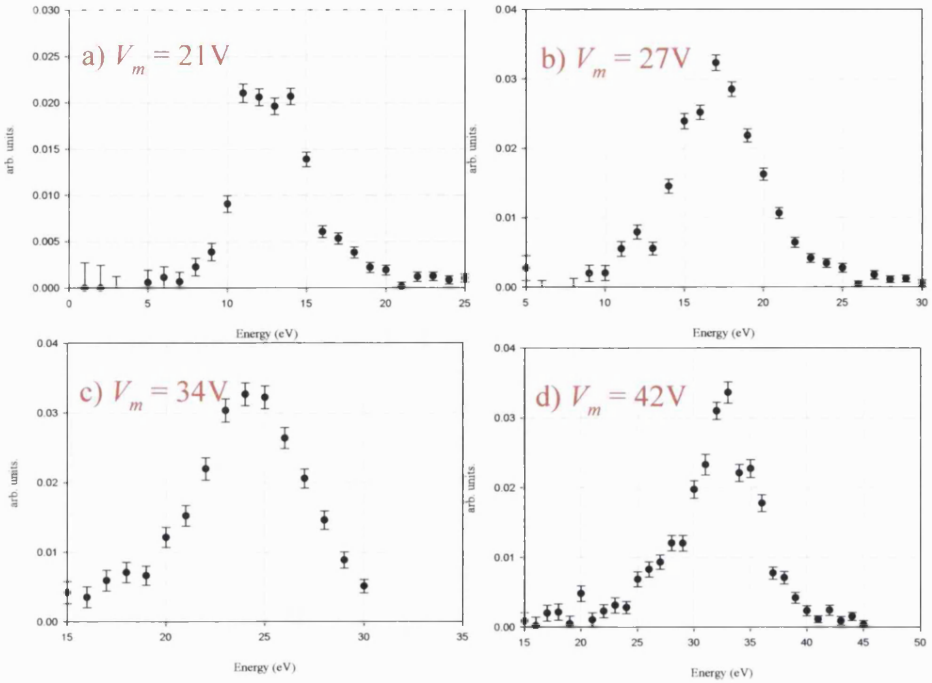

Figure 3.10 Ps energy spreads determined from the time-of-flight spectra.

The full-width-half-maximum, ΔE_{Ps}, of these distributions are shown in table 3.3. The weighted mean of these values is (6.0±0.2) eV, twice that of the positrons as determined in section 3.2.3. In the case of Ps, an additional time spread arises from the spread in the Ps formation points along the production cell, as discussed in chapter 5.

In figure 3.11, the energy distribution for a 32eV Ps beam, formed through charge exchange reaction in H_2 (as described in section 1.5.2), is compared to a 30eV Ps beam obtained by Zafar *et al* (1991), using low pressure He as the production gas (the latter has been shifted by 2eV and normalised to the peak value for comparison). The smaller peak at lower energies, obtained from He, has been interpreted as indicating the presence of Ps^* because it is separated by 5.1eV from the ground state o-Ps peak. As can be seen from figure 3.11, no Ps^* contribution to the beam is apparent in this study.

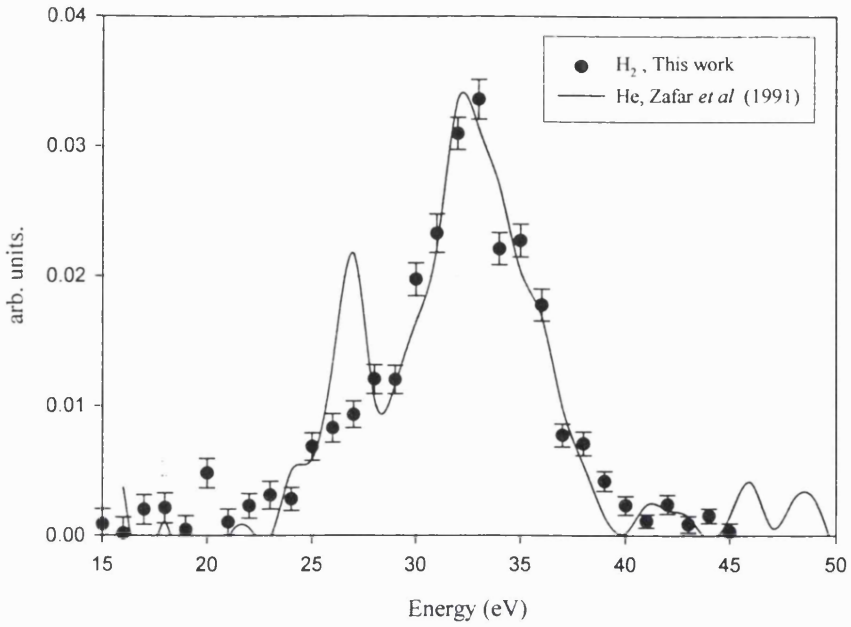

Figure 3.11 Comparison of the energy distribution of 32eV Ps obtained from He and H_2.

To a first approximation (Laricchia *et al*, 1992) the kinetic energy of the Ps beam, E_{Ps}, is given by

$$E_{Ps} = E_{+} - I + B, \tag{3.9}$$

where E_+ is the positron kinetic energy, I is the ionisation energy of the production gas, in this case 15.65eV for H_2 and B is the Ps binding energy (6.8eV for the ground state). By substitution of Equation 3.5, we can rewrite Equation 3.9 as

$$E_{Ps} = eV_m + |W| + C - I + B. \tag{3.10}$$

Table 3.3 compares the Ps peak energies, E_s, taken from the spectra of figure 3.10, with the expected Ps energy, E_{Ps}, calculated using Equation 3.10. Also shown in table 3.3 are the deviations, E_{Ps} -E_s. It cannot be categorically ruled out that the deviations could arise from errors in the determination of the positron/Ps flight lengths used in Equation 3.6. However, a physical effect, which could give rise to a shift in the Ps kinetic energy, would be the occurrence of Ps formation simultaneous to another

inelastic effect, for example, vibrational excitation or molecular dissociation of the target.

Vm **(V)**	ΔE_{Ps} **(eV)**	***Spectrum energy,*** E_s ***(eV)***	***Expected energy,*** E_{Ps} ***(eV)***	$E_{Ps} - E_s$ **(eV)**
21	5.4±0.4	12.5±1.0	13.2±0.4	0.7±1.1
27	5.7±0.3	17.4±0.5	19.2±0.4	1.8±0.6
34	6.4±0.4	24.0±0.5	26.2±0.4	2.2±0.6
42	6.3±0.3	33.0±0.3	34.2±0.4	1.2±0.5

Table 3.3 Comparison of the Ps energy spread and spectrum energy, determined from the time-of-flight spectrum, with the expected Ps energy.

Ps formation from CO_2, simultaneous to the excitation of the remnant ion has been observed to have a large cross-section (Laricchia *et al* 1988, Laricchia and Moxom 1993). If Ps formation resulted in dissociation of the remnant ion, the Ps kinetic energies would be decreased by at least the dissociation energy of H_2^+. Murkherjee and Ghosh (1999) have studied the vibrational excitation of H_2^+ by Ps formation in e^+-H_2 collisions to v = 2, 3, 4 (whose thresholds are 0.6, 0.9, 1.1eV, respectively) and found that the simultaneous occurrence of these processes is probable for 50eV positron impact. Recent triply differential cross-section measurements for ionisation of H_2 by 50eV impact-energy positrons (Köver *et* al, 2001) have shown a shift in the ejected electron energy distribution of approximately 1.6eV, in comparison with a theory that ignores the molecular structure of the target (see section 1.5.1). This suggests that an additional energy loss mechanism may be correlated to positron ionisation of H_2. The energy shifts observed in the present work do seem to support the suggestion that another energy loss mechanism (e.g. molecular excitation/dissociation) is dominantly occurring simultaneous to Ps formation in bound states.

3.3 Ps-He Total Cross Section

3.3.1 Introduction

A brief summary of experimental and theoretical investigations on Ps total cross-sections was presented in section 1.5.3. In this section, total cross-sections of Ps scattering from He, obtained in conjunction with the Ps-He break-up measurements, are presented. At first, the experimental method and data analysis are described. Then the results are presented and compared with other available data.

3.3.2 Experimental Method

Total cross-sections, σ_T, for Ps-He scattering have been obtained via the relationship,

$$\sigma_T = \frac{kT}{PL}\ln\left(\frac{I_0}{I}\right), \tag{3.11}$$

where T is the temperature of the target gas, k is the Boltzmann constant, P is the target gas pressure, L is the effective length of the scattering cell and I and I_0 are the intensities for the incident and transmitted beams, respectively. The random background contribution to the Ps peak was computed from a flat part of the same time-of-flight spectrum and subtracted directly.

The positron beam intensity was measured for 20 seconds at the beginning and end of each Ps beam run and was found to be stable, to within 10%, throughout the course of these measurements. The incident and transmitted Ps beams were measured sequentially at each energy. Typically, the incident Ps beam intensity was measured for 18000s, whilst the transmitted beam intensity was measured for 50000s. The target gas temperature was monitored with a thermometer in good thermal contact with the experimental chamber. An average temperature was obtained from those registered at the beginning and end of each run and an error of $\pm$1K was estimated and propagated through the calculations for σ_T.

3.3.3 Effective Length of the Scattering Cell

Due to the unknown variation of target gas pressure along the length of the scattering cell, an effective cell length, L, has been determined by measuring e^+-He total-cross-sections and normalising them to known total-cross-section values. Since the positron beam is magnetically guided, total cross-section measurements have to be performed with particular care in order to discriminate against forward elastically scattered positrons. This was done by employing a retarder (R1, see section 2.6.3) set 1eV below the positron beam energy such that any positron that has converted longitudinal energy into transverse energy via elastic scattering would not be detected (a review of this method is given by Charlton, 1985).

The incident and transmitted positron beam intensities were measured sequentially for 100s. The effective cell length, L, was then calculated by performing a weighted least-square-fit to a plot of LP versus P, were L is given by

$$L = \frac{kT}{P\sigma_T(e^+)} \ln\left(\frac{I_0}{I}\right). \tag{3.12}$$

The symbols are the same as Equation 3.11, and $\sigma_T(e^+)$ is the corresponding positron total cross-section, measured by Kauppila *et al* (1981). Figure 3.12 shows an example of a plot of LP versus P, for e^+-He scattering. From this plot, the effective length of cell for He was found to be 0.070±0.002m, in excellent agreement with the value determined, for the same scattering cell, by Garner (thesis, 1997) of 0.071±0.001m. The value for the scattering cell length was measured with varying incident positron beam energies and found to be consistent within experimental errors.

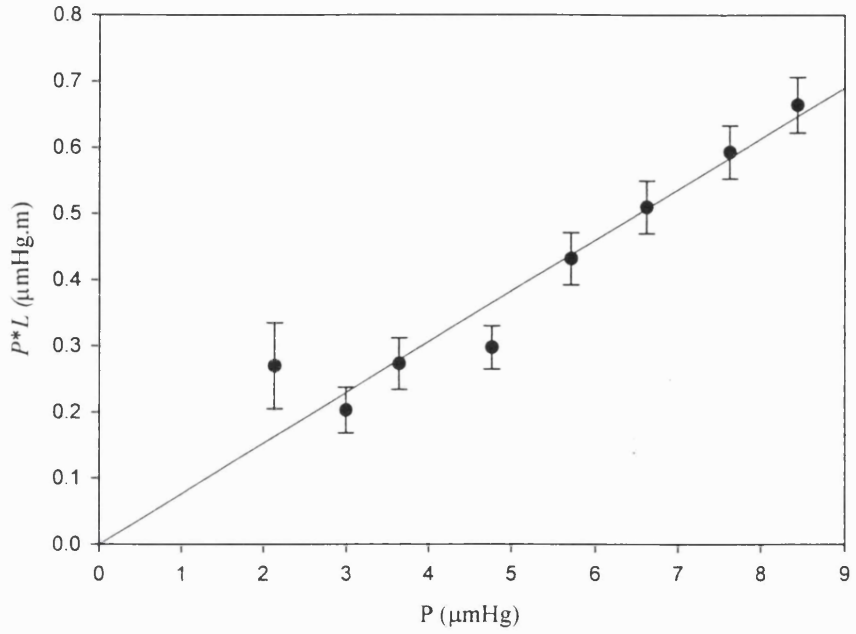

Figure 3.12 An example of a measurement to determine the effective cell length for He (see Equation 3.11). The positron beam energy is 50eV.

3.3.4 Results and Comparison with other Experiments and Theory

Figure 3.13 shows a plot of the total-cross-section values determined in this study, compared with the previous measurements of Garner *et al* (1996). Also shown in figure 3.13 are the total-cross-section values of Garner *et al* (2000), corrected for forward scattering effects, see section 1.5.3. The total-cross-section values obtained in this work for 13 eV and 18 eV were taken with a detection solid angle of 5.3msr and have thus been corrected for forward scattering effects, using the average differential-cross-section values determined by Garner *et al* (2000). The 'true' total cross-section, σ_{True}, may be obtained from the measured cross-section, $\sigma_{measure}$, using

$$\sigma_{True} = \sigma_{measure} + \left\langle \frac{d\sigma}{d\Omega} \right\rangle \Delta\Omega , \tag{3.13}$$

where $\Delta\Omega$ is the detection solid angle and $\langle d\sigma/d\Omega \rangle$ is the differential-cross-section for Ps-He scattering of average value of $(34\pm12)\times10^{-20}m^2sr^{-1}$ across the energy range investigated (Garner *et al*, 2000). The large uncertainty in the low energy total-cross-section values determined in this study, are a convolution of the large uncertainty on the differential cross-section, combined with the large statistical uncertainty inherent with low energy Ps scattering measurements.

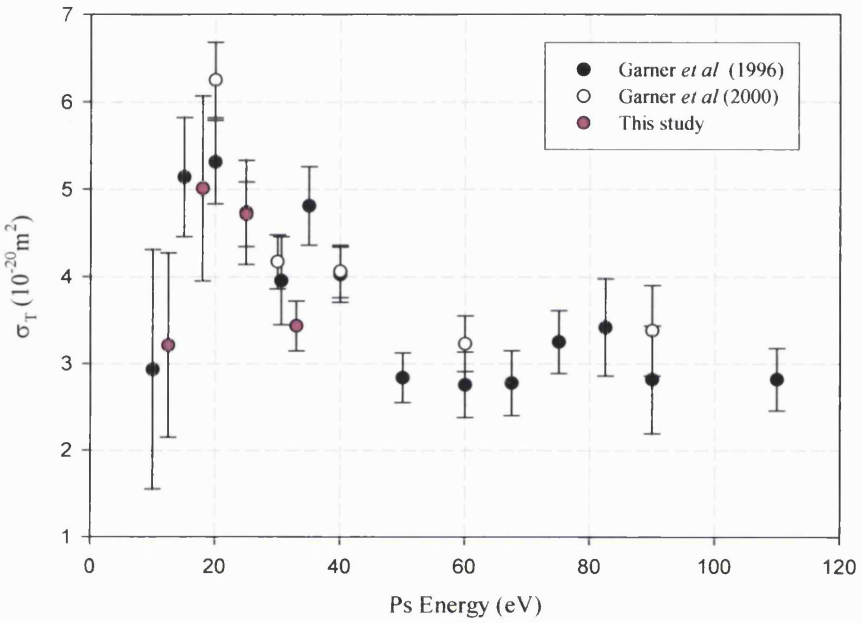

Figure 3.13 Ps-He total cross-section measurements.

As can be seen in figure 3.3, there is a good agreement, within experimental uncertainties, between the Ps-He total cross-section values determined in this study and those of Garner *et al* (1996 and 2000).

Figure 3.14 shows the total-cross-section values determined in this study compared with other experiments and available theories. Given the consistency between the present values and those of Garner *et al* (1996), the reader is referred to section 1.5.3 for a discussion of this plot.

Despite its poor precision, the low energy point (13eV), measured in this work, tends to increase the significance of the discrepancy with the results of Blackwood *et al* (1999). Further work is required at this energy, especially

considering the agreement between the break-up cross-section of Blackwood *et al* (1999) and the results of the present study, as will be discussed in chapter 5.

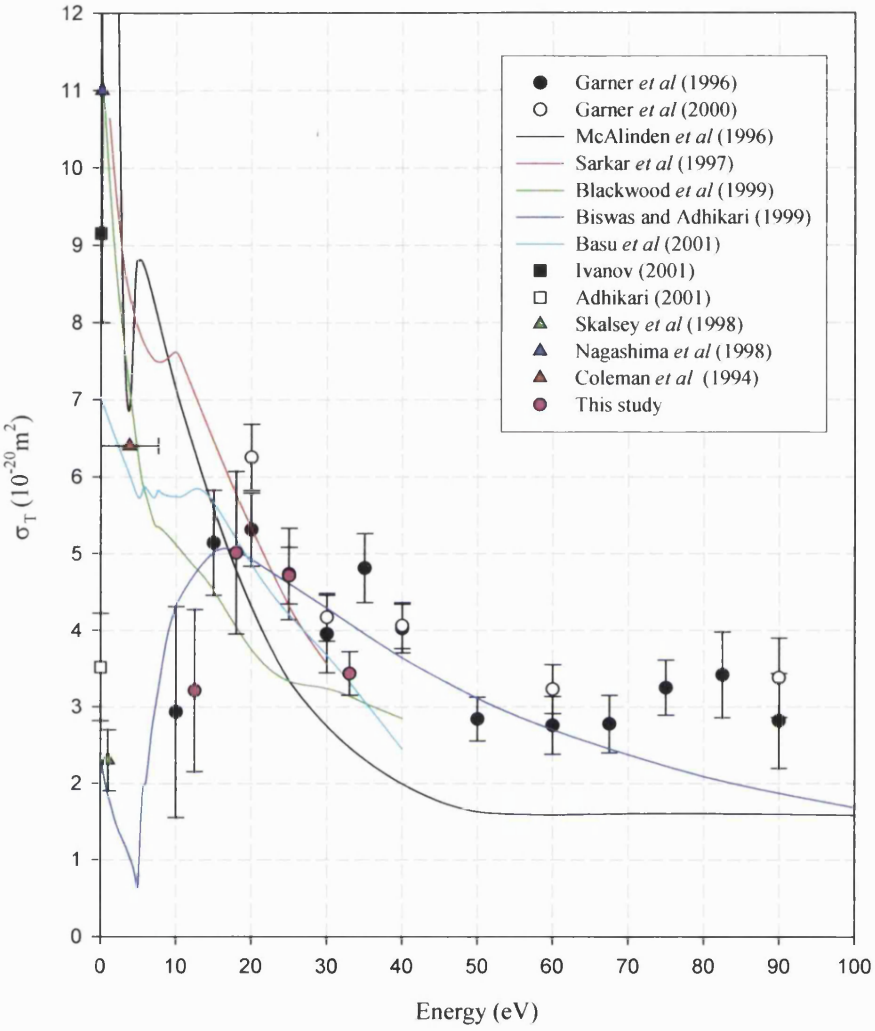

Figure 3.14 Comparison of experimental and theoretical total-cross-section values.

3.4 Summary and Conclusions

The procedures for preparing an Ar RGS moderator have been given, and the slow positron moderation efficiency values found to be consistent with previous efficiencies. Energy spread measurements on the positrons emitted from the Ar RGS moderator (during the growth but after saturation) have been performed using a

retarding field analyser. A reduction in the epi-thermal positron contribution observed and attributed to the larger effective implantation depth for thicker moderators.

The energy distribution of the Ps beam has been determined for each Ps energy, by converting the time-of-flight spectra. The Ps peak energy is found to be shifted from the value expected from the lowest thresholds by approximately 1.5eV. At present the origin of this shift is unknown, but might be related to that observed in the spectrum of the ejected electron in the positron impact ionisation of H_2 (Köver *et* al, 2001).

Ps-He total-cross-section measurements have been performed in conjunction with the Ps break-up study, where good agreement has been found with the previous determination by Garner *et al* (1996). In order to have a better understanding of the Ps-He system, the uncertainty in the low energy Ps-He total cross-sections must be reduced.

Chapter 4
Positron and Positronium Detection Efficiencies

4.1 Introduction

The values of the positron and Ps detection efficiencies and their energy dependences are required in order to determine absolute cross-sections for Ps break-up. Additionally, in the case of Ps, an understanding of the mechanisms at play in its detection may offer possibilities of its improvement.

The detection efficiency of a detector, ε_{det}, corresponds to the fraction of the incident particles that are counted, i.e.

$$\varepsilon_{det} = \frac{N_C}{N_i}, \tag{4.1}$$

where N_C is the number counted by the detector and N_i is the number of incident particles. The detection efficiency of CEMA2, to either a positron or Ps, can be deduced by performing measurements in coincidence with a second detector, in this case a CsI γ-detector placed in its proximity.

After subtracting the relevant background due to fast particles, the total number of counts registered by the CsI detector (N_{CsI}) can be expressed in terms of counts due to correlated events ($(\Delta N_{CsI})_C$) and random events (R_{CsI}), where the correlated events may give rise to a coincidence with CEMA2, i.e.

$$N_{CsI} = R_{CsI} + (\Delta N_{CsI})_C . \tag{4.2}$$

The correlated events may also be expressed as

$$(\Delta N_{CsI})_C = 2\varepsilon_{CsI} N_i , \tag{4.3}$$

where ε_{CsI} is the efficiency of the CsI detector to slow positrons; the factor of 2 in the equation allows for the two-annihilation γ-rays. Similarly, the number of counts detected by CEMA2 may be expressed in terms of both correlated and random events as,

$$\Delta N_{CEMA2} = R_{CEMA2} + (\Delta N_{CEMA2})_C, \tag{4.4}$$

and the number of correlated events as,

$$(\Delta N_{CEMA2})_C = \varepsilon_{CEMA2} N_i, \tag{4.5}$$

where ε_{CEMA2} is the efficiency of CEMA2 to slow positrons. By integrating only over the region of correlated events, the number of coincidences between the two detectors may be rewritten as,

$$\Delta N_{coinc} = \frac{(\Delta N_{CsI})_C (\Delta N_{CEMA2})_C}{N_i}. \tag{4.6}$$

Substituting Equation 4.5 into 4.6 now gives

$$\varepsilon_{CEMA2} = \frac{\Delta N_{coinc}}{(\Delta N_{CsI})_C}. \tag{4.7}$$

In order to obtain an accurate value of the detection efficiency for CEMA2 to positrons (ε_{e^+}) and Ps (ε_{Ps}), it is important that both detectors view the same events and that the background on the CsI is carefully accounted for and removed. Two methods have been used to determine ε_{Ps}. In the first, under the assumption that the detection efficiency depends primarily on the impact velocity, ε_{e^+} for positrons of the same impact velocity as the Ps beam have been determined. In the second method, ε_{Ps} was measured directly using the Ps beam.

4.2 Geometry of the System

To measure the CEMA2 detection efficiencies to positrons and Ps, a coincidence arrangement was set-up between CEMA2 and a CsI detector (see section 2.7.2 for details). Typical coincidence rates for positron detection efficiency measurements were approximately $6\times10^{2}s^{-1}$ with a corresponding CsI rate of approximately $2.5\times10^{3}s^{-1}$. Fluctuations in the background were so small in comparison to the positron rates that they had no effect on the determination of the detection efficiency. However, for detection of Ps a reduction in the background on the CsI detector was required, hence extra Pb shielding was placed around the CsI detector defining a 7mm slit between the CsI detector and CEMA2, as shown in figure 4.1.

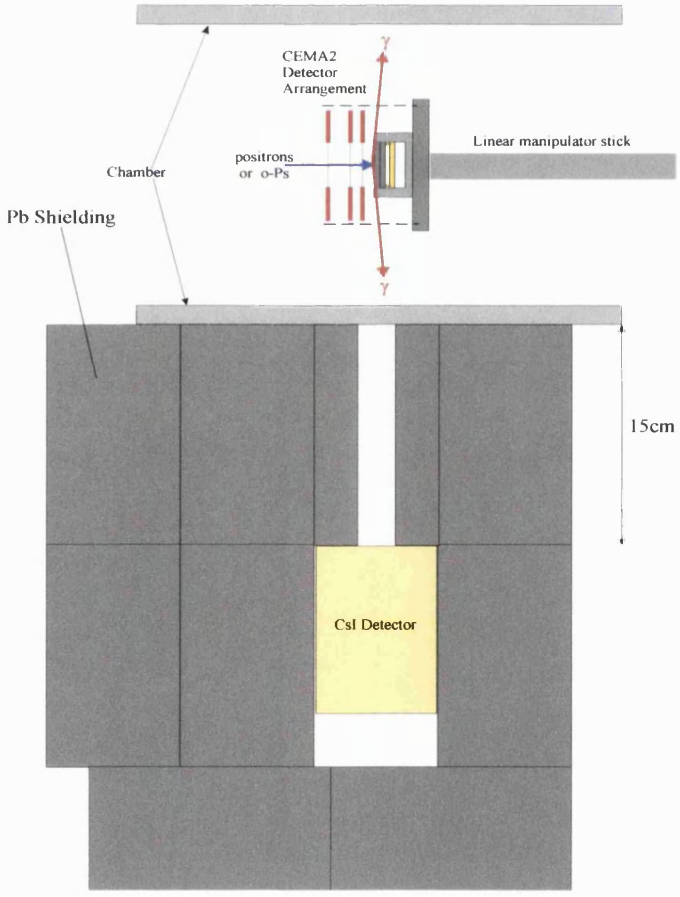

Figure 4.1 CsI – CEMA2 coincidence arrangement - Not to scale.

4.3 Characterisation of the Coincidence System

In order to have a better understanding of the detected signal, measurements were taken for both coincidences and CsI rates for different positions of CEMA2. These were set via the "stick-position" of the linear manipulator, see figure 4.1. For each stick-position, a different part of the CEMA2 detector arrangement was brought into view of the CsI detector. In this way, and by varying the potentials applied to CEMA2, annihilations could be resolved emanating from the channel-plates and each individual grid. Additionally, the background on the CsI detector rate, i.e. counts not correlated to a coincidence, could be evaluated.

4.3.1 Coincidence and Annihilation Measurements

Figure 4.2 shows the coincidence and CsI rates for varying CEMA2 positions with respect to the CsI detector.

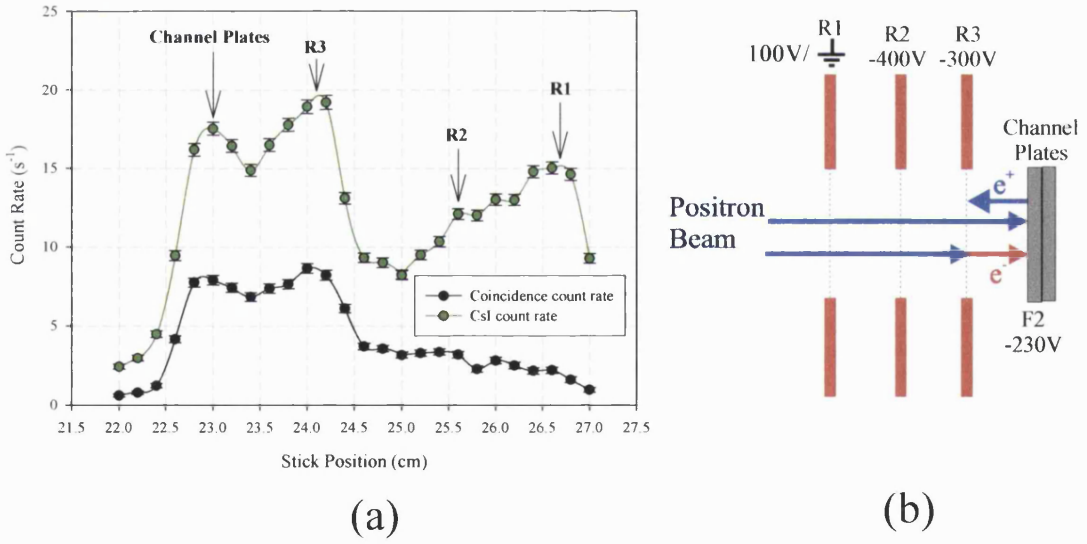

(a) (b)

Figure 4.2 Coincidence and CsI rates versus stick position (a), obtained using the CEMA2 configuration illustrated in (b).

As illustrated in figure 4.2 (a), annihilations and coincidences can be distinguished emanating from the channel-plates and the three grids, R1, R2 and R3. The annihilations (γ) on R1 and R2 are predominantly from the incident positron beam, as $\gamma(R1) > \gamma(R2)$. Any incident positron, which releases a secondary electron from and then annihilates at either R2 or R3, can give rise to a coincidence. However,

as can be seen from figure 4.2 (a), coincidences are also seen correlated to positron annihilation at R1, although, with reference to figure 4.2 (b), secondary electrons from R1 cannot reach the channel-plates due to the potential applied to the R2. Therefore, the few coincidences at R1 must arise from positrons re-emitted/backscattered from the channel-plates. Since, for the incident positron beam it would be expected that $\gamma(R1) > \gamma(R2) > \gamma(R3)$, the annihilations recorded at R3 must arise predominantly from re-emitted/backscattered positrons. By grounding all the grids, secondary electrons

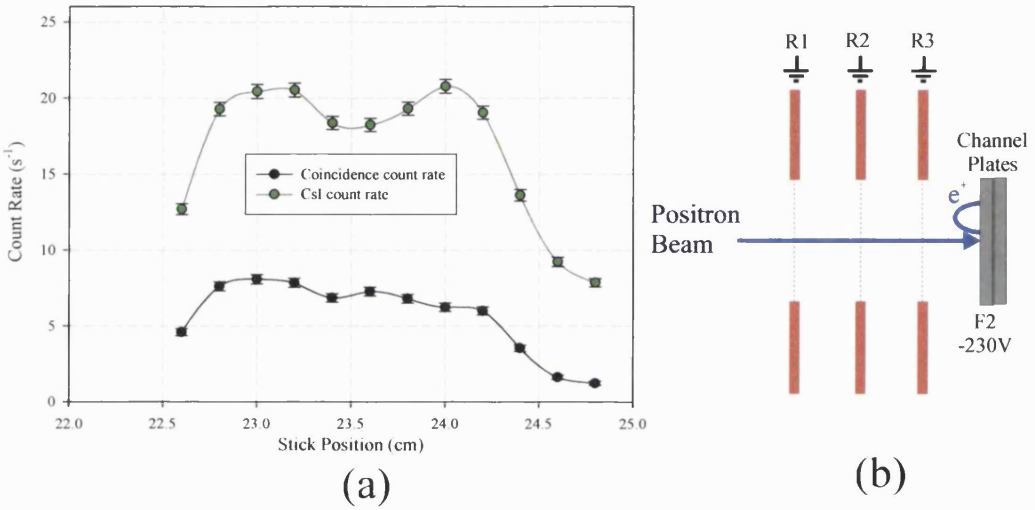

Figure 4.3 Coincidence and CsI rates versus stick-position (a), obtained using the CEMA2 configuration illustrated in (b).

released from there will not be accelerated to the channel-plates. As can be seen in figure 4.3 (a), a reduction in the coincidences from R3 is evident, as the secondary electrons released by the incident positron beam from this grid cannot reach the channel plates. Therefore, the coincidences recorded at R3 must arise from secondary electrons released at the channel plates. With all the grids grounded, any coincidence correlated to annihilation on the grids must therefore arise from positrons re-emitted/backscattered from the surface of the channel-plates.

4.3.2 Conclusions

From the coincidence and CsI rate measurements, taken at different "stick-positions", a contribution arising from re-emitted/backscattered positrons from CEMA2 has been distinguished. With reference to the positron detection efficiency, any elastic scattering from the surface of CEMA2, followed by annihilation away from the field of view of the CsI detector, will lead to an overestimate of its detection

efficiency. In order to determine 'true' detection efficiencies, a measure of the elastic scattering from the surface of the detector is required.

As approximately 50% of the coincidences are correlated to a positron that annihilates at R3, the slit defining the field of view of the CsI detector was increased to 15mm. In this way both the channel-plates and R3 are viewed by the CsI detector, thus leading to an improved data collection rate.

4.4 Equivelocity Positron Method

Positrons incident upon CEMA2 are accelerated by a potential of –230V applied to the front of the plates. The energy range of positrons used in this study was 0 to 50eV, corresponding to impact energy in the range 230eV to 280eV. Figure 4.4 shows typical detection efficiencies for a channel electron multiplier (CEM) to various projectiles. As can be seen from figure 4.4, the detection efficiency for electrons varies very little across the impact energy range of this study. This is in accord with the detection efficiency for positrons measured in this study by measuring the coincidence and CsI rates for incident positrons, as described in the introduction. The background was measured with the retarders R1 and CR1 on. The positron detection efficiency, ε_{e^+}, was calculated across the energy range, using Equation 4.7 and found to be 0.51±0.01.

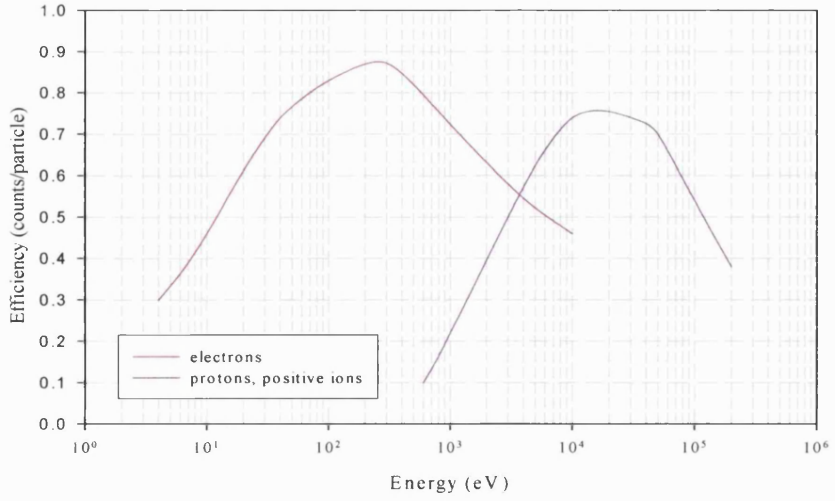

Figure 4.4 Typical detection efficiencies for electrons, protons and positive ions ("Electron Multipliers", Phillips Components, 1991).

Of course, being neutral Ps is not accelerated into the surface of the channel-plates and will impact with a lower impact velocity than the incident positrons. If, as suggested by figure 4.4, across the energy range of this study the dominant factor in determining the detection efficiency is the impact velocity, it would be expected that the detection efficiency of Ps should vary significantly. As a first order approximation to the Ps detection efficiency, we have measured the detection efficiency of positrons with the same impact velocity as that of the Ps atoms used in this study. The results of this study are presented in the following subsections.

4.4.1 Experimental Procedure

The impact velocity of positrons was varied by changing the potential on the front of the channel-plates. The potential difference across the plates was fixed throughout the study, so as to keep the secondary electron gain constant. Rates for the incident positrons and background were measured for 100 seconds. Both coincidences and CsI rates were measured at each respective positron impact velocity. The detection efficiencies were calculated using Equation 4.7 .

4.4.2 Results

The detection efficiencies, ε_{e^+}, for "equivelocity positrons" i.e. with velocities comparable to those of Ps used in this study, are shown in figure 4.5. As can be seen there is a slight increase in the detection efficiency values from (16.0±0.6)% to (17.9±0.6)% as the impact velocity is increased.

A closer correspondence with figure 4.4 would not be expected as efficiency curves for CEMs vary, even for the same type of CEM, see review by Seah (1990) and data given by Bennani *et al* (1973) and Olsen *et al* (1979).

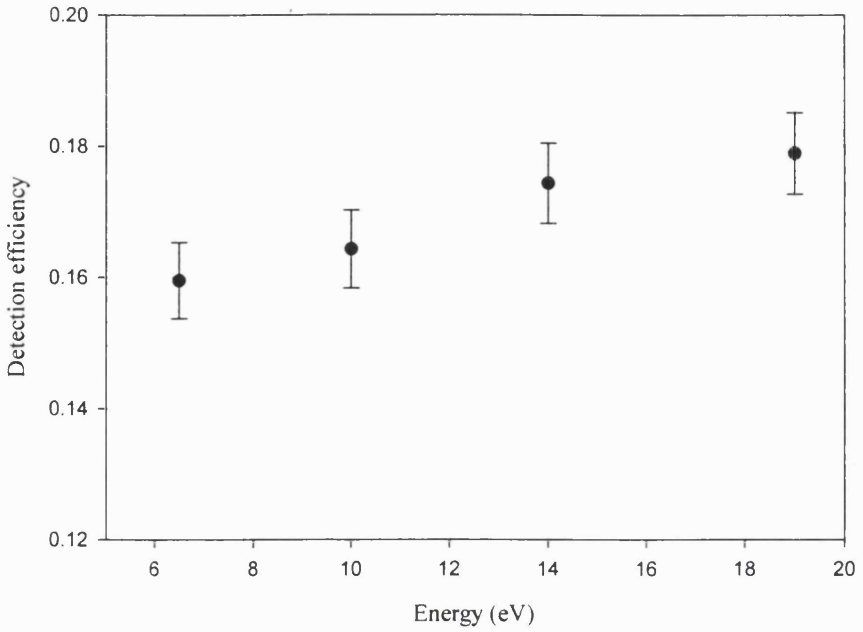

Figure 4.5 Detection efficiencies for equivelocity positrons.

Because of the importance of these values for the absolute determination of the break-up cross-section and the remaining uncertainty on how closely this efficiency would correspond to that of a neutral composite particle such as Ps, we set out to measure this efficiency explicitly, although as discussed below, these measurements pose considerable difficulty.

4.5 Direct Ps Detection Efficiency

The Ps detection efficiency, ε_{Ps}, is determined using Equation 4.7. Particularly important in these types of measurements is an accurate determination of all the backgrounds inherent within the experiment. The total number of CsI counts, γ_{total}, measured when detecting Ps is given by,

$$\gamma_{total} = \varepsilon_4 N_i + \left(\varepsilon_{inflight} + \varepsilon_{Grids}\right) N_i + \gamma_{amb} + \gamma_{Pos}, \tag{4.8}$$

where N_i is the incident number of Ps atoms and ε_4 is the efficiency of the CsI detector for positrons annihilating at CEMA2. Due to the finite lifetime of Ps, a fraction of atoms will annihilate before reaching CEMA2 and give rise to an extra contribution to the CsI rate, proportional to the incident Ps beam and detected with efficiency $\varepsilon_{inflight}$. A background may be associated with annihilations at the grids R1, R2 and R3 in

front of the channel-plates, proportional to the incident Ps beam and detected with efficiency ε_{Grids}, the sum of the detection efficiency for each respective grid ($\varepsilon_1 + \varepsilon_2 + \varepsilon_3$). γ_{amb} is the ambient background CsI rate, measured with vacuum in the production cell. When producing Ps, H_2 gas is inserted in the production cell. In principle, positrons that scatter from the production gas may annihilate on the production cell to give rise to an extra background, γ_{Pos}.

With reference to figure 4.2, a coincidence between the channel plates and the CsI detector may be achieved through a Ps atom releasing a secondary electron and annihilating at either of the grids R2 and R3, as well as through impact at the channel plates. Therefore, the counts recorded by the CsI detector which may give rise to a coincidence are given by

$$(\Delta N_{CsI})_C = \varepsilon_4 N_i + (\varepsilon_2 + \varepsilon_3) N_i, \tag{4.9}$$

where ε_2 and ε_3 correspond to the CsI detection efficiency for Ps annihilation at the grids R2 and R3 respectively. By comparison with Equation 4.8 we can rewrite Equation 4.9 as

$$(\Delta N_{CsI})_C = \gamma_{total} - \gamma_{amb} - \gamma_{Pos} - (\varepsilon_{inflight} + \varepsilon_1) N_i. \tag{4.10}$$

From Equations 4.9 and 4.10, N_i may be written as

$$N_i = \frac{\gamma_{total} - \gamma_{amb} - \gamma_{Pos}}{(\varepsilon_4 + (\varepsilon_2 + \varepsilon_3) + (\varepsilon_{inflight} + \varepsilon_1))}, \tag{4.11}$$

which may be substituted back into Equation 4.10 to find the number of annihilations measured by the CsI which may give rise to a coincidence. This number may then be used in Equation 4.7 with the measured coincidence rate to give the Ps detection efficiency. All the measured quantities and the respective detection efficiencies will be considered in turn and evaluated in the next subsections.

4.5.1 Raw Ps Detection Efficiency Measurements, γ_{total} and γ_{amb}

The coincidence and CsI rates were measured with gas and vacuum in the production cell for 7200 seconds, to determine γ_{total} and γ_{amb} respectively. The CsI

rates were monitored using a multi-channel-scalar card (MCS-Plus, EG&G Ortec). Every CsI spectrum was checked for noise and restored, if necessary by removing obvious noise peaks (i.e. greater than ten times the spectrum average without that noise peak, see figure 4.6). The total number of counts in the spectrum was then computed to give the net CsI rates (γ_{total} and γ_{amb}).

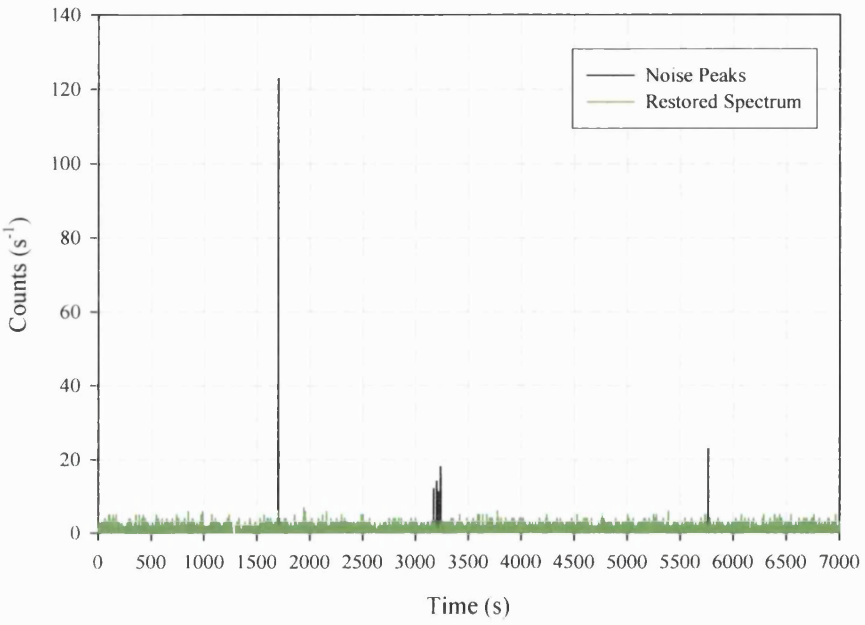

Figure 4.6 The raw and restored CsI spectrum obtained with gas in the production cell.

4.5.2 Positron Annihilation in the Production Cell, γ_{Pos}

To evaluate a possible contribution to the CsI rate from scattered positrons annihilating in the production cell, the CEMA2 detector arrangement was moved as close to the cells as possible. In this way, any Ps formed would be stopped at CEMA2 and not reach the vicinity of the slit. Measurements were hence made for the CsI rate, with and without gas in the production cell. The pressure of the production gas was kept the same as for all the Ps measurements made within this study, i.e. P_{H2} = 10μmHg. Table 4.1 shows the CsI rates for both gas and vacuum in the production cell.

	Gas in production cell	***Vacuum in production cell***
CsI Rate (s^{-1})	1.065±0.008	1.064±0.004

Table 4.1 CsI rates with gas and vacuum in the production cell.

No difference is seen, within errors, between the CsI rates with and without gas in the production cell and therefore we have taken γ_{Gas} to be equal to zero.

4.5.3 In-flight Ps Decay, $\varepsilon_{inflight}$

In this section, the effective efficiency of the CsI detector to the inflight annihilation of Ps atoms is calculated. The fraction, F_s, of the incident Ps beam that survives, as a function of flight length L, is given by

$$F_s(L) = \exp\left(-\frac{L}{\tau_{Ps}}\left(\frac{m}{E}\right)^{\frac{1}{2}}\right), \tag{4.12}$$

where m is the mass of the positron, E is the Ps kinetic energy and τ_{Ps} is the o-Ps lifetime. The fraction of Ps atoms, F_i, which self-annihilate between two flight lengths L and L+1cm are given by

$$F_i = F_s(L) - F_s(L+1cm). \tag{4.13}$$

We have calculated F_i for Ps atoms within 1cm intervals to match measurements taken at the same intervals along the Ps flight length. Figure 4.7 shows the variation of F_s and F_i with flight length for 33eV Ps.

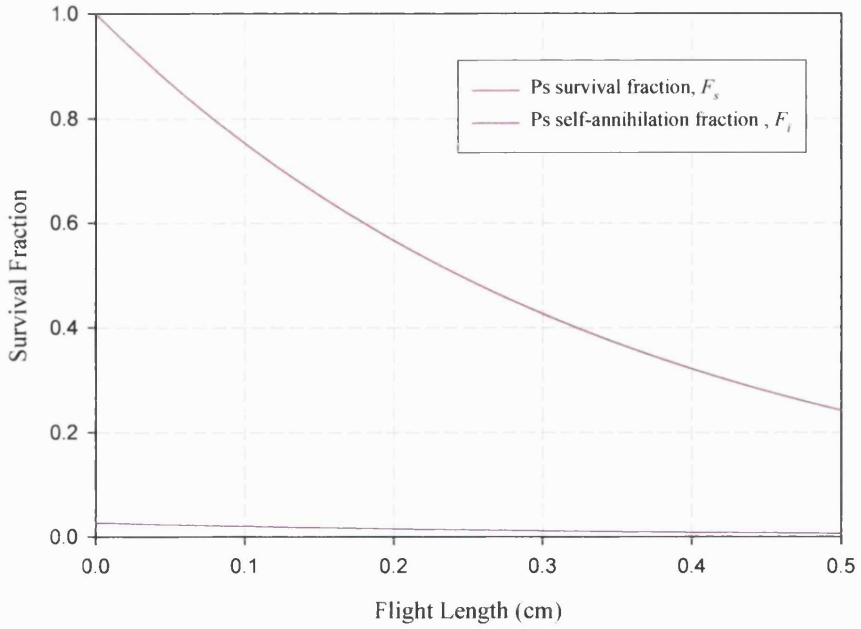

Figure 4.7 Variation with flight length of the survival and self-annihilation fractions at 33eV.

In order to estimate how many γ-rays from in-flight Ps annihilation are counted by the CsI detectors, CsI rates, N_{γ}, were measured as a function of CEMA2 stick position for the incident positron beam. With the incident positron beam annihilating at the channel-plates, CEMA2 acts as a source of γ-rays with a flux F_{γ} given by

$$F_{\gamma} = \frac{2N_{Li}}{\varepsilon_{e^+}}, \tag{4.14}$$

where N_{Li} is the CEMA2 rate for flight-length L_i (which was found to vary slightly due to the transport efficiency), ε_{e^+} is the positron detection efficiency of CEMA2 with normal potentials applied (0.51±0.01) and 2 accounts for the number of γ-rays emitted predominantly in free positron annihilation. In this way, a CsI shielding-factor, S_i, along the flight length, may be calculated

$$S_i = \frac{N_{\gamma}}{F_{\gamma}}. \tag{4.15}$$

Figure 4.8 shows the CsI shielding-profile. Naturally the majority of γ-rays detected by the CsI detector occur in the region of the slit. The CsI rate drops as CEMA2 moves towards the cells (i.e. as the flight length decreases), firstly due to the extra amount of Pb that shields the CsI detector and secondly due to the solid angle effect. Once CEMA2 is beyond the slit, the thickness of the Pb does not change and the reduction in CsI rate is governed by the solid angle effect alone.

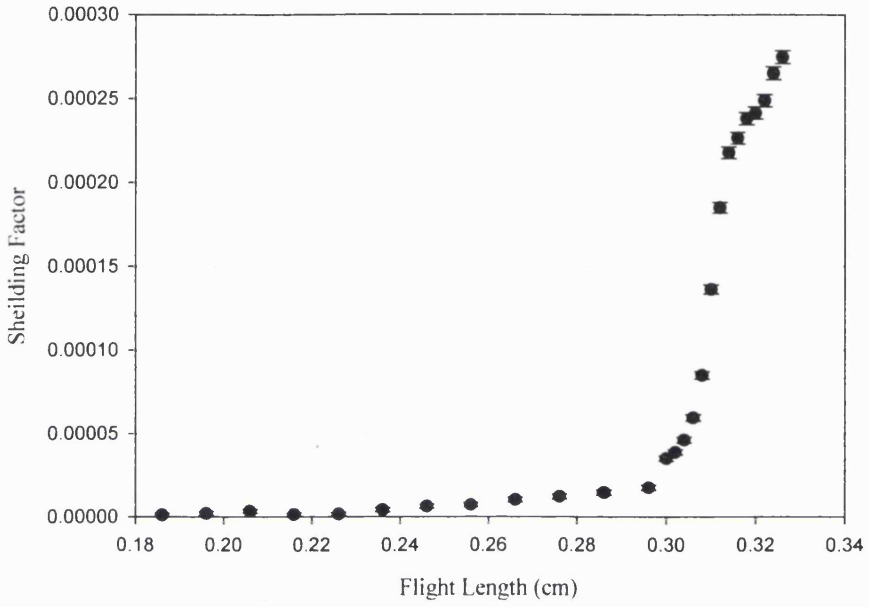

Figure 4.8 CsI shielding profile.

By convoluting the fraction of Ps atoms annihilating within each cm, F_i, with the measured CsI shielding factor, S_i, the effective efficiency for γ-rays seen by the CsI detector from in-flight Ps decay can be calculated:

$$\varepsilon_{inflight} = 3\times\sum_{i=0}^{R1} S_i F_i + 2.7\times\sum_{i=R1}^{R2} S_i F_i + 2.43\times\sum_{i=R2}^{R3} S_i F_i + 2.19\times\sum_{i=R3}^{CP} S_i F_i \,, \qquad (4.16)$$

where 3 accounts for the number of γ-rays emitted predominantly in o-Ps decay and the second, third and fourth terms take into account 10% attenuation of the Ps beam through each of the three grids infront of the channel plates.

4.5.4 Annihilations at the Grids, ε_{Grids}

As shown in figure 4.8, the majority of background γ-rays, detected by the CsI detector come from the region in front of CEMA2 where the slit is positioned. Any

annihilation on the retarding grids will hence contribute to the background γ-rays detected by the CsI detector, due to their close proximity to the slit. As the grids used in this study are nominally 90% transmission grids, 10% of the incident Ps beam will annihilate at each grid. To calculate the effective efficiency of the CsI detector to Ps annihilation on the grids, the fraction of the Ps beam annihilating at each respective grid is convoluted with the CsI shielding factor for the position of that grid. The effective efficiency of the annihilations, as seen by the CsI detector, due to the attenuation of the incident Ps beam at R1, is given by

$$\varepsilon_{R1} = 0.1 \times 2 \times 1.37 \times S_{R1} \times \exp\left(-\frac{L_{R1}}{\tau_{Ps}} \left(\frac{m}{E} \right)^{\frac{1}{2}} \right), \tag{4.17}$$

where S_{R1} is the shielding factor, taken from figure 4.8 at the position of the grid R1, 2 takes into account the decay mode of quenched o-Ps and L_{R1} is the Ps flight length to R1 and the 1.37 corrects for the transmission through the grids, as the incident beam is defined with respect to that impacting the channel plates. Similarly for R2, the fraction of annihilations is given by

$$\varepsilon_{R2} = 0.1 \times 2 \times S_{R2} \times 1.23 \times \exp\left(-\frac{L_{R2}}{\tau_{Ps}} \left(\frac{m}{E} \right)^{\frac{1}{2}} \right), \tag{4.18}$$

where the symbols are the same as for Equation 4.17 with the 1.23 to take into account the transmission through grids R2 and R3. The effective efficiency of the CsI detector to Ps annihilation at R3 is calculated in exactly the same way as for R1 and R2, i.e.

$$\varepsilon_{R3} = 0.1 \times 2 \times S_{R3} \times 1.11 \times \exp\left(-\frac{L_{R3}}{\tau_{Ps}} \left(\frac{m}{E} \right)^{\frac{1}{2}} \right). \tag{4.19}$$

4.5.5 Fraction of Ps Beam Annihilating at CEMA2, ε_4

The effective efficiency of the CsI detector to Ps atoms which annihilate at CEMA2 is given by the fraction that has survived to impact the plates, convoluted with the CsI shielding factor for the position of CEMA2:

$$\varepsilon_4 = 2 \times \exp\left(-\frac{L_{CEMA2}}{\tau_{Ps}} \left(\frac{m}{E} \right)^{\frac{1}{2}} \right) \times S_{CEMA2}, \tag{4.20}$$

where 2 takes into account the mode of decay for quenched o-Ps. S_{CEMA2} is the shielding factor at the position of CEMA2 and L_{CEMA2} is the Ps flight-length to CEMA2.

4.5.6 Results

Figures 4.9(a,b,c) show the individual Ps detection efficiency values calculated using Equations 4.7, taking full account of the backgrounds on the CsI detector using Equation 4.10, as determined in the previous sections (4.5.1-4.5.5).

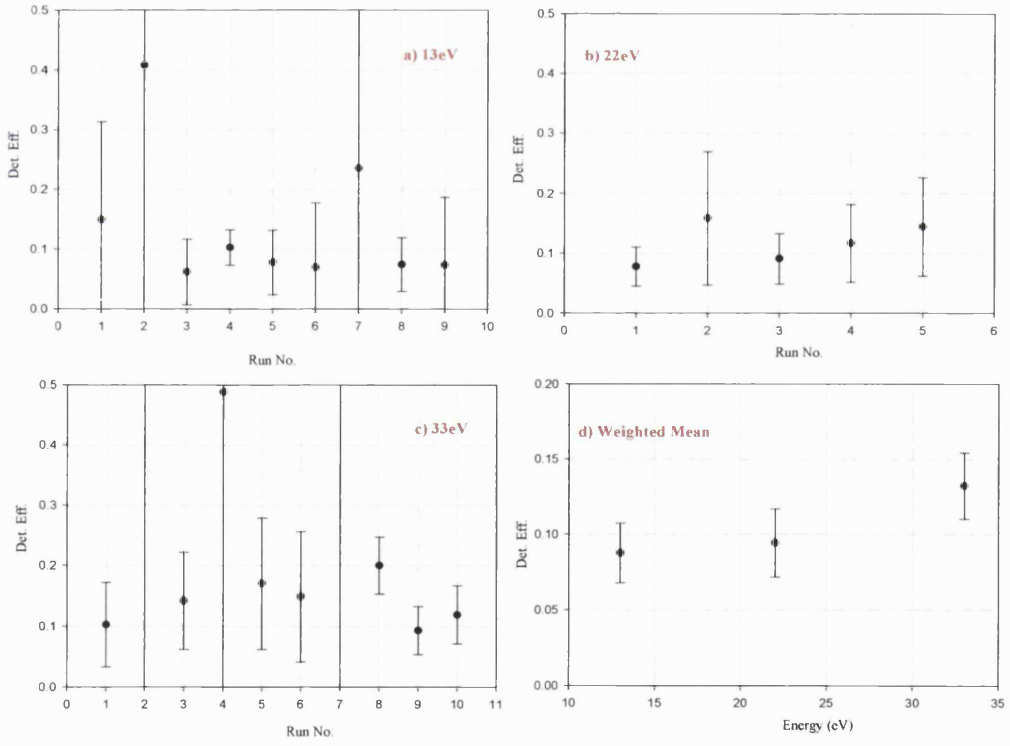

Figure 4.9 Raw Ps detection efficiency measurements.

For each Ps energy, the weighted mean of all the measurements has been taken and are shown in figure 4.9 (d). As can be seen from this figure, the Ps detection efficiency increases from 9±2% to 13±2% across the energy range of this study.

Figure 4.10 shows a comparison of the raw Ps detection efficiencies and those obtained with equivelocity positrons.

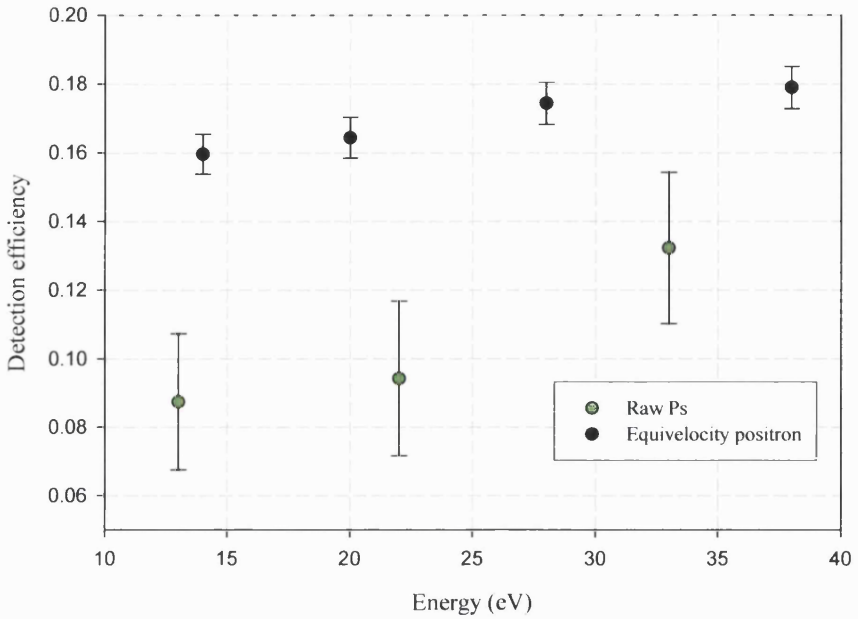

Figure 4.10 Comparison of the raw Ps and equivelocity positrons detection efficiencies.

4.5.7 Fraction of Ps Atoms Elastically Scattering and Breaking Up from the Surface of the Channel-plates

As can be seen from figure 4.10, the detection efficiencies obtained with the equivelocity positrons are approximately twice as large as for those obtained for Ps. A reduction in the measured Ps detection efficiencies would be apparent if elastic scattering and break-up of Ps atoms from the surface of the channel plates are significant effects. If Ps atoms are elastically scattered from the surface of the channel-plates, then an extra contribution to the CsI rate will arise from the attenuation at the grids and the in-flight annihilation of these Ps atoms. Weber *et al* (1988) have observed the elastic scattering of energetic Ps from LiF. At a Ps energy of 7eV, they found at 50° a maximum reflected fraction R= (30±5)%, reducing to (0.5±2.0)% at 60eV. Which suggests that in the energy range of this study, inflight annihilation of Ps elastically scattered from the surface of CEMA2 may be contributing to the background on the CsI rate. From the Ps annihilation spectrum from positrons incident upon a number of target materials, a fast lifetime component, attributed to Ps break-up, has been determined by Gidley *et al* (1995), in the incident positron energy range 0.3 to 10 keV. By extrapolating the data obtained by Gidley to

positron energies used in this study we found a value of 0.10 for the Ps break-up probability, suggesting that in the energy range of this study Ps break-up from the surface of the channel plates may also be affecting the measured Ps detection efficiencies.

In order to obtain true detection efficiencies, Equations 4.10 and 4.11 need to be modified to include elastic scattering from and break-up of Ps atoms at the surface of the channel plates. The incident Ps beam can now be written as,

$$N_i = N_P + N_e + N_{bu}, \tag{4.21}$$

where N_e and N_{bu} are the number of Ps atoms that elastically scatter and break-up from the surface of the channel plates respectively. If α^0 is the probability of a Ps atom annihilating at the channel plates, N_P can be expressed as

$$N_P = \alpha^0 N_i, \tag{4.22}$$

The number of Ps atoms that break-up on the channel plates can be written as

$$N_{bu} = z(1-\alpha^0)N_i, \tag{4.23}$$

where z is the Ps break-up probability. The number of Ps atoms that elastically scatter from the channel plates may hence be expressed as:

$$N_e = (1-\alpha^0)(1-z)N_i. \tag{4.24}$$

The total number of CsI counts, γ_{total}, measured when detecting Ps can now be written as:

$$\gamma_{total} = \alpha^0 \varepsilon_4 N_i + (\varepsilon_{inflight} + \varepsilon_{Grids})N_i + (1-\alpha^0)(1-z)(\varepsilon'_{inflight} + \varepsilon'_{Grids})N_i + z(1-\alpha^0)N_i A + \gamma_{amb} + \gamma_{Pos} \tag{4.25}$$

where the primed symbols refer to elastically scattered Ps atoms and A accounts for the annihilations from positrons released through Ps break-up and is given by

$$A = \varepsilon^{*}_{Grids} + \sum_{n=1}^{5}(1-x)^{4n}\left[\alpha^{+}\varepsilon_4 + (1-\alpha^{+})\left\{F_{Ps}\left(\varepsilon^{Ps}_{Grids} + \varepsilon^{Ps}_{inflight}\right) + F_e\varepsilon^{*}_{Grids}\right\}\right]. \quad (4.26)$$

F_{Ps} and F_e are the Ps formation and elastic scattering branching ratios respectively (these will be discussed further in section 4.6), α^{+} is the probability of the positron annihilating at the channel plates. ε^{*}_{Grids} accounts for the attenuation of the residual positrons at the grids R2 and R3 as they are reflected towards to the channel plates by the potential applied to the grid R1 (see figure 4.2 for the grid potentials). Each time the residual positrons are accelerated back to the channel plates a fraction forms Ps and a fraction is elastically scattered. The elastically scattered fraction is then accelerated back through the grids R2 and R3 to the channel plates. Given the attenuation at the grids and the fact that a fraction will form Ps each time they are re-emitted from the channel plates, the residual positrons will only traverse the grids R2 and R3 to the channel plates 5 times before being attenuated to 1% of their original intensity. The contribution from inflight annihilation of the Ps atoms was determined assuming that the reflected positrons formed 1eV Ps (Mondal and Hamatsu, 2001). The counts recorded by the CsI detector which may give rise to a coincidence are the same as Equation 4.10, i.e.

$$\left(\Delta N_{CsI}\right)_C = \gamma_{total} - \gamma_{amb} - \gamma_{Pos} - \left(\varepsilon_{inflight} + \varepsilon_1\right)N_i. \quad (4.27)$$

Equations 4.25 and 4.27 may now be used to find the incident Ps beam,

$$N_i = \frac{\gamma_{total} - \gamma_{amb} - \gamma_{Pos}}{\left(\alpha^0\varepsilon_4 + (\varepsilon_2 + \varepsilon_3) + (\varepsilon_{inflight} + \varepsilon_1) + (1-\alpha^0)(1-z)(\varepsilon'_{inflight} + \varepsilon'_{Grids}) + z(1-\alpha^0)A\right)}. \quad (4.28)$$

This can be substituted back into Equation 4.27 in order to calculate the number of annihilations measured by the CsI detector that may give rise to a coincidence. The modified CsI rate may then be used in Equation 4.7 to give the true Ps detection efficiency.

To estimate the fraction ($1-\alpha^0$) of the incident Ps beam that might be reflected from the channel-plates, ratios have been computed for the elastic-cross-section to the total-cross-section (σ_e/σ_T) for Ps scattering from H, He, Ar and Ne as calculated by Walters *et al* (2001), Campbell *et al* (1998) and Blackwood *et al* (1999). These ratios

are shown in figure 4.11 with the Ps reflection fractions from LiF as determined by Weber *et al* (1988).

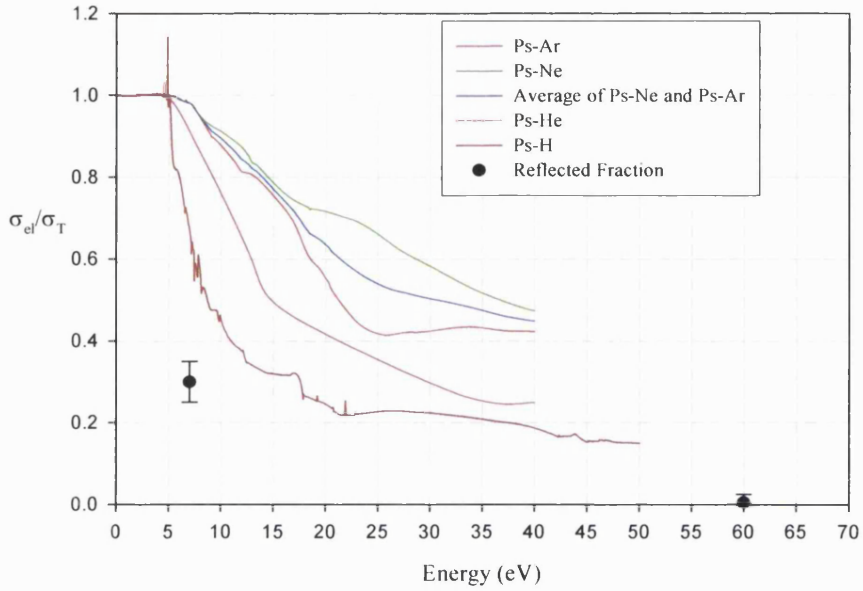

Figure 4.11 Ratio of elastic to total cross-sections for Ps-Atom scattering.

As can be seen from figure 4.11, below 5.1eV the ratios of σ_{el}/σ_T are equal to one, as elastic scattering is the only scattering channel below the Ps excitation threshold. Above this value σ_{el}/σ_T reduces, whereby the larger the target the faster the decrease, apart from Ne, which shows the slowest decrease across this energy range. In comparison with the LiF results, the atomic data would seem to overestimate the reflection probability. As no data are available specifically for Ps scattering from channel-plates (which are predominantly made of SiO_2), the average of σ_{el}/σ_T for Ar and Ne has been used as an upper limit for the elastic scattering fraction. The values of the elastic to total cross-section ratio, used to correct the measured Ps detection efficiencies, are shown in table 4.2.

Energy (eV)	σ_{el}/σ_T
13	0.84
22	0.58
33	0.48

Table 4.2 Average values of σ_{el}/σ_T for Ar and Ne scattering of Ps.

The fraction of Ps atoms that break-up on the surface of the channel plates has been taken as 0.10 from Gidley *et al* (1995). The Ps detection efficiencies, corrected for elastic scattering and break-up of Ps atoms from the surface of the channel plates are shown in figure 4.12, where they are compared with the raw detection efficiencies. As can be seen in figure 4.12, the correction results in an increase of approximately 40% at 13eV, where the magnitude of the elastic to total cross section is largest. The correction decreases to 10% at 33eV.

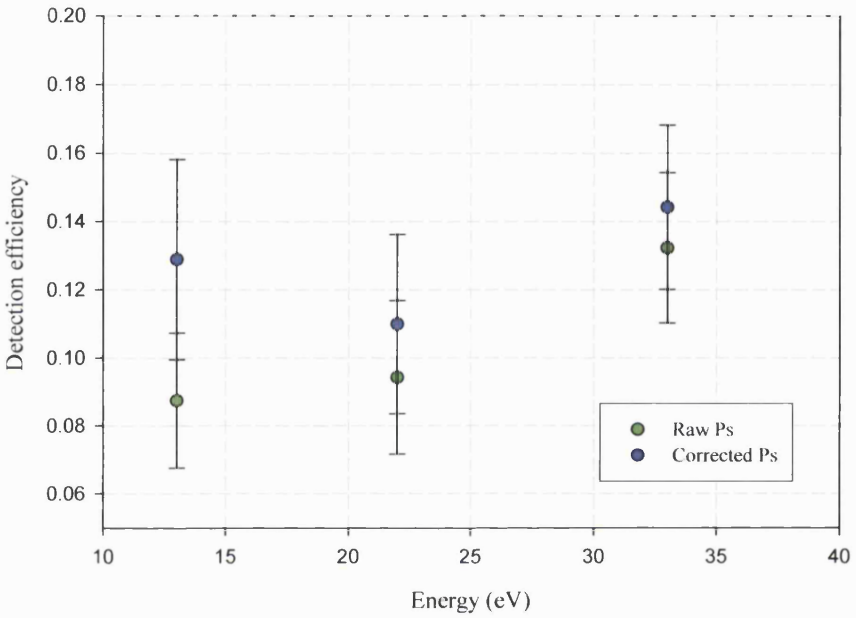

Figure 4.12 Comparison of the raw Ps detection efficiencies to the corrected detection efficiency.

In figure 4.13, the variation of the Ps detection efficiency with the break-up probability z is plotted for each respective Ps energy. As can be seen from 4.13 b) and c), the Ps detection efficiencies for 22 and 33eV Ps atoms do not vary, within errors, across the range of z. For 13eV Ps, the detection efficiency doubles from 100% break-up to 100% elastic scattering, due to the large elastic scattering probability at this energy.

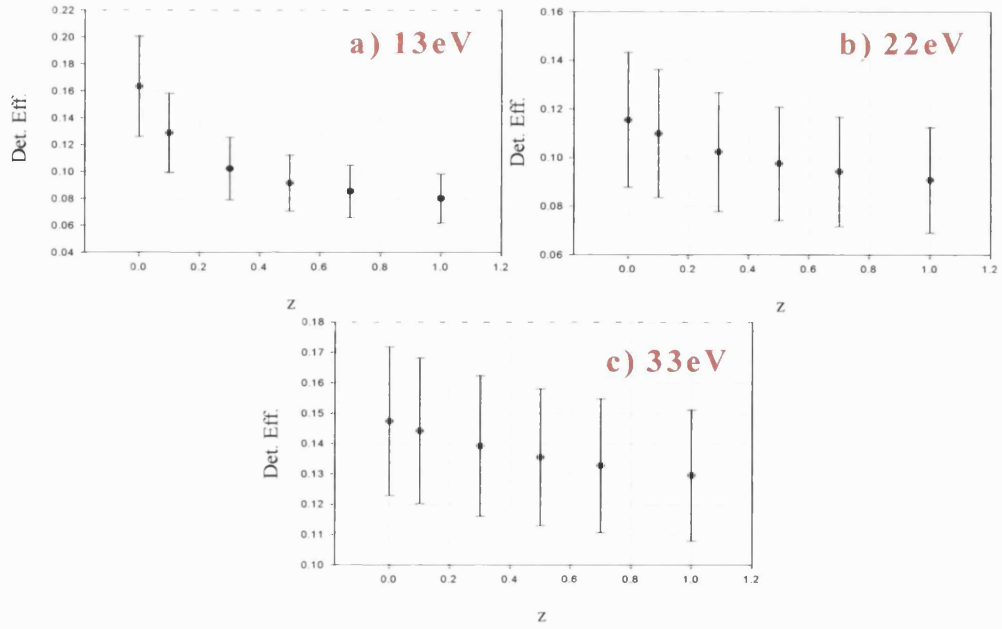

Figure 4.13 Variation of corrected Ps detection efficiency with break-up probability z.

4.6 Comparison of the Corrected Ps Detection Efficiency to the Equivelocity Positron Detection Efficiencies

In figure 4.14, the corrected Ps detection efficiency values are compared with the results obtained with the equivelocity positron method (see section 4.4). The energy of the equivelocity positrons have been doubled for comparison.

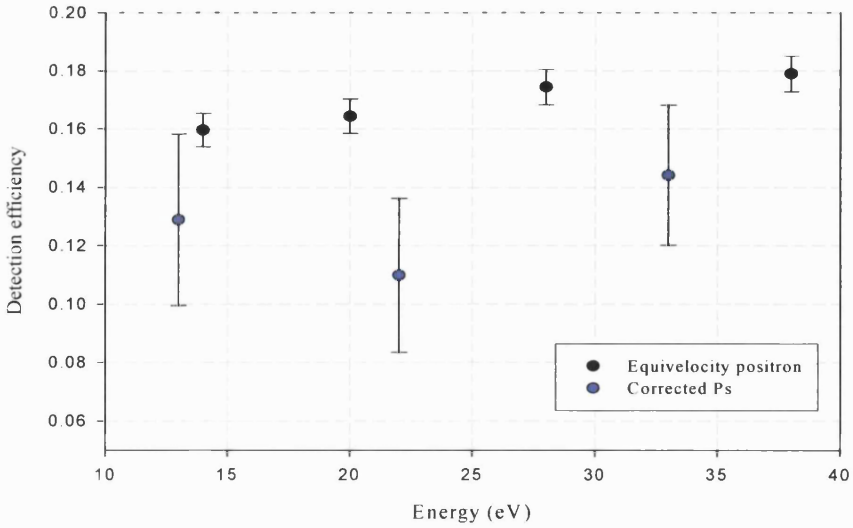

Figure 4.14 Comparison of the equivelocity positron detection efficiencies to the corrected Ps.

As can be seen, the equivelocity positron detection efficiency values are approximately 25% higher than the corrected values obtained for Ps. However, the analysis used to determine the equivelocity positron detection efficiency has not taken into account the possibility of elastic scattering of positrons from the surface of the channel plates. A correction may also need to be applied due to the formation of Ps from the reflected positron beam. Any Ps formation will give rise to extra counts on the CsI rate, which will reduce the measured detection efficiencies accordingly.

The incident positron flux may be written as,

$$N_i = N_P + N_{Ps} + N_e, \tag{4.29}$$

where N_e and N_{Ps} are the number of elastically scattered positrons and formed Ps atoms respectively. If α is the probability of positrons annihilating at the channel plates, N_P can be expressed as

$$N_P = \alpha N_i, \tag{4.30}$$

The number of Ps atoms formed by the backscattered positron beam can also be expressed as:

$$N_{Ps} = F_{Ps} N_i. \tag{4.31}$$

Here F_{Ps} is the Ps formation fraction with respect to the incident positron beam (Howell *et al*, 1986). The number of elastically scattered positrons may then be written in terms of the incident positron beam as

$$N_e = F_e N_i, \tag{4.32}$$

where F_e is the elastic scattering coefficient and is given by

$$F_e = 1 - \alpha - F_{Ps}, \tag{4.33}$$

Annihilations may now be resolved into, (a) those emanating from positrons at the channel plates, (b) those from Ps formed by the backscattered positrons, either through inflight decay or annihilating on the grids and (c) from the elastically scattered positron beam annihilating on the grids. The CsI detector may measure all these annihilations with an effective efficiency given by the place of annihilation and the respective CsI shielding profile. Therefore, the total number of CsI counts, γ_{total}, detected when measuring the positron detection efficiencies may be written as:

$$\gamma_{total} = \alpha\varepsilon_4' N_i + \varepsilon_{Grids}' N_i + F_{Ps}\left(\varepsilon_{inflight} + \varepsilon_{Grids}\right)N_i + \varepsilon_{Grids} F_e N_i + \gamma_{amb} + \gamma_{Pos} \qquad (4.34)$$

where the primed symbol refers to the incident positron beam. The counts recorded by the CsI detector which can give rise to a coincidence are

$$\left(\Delta N_{CsI}\right)_C = \alpha\varepsilon_4' N_i + \left(\varepsilon_2' + \varepsilon_3'\right)N_i + F_{Ps}\left(\varepsilon_{inflight} + \varepsilon_{Grids}\right)N_i + F_e\left(\varepsilon_{Grids}\right)N_i \qquad (4.35)$$

Given that the energy of the incident positrons is below 100eV, the inflight annihilation of the Ps atoms was determined assuming that the reflected positrons formed 10eV Ps (Howell *et* al, 1986). By comparison with Equation 4.34 we can rewrite Equation 4.35 as

$$\left(\Delta N_{CsI}\right)_C = \gamma_{total} - \gamma_{amb} - \gamma_{Pos} - \varepsilon_{R1}' N_i . \qquad (4.36)$$

Equations 4.35 and 4.36 may now be used to find the incident positron beam,

$$N_i = \frac{\gamma_{total} - \gamma_{amb} - \gamma_{Pos}}{\left(\alpha\varepsilon_4' + \varepsilon_{Grids}' + \left(\varepsilon_{inflight} + \varepsilon_1\right) + F_{Ps}\left(\varepsilon_{inflight} + \varepsilon_{Grids}\right) + F_e\left(\varepsilon_{Grids}\right)\right)}. \qquad (4.37)$$

This may be substituted back into Equation 4.36 in order to calculate the number of annihilations measured by the CsI detector, which may give rise to a coincidence. The modified CsI rate is then used in Equation 4.7 to give the measured detection efficiency.

Unlike in the Ps case, when detecting positrons the grid R1 is grounded and any positron, which elastically scatters from the surface of the channel plates and does not annihilate on one of the three grids infront of CEMA2, will be lost to the CsI

detector leading to an underestimate of the incident positron beam. The true positron detection efficiency may then be obtained by scaling the measured value with the fraction of positrons reflected away from the CsI detector, i.e.

$$\varepsilon_{e^+}^{True} = \varepsilon_{e^+}^{Measured}\left(1 - P_{lost}\right), \tag{4.38}$$

where P_{lost} is the fraction of positrons lost to the CsI detector. As a fraction of the elastically scattered positrons will annihilate at the grids infront of CEMA2, P_{lost} is given by

$$P_{lost} = 0.73F_e. \tag{4.39}$$

where 0.73 accounts for the beam attenuation through the grids and F_e is given by Equation 4.33.

Knights and Coleman (1996) have determined the fraction of epithermal positrons from SiO_2/Si to be ~0.30, decreasing to ~0.17 for Sn. From measurements of the branching ratio for positrons at a Cu (110) surface, Baker *et al* (1988) have determined a re-emitted positron fraction, F_e, in the energy range 0-40eV of 0.18 to 0.35. Baker *et al* also observed a decrease in the Ps formation fraction, F_{Ps}, in this energy range of 0.33 to 0.25. Assuming that the total branching ratio for all other channels is negligible, the fraction of positrons annihilating at the surface is given by $1\text{-}F_{Ps}\text{-}F_{+}$, i.e. 0.47-0.40. By employing a one-dimensional Boltzmann equation, Kong and Lynn (1990) have determined the fraction of positrons, re-emitted as positrons or Ps as 0.40. Howell *et al* (1986) have measured the Ps produced through reflected positrons from Ni, below 100eV incident energy, to be 0.20. Table 4.3 shows a summary of the re-emitted positron fraction and Ps formation fractions determined from solid-state studies. Also shown in table 4.3 are the elastic scattering and Ps formation fractions for high energy positrons, i.e. E=250eV, used to correct the high energy positron detection efficiency value determined in section 4.4.

	Energy (eV)	F_e	F_{Ps}	F_e+F_{Ps}
Low Energy				
Howell *et al* (1986)	<100		0.20	
Knights and Coleman (1996)	<100	0.17-0.3		
Baker *et al* (1988)	0-40	0.18-0.35	0.35-0.25	
Kong and Lynn (1990)	<100			0.40
High Energy				
Knights and Coleman (1996)	200-300	0.07-0.20		
Howell *et al* (1986)	250		0.14-0.15	

Table 4.3 Summary of re-emitted positron fraction and Ps formation fractions.

The limits for F_e and F_{Ps} in table 4.3 are given by the different materials investigated and the variance across the energy range shown.

Figure 4.15 shows the ratio of the elastic to total cross-sections for a number of atomic targets, as calculated by Baluja and Jain (1992). As can be seen from the plot, the value for the positron re-emission fractions, determined from solid-state surface studies, are more consistent with the higher elastic scattering fraction of positrons from atomic targets.

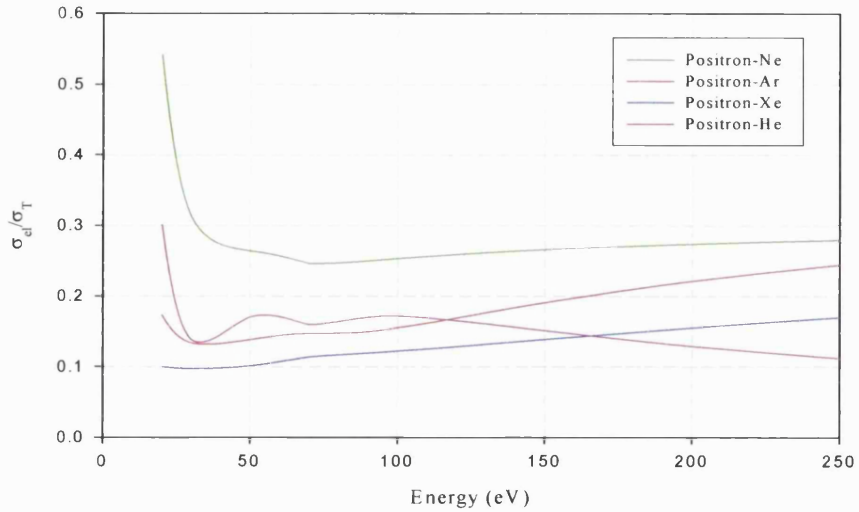

Figure 4.15 Ratio of elastic to total cross-sections for positron-Atom scattering, as calculated by Baluja and Jain (1992).

In figure 4.16, the equivelocity and corrected (F_e=0.20 and F_{Ps}=0.20) positron detection efficiencies are compared with the raw and corrected Ps detection efficiency values. As can be seen from figure 4.16, the corrected positron detection efficiencies are 17% lower than the equivelocity positron values. A much better agreement is seen between the two methods used to determine the Ps detection efficiency, after correction for elastic scattering, Ps formation and Ps break-up from the surface of the channel plates. The good agreement between the corrected positrons and the corrected Ps detection efficiencies suggests that at least for these two projectiles, the dominant

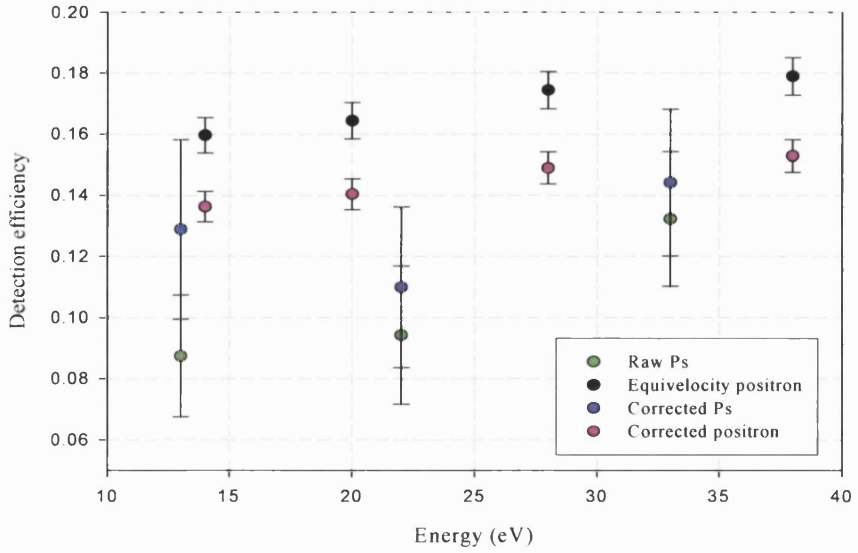

Figure 4.16 Comparison of the corrected positron detection efficiencies to the measured positron and the measured and corrected Ps efficiencies.

factor in determining the detection efficiency is their impact velocity.

In order to determine the uncertainty associated with the corrected positron detection efficiencies, the values of F_e and F_{Ps} have been varied within the ranges given in table 4.3 and the results are plotted in figure 4.17.

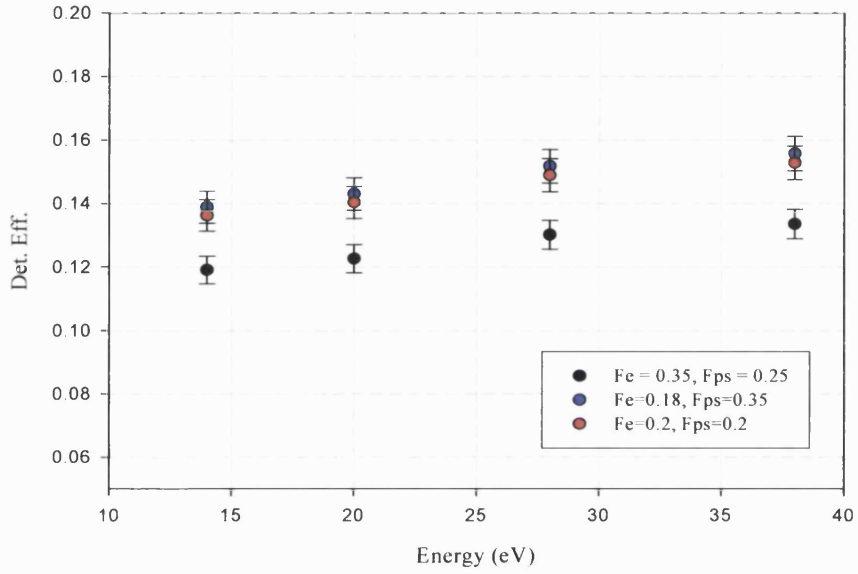

Figure 4.17 Variation of the corrected positron detection efficiencies with elastic scattering and Ps formation probability.

As can be seen in figure 4.17, the correction to the equivelocity detection efficiency values are dominated by Equation 4.38, whereby the fraction of the incident beam lost to elastic scattering is corrected for. Therefore, the lowest value for the detection efficiencies corresponds to the largest elastic scattering fraction. With F_e=0.18 an increase of 2% is observed, whilst for F_e=0.35, the detection efficiencies are reduced by 17%, as expected from Equation 4.38.

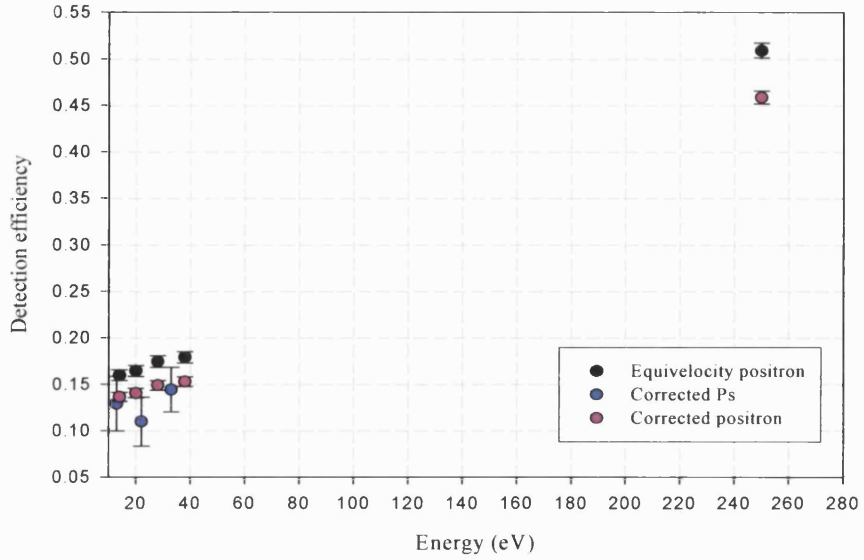

Figure 4.18 Comparison of the corrected positron detection efficiencies, compared with the equivelocity positron and corrected Ps.

In figure 4.18 the corrected Ps detection efficiencies are shown along with the equivelocity positron and the corrected positron detection efficiencies. Also included in the plot is the high-energy (~250eV) positron value, determined in section 4.4 as 0.51±0.01, also corrected for elastic scattering and Ps formation using the average of the 250eV positron values for F_e and F_{Ps} given in table 4.3, to give a value of 0.46±0.01.

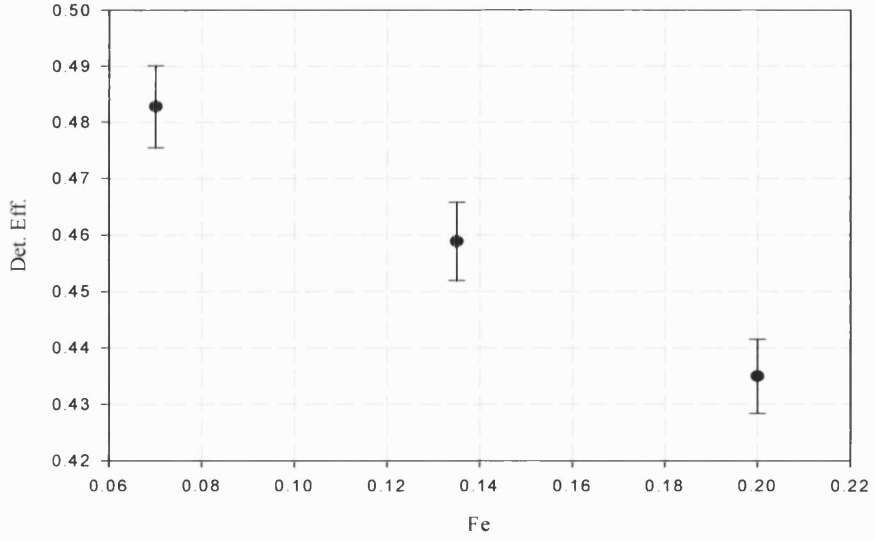

Figure 4.19 Variation of the 250eV positron detection efficiency with elastic scattering fraction.

Figure 4.19 shows the variation in the 250eV positron detection efficiency with the elastic scattering fraction. As can be seen from the plot, the detection efficiency value varies by $\pm$5% as F_e is varied from 0.07 to 0.20.

Both the corrected Ps and corrected positron detection efficiencies will be used in chapter 5 to determine absolute break-up cross-sections and a discussion on the effects of varying the fraction of elastic scattering, Ps formation and Ps break-up on the absolute break-up cross-section will be included.

Chapter 5

Positronium Break-Up in Collision with He Atoms

5.1 Introduction

In this chapter, the first ever measurements of the Ps break-up cross-section from He atoms are presented. A description of the experimental procedures employed to obtain them and of the investigation and determination of systematic effects are also included. The results are compared with available theoretical calculations.

As the break-up study was undertaken using the time-of-flight detection system, longitudinal energy spreads for the break-up positrons have also been determined. The distributions are found to be peaked at around 50% of the residual energy, suggesting a strong correlation between the residual particles.

5.2 The Absolute Ps-He Break-Up-Cross-Section

The absolute break-up-cross-section, at a given energy is given by

$$\sigma_{bu} = \frac{N_+}{(N_{Ps})_{scatt}} \times \sigma_T \times \left(\frac{\varepsilon_{Ps}}{\varepsilon_+} \right) \times S \times G \qquad (5.1)$$

where N_+ = Net number of positrons released from Ps break-up

$(N_{Ps})_{scatt}$ = Net number of scattered Ps atoms

σ_T = The corresponding Ps-He total cross-section

$(\varepsilon_{Ps}/\varepsilon_+)$ = Ratio of the efficiencies for detection of Ps/e^+

S = Survival probability of Ps atoms

G = A correction factor dependent upon the geometry of the apparatus

All the factors used to determine the absolute break-up-cross-section will be described and evaluated in the following sections.

5.2.1 Experimental Method

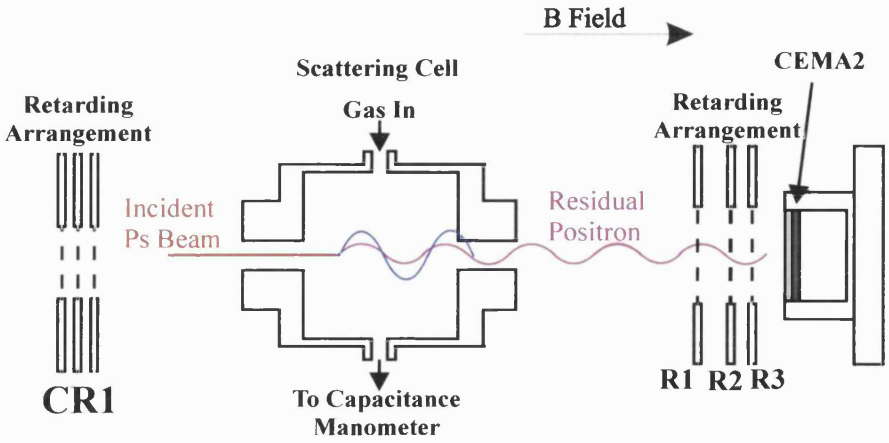

Figure 5.1 Schematic diagram of the Ps scattering and detection region.

Positrons released from Ps break-up are confined to spiral trajectories in the guiding magnetic field with a Larmor radius given by their kinetic energy and emittance angle, see figure 5.1. If the Larmor radius is smaller than the exit aperture of the scattering cell (pink curve, fig 5.1), the positron can exit and travel to the detector. Grounding the retarder R1 allows these positrons to be detected together with the transmitted Ps beam. The flux of the positrons originating from Ps break-up is obtained by taking two measurements: with R1 positive, only Ps (N_{Ps}) is counted; with R1 grounded, both positrons and Ps ($N_{e^+,Ps}$) are detected. Subtraction of the two spectra yields the number of positrons from collisional break-up of Ps, i.e.

$$N_+ = N_{e^+,Ps} - N_{Ps}. \tag{5.2}$$

The number of Ps atoms scattered out of the beam through any interaction with the target gas and is given by

$$(N_{Ps})_{scatt} = I_0 - I, \tag{5.3}$$

where I_0 is the incident Ps beam (measured with vacuum in the scattering cell) and I is the transmitted Ps beam (measured with He in the scattering cell).

The positron beam intensity was measured for 20s at the beginning and end of

each run in order to monitor its stability. During these measurements, the positron beam remained stable, within experimental errors (see table 5.1). The numbers of incident Ps, transmitted Ps and residual positrons were measured sequentially. Typically, the incident and attenuated Ps beams were measured for 18000s and 50000s respectively. The residual positron measurements were taken for 18000s. The random background contribution to the Ps peak was taken from the flat part of the same time-of-flight spectrum and subtracted directly. The number of counts, in the regions of interest from each spectrum, corresponding to incident Ps, transmitted Ps and residual positrons were then determined. Figure 5.2 shows typical time-of-flight spectra for the transmitted Ps beam, residual positrons (with transmitted Ps) and net residual positrons (break-up minus transmitted Ps).

Quantity	***Error***
Positron beam intensity (e^+)	$\pm 2\%$
Positronium beam intensity (I & I_0)	$\pm 10\%$
Residual positrons and Ps beam ($N_{e^+,Ps}$)	$\pm 5\%$
Target gas pressure (P)	$\pm 2\%$

Table 5.1 Typical errors on quantities measured to determine σ_{bu}.

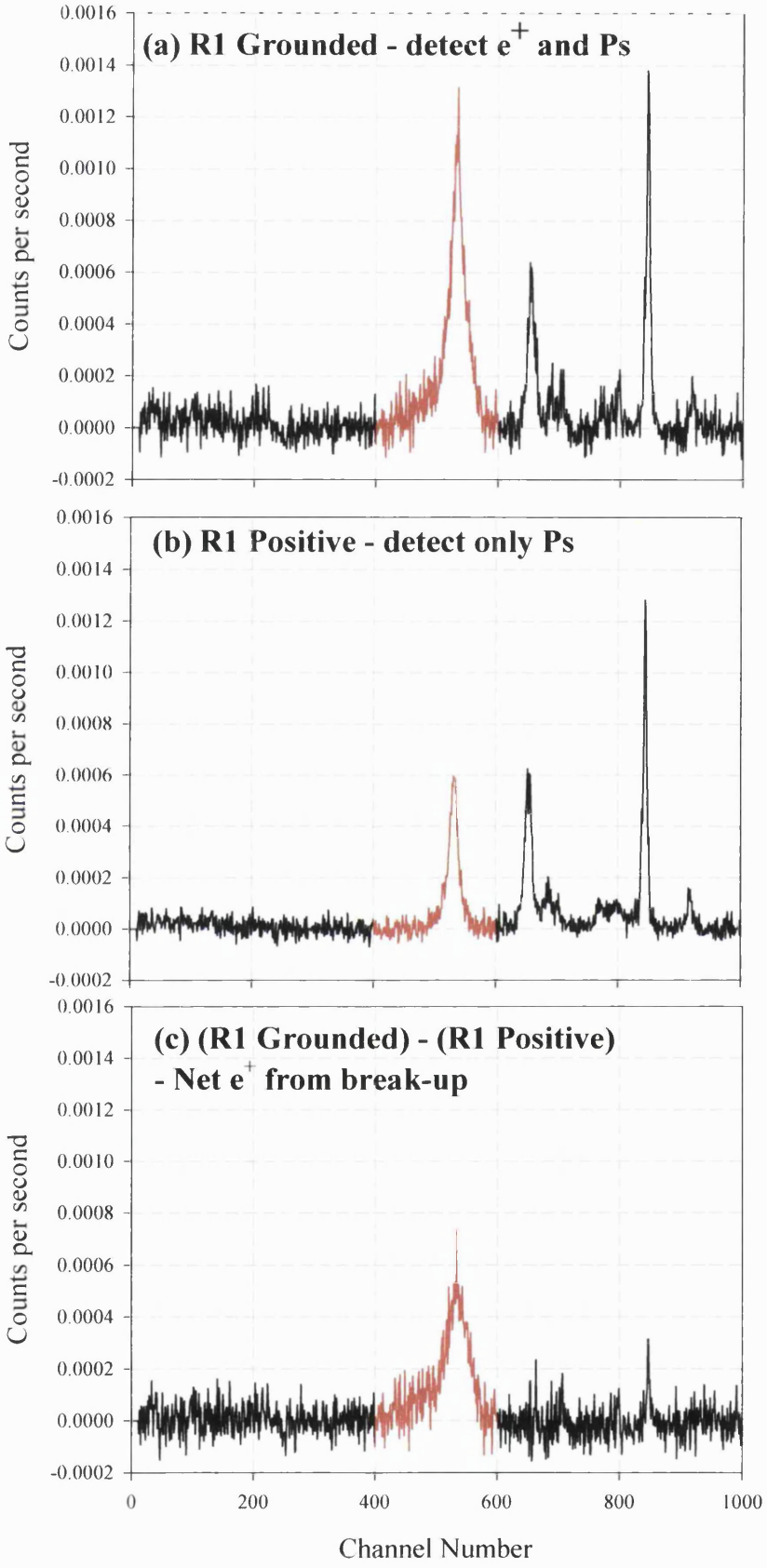

Figure 5.2 Typical time-of-flight spectra for (a) residual positron and Ps, (b) transmitted Ps and (c) net residual positrons.

5.2.2 Magnetic Field Measurements

In order to ensure that all positrons from Ps break-up were extracted from the scattering cell, the magnitude of the magnetic field, **B,** in the scattering region was adjusted such that the Larmor radius of the residual positrons plus the radius of the Ps beam was smaller than the radius of the exit aperture of the scattering cell. This was checked by verifying signal saturation with increasing values of **B**. Figure 5.3 shows results obtained for different **B**-field intensities around the scattering cell for the break-up positron yield, Y_{e^+}, defined as

$$Y_{e^+} = \frac{N_+}{(N_{Ps})_{scatt}} \tag{5.4}$$

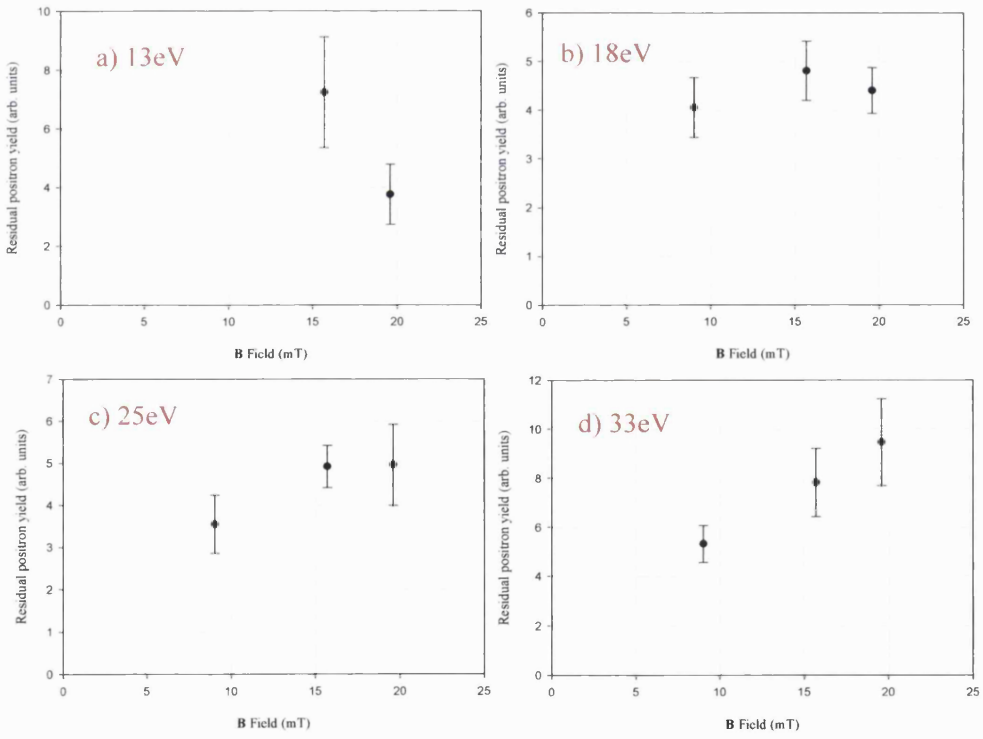

Figure 5.3 Residual positron yields for differing B-field intensities for the four incident Ps energies a) 13eV, b) 18eV, c) 25eV and d) 33eV.

At the two higher incident energies, the relative break-up-cross-section appears to saturate within errors with increasing magnetic field, indicating insufficient confinement of the residual positrons at the lower magnetic fields. At 25eV and 33eV,

the break-up-cross-section was obtained from the weighted mean of the values above 15mT. At 18eV, the residual positron yield does not display a significant **B**-field dependence, indicating that the lower **B**-field values are sufficient to confine the residual positrons. This would also appear to be the case at 13eV, although the experimental uncertainties are larger. For both lower energies, the relative break-up-cross-section was obtained from the weighted average of all the **B**-field measurements.

Measurements were also taken at various He gas pressures (shown in appendix C), to check the linearity of signal with pressure. Within the pressure range of this study, no attenuation of the break-up flux was found to be occurring in the target gas. Figure 5.4 shows the residual positron yield values obtained in this study.

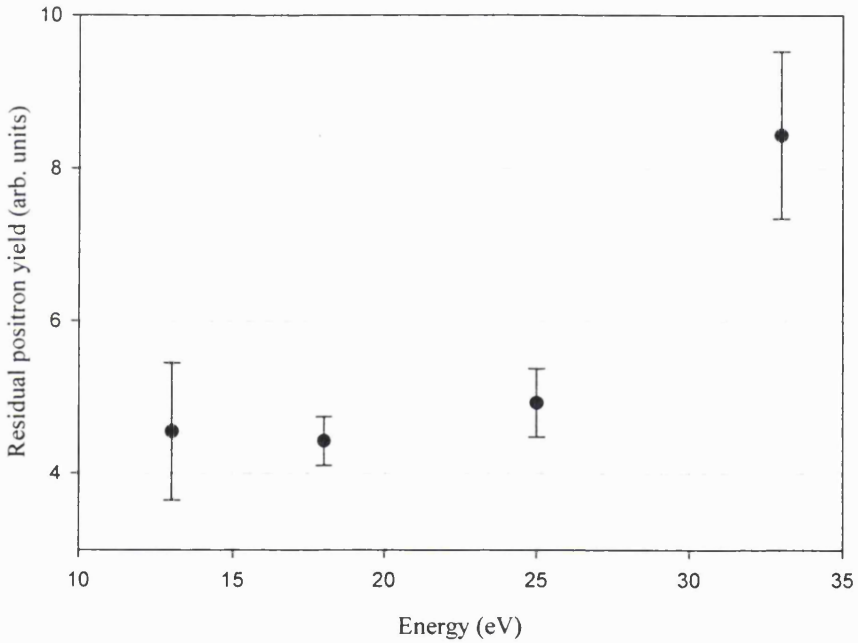

Figure 5.4 Residual positron yields versus incident Ps energy.

As can be seen from figure 5.4, the residual positron yield is approximately constant at the lower energies, but almost doubles at 33eV. In the next few sections the correction factors (given in Equation 5.1) are calculated and are used to determine the absolute break-up cross-section.

5.2.3 Survival Probability of Ps Atoms

In order to determine the absolute values of the break-up-cross-section, we need to know the number of Ps atoms traversing the scattering cell. More Ps atoms are available to break-up within the scattering cell than are detected at CEMA2, due to in-flight-decay. To correct for this effect, we have to scale the measured scattered Ps flux, $(N_{Ps})_{scatt}$, by calculating the average fraction of the incident Ps beam passing through the scattering cell. The total number of Ps atoms, N_{av}, available to break-up in the scattering cell is given by

$$N_{av} = \frac{(N_{Ps})_{scatt}}{S}, \tag{5.5}$$

where S is the survival probability factor and is given by

$$S = \frac{S(CEMA2)}{\langle S(ScattCell)\rangle}, \tag{5.6}$$

and *S(CEMA2)* corresponds to the fraction of Ps atoms that reach the detector – taken directly from the corresponding Ps decay curve (see section 4.5.3). <*S(ScattCell)*> is the average fraction of Ps atoms along the scattering cell, calculated using

$$\langle S(ScattCell)\rangle = \frac{1}{(l_2 - l_1)} \int_{l1}^{l2} e^{\frac{-1}{\tau}\left(\frac{m}{E}\right)^{\frac{1}{2}} x} dx, \tag{5.7}$$

where x corresponds to the Ps flight length, τ is the o-Ps lifetime, E is the Ps kinetic energy and m is the mass of a positron. The limits for the Ps flight length, through the scattering cell, are l_1= 0.073m and l_2= 0.139m. These distances correspond to the flight-length from the middle of the production cell to the middle of the scattering cell, plus or minus half of the scattering cell length (see section 3.3.3). Table 5.2 shows the survival probability factors determined for each Ps energy used in this study.

Energy (eV)	*Flight Length (cm)*	*S(CEMA2)*	*<S(ScattCell)>*	*S*
33	0.393	0.314	0.690	0.455
27	0.393	0.267	0.661	0.404
18	0.293	0.314	0.620	0.506
13	0.293	0.249	0.571	0.436

Table 5.2 Ps survival probability correction factors.

5.2.4 Geometric Ps Factor

The Ps break-up study was undertaken mostly using a scattering cell with cylindrical apertures of radius 4mm. The Ps detection pencil angle, θ_{pencil} (light purple region of figure 5.6) is defined by the exit aperture of the scattering cell. Only Ps atoms within this pencil angle will be detected at CEMA2. Ps atoms can enter the scattering cell outside of the Ps detection pencil angle (cyan region inside the scattering cell). As the residual positrons are magnetically confined, any Ps atoms that break-up in the cyan region of figure 5.5 can lead to positrons that are confined to reach CEMA2, leading to a greater break-up signal than that from the possible break-up of the detectable Ps.

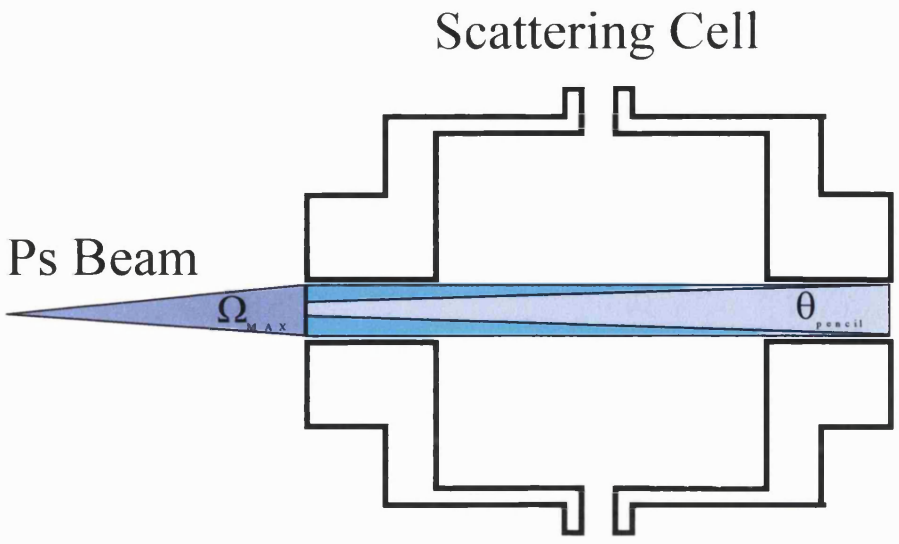

Figure 5.5 Schematic of scattering cell showing Ps pencil angle, θ_{pencil} (light purple) and maximum Ps solid angle Ω_{max}.

To correct for this geometric effect, the ratio of the maximum solid angle, defined by the entrance aperture of the scattering cell and the average Ps solid angle through the cell is calculated. The maximum Ps solid angle, Ω_{max}, is given by

$$\Omega_{max} = \frac{\pi \times r^2}{D^2} = 9.8 \times 10^{-3} sr, \tag{5.8}$$

where r = radius of scattering cell aperture (4mm)

D = distance from middle of production cell to entrance aperture of scattering cell (7.15mm)

The average Ps solid angle is determined by integrating over the scattering cell length, i.e.

$$\begin{aligned} \langle \Omega_{Ps} \rangle &= \frac{\pi r^2}{(l_2 - l_1)} \int_{l1}^{l2} \frac{1}{y^2} dy \\ &= 4.95 \times 10^{-3} sr \end{aligned} \tag{5.9}$$

The geometric factor, G, is then given by

$$G = \langle \Omega_{Ps} \rangle / \Omega_{+} = 0.51. \tag{5.10}$$

5.2.5 Results

Figure 5.6 shows the absolute break-up-cross-section values determined using Equation 5.1. The values for G and S are taken from Equation 5.10 and Table 5.2 respectively. The total cross-section values used have been presented in section 3.3.4. The positron detection efficiency, ε_{+}, used to determine the absolute break-up cross-section values presented were determined in section 4.6 as 0.46 ± 0.01, after correction for elastic scattering from the channel plates. The values for ε_{Ps} used here are the corrected equivelocity positron detection efficiencies shown in figure 4.16. A discussion on the effects the detection efficiency values have on the absolute break-up cross-section is given in section 5.3.

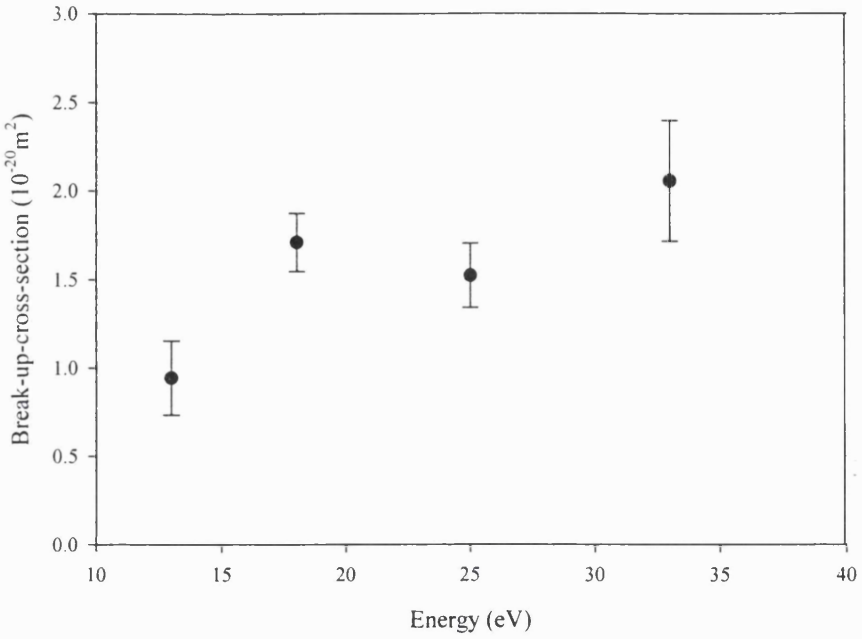

Figure 5.6 Absolute Ps-He break-up-cross-section values determined in this study.

5.2.6 New Gas Cell

To test the correction applied through the geometric factor, a new scattering cell (shown schematically in figure 5.7) was designed such that $G = 1$. With this new scattering cell, the entrance aperture defines the Ps pencil angle, in this way all the Ps entering the scattering cell is detectable at CEMA2. The scattering cell was designed such that break-up positrons of up to 100eV and emittance angle of 90^0, would not be intercepted by the exit aperture.

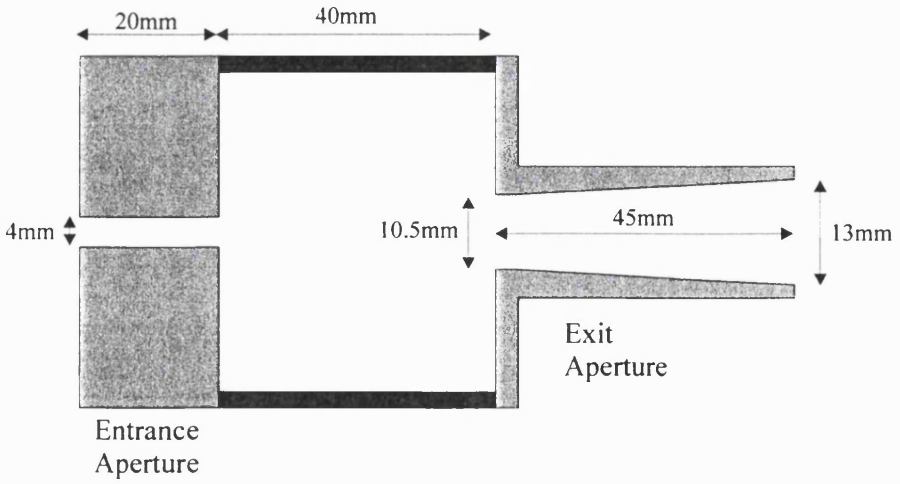

Figure 5.7 Schematic of the new scattering cell.

Table 5.3 shows the survival probability values for the new scattering cell (calculated as per section 5.2.4, but with l_1=0.097m and l_2=0.157m). Measurements for the determination of σ_{bu} were taken with the new gas cell, as described in section 5.2.

Energy (eV)	***Flight Length (cm)***	***S(CEMA2)***	***<S(ScattCell)>***	***S***
33	36.3	0.343	0.690	0.498
18	36.3	0.238	0.608	0.391

Table 5.3 Ps survival probability correction factors for new gas cell.

Figure 5.8 shows the absolute Ps-He break-up-cross-section values determined with the new scattering cell (calculated using equation 5.1 with G=1), compared to those obtained with the old scattering cell. As can be seen from figure 5.8, the break-up-cross-section values determined for both gas cells are in agreement within errors, indicating that the geometric effect for the old scattering cell has been evaluated correctly.

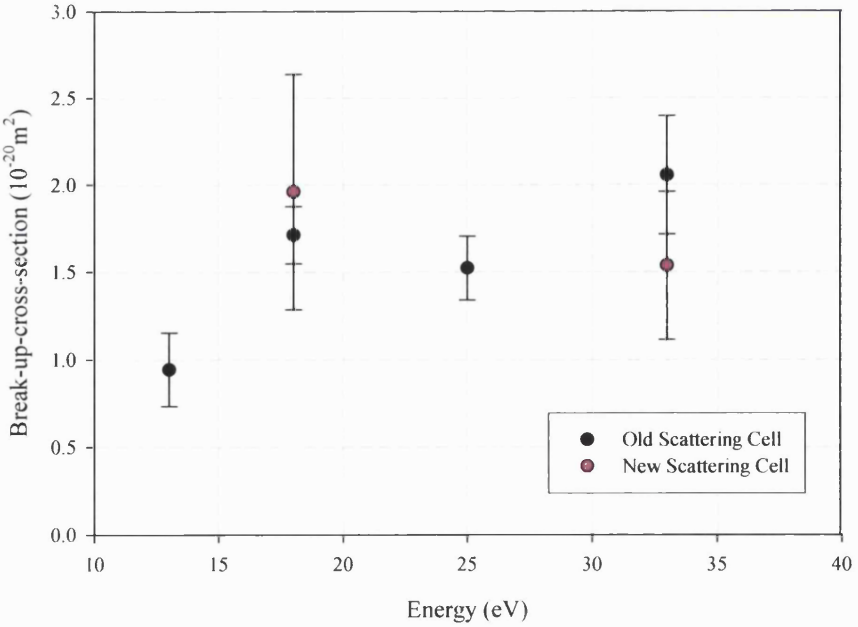

Figure 5.8 Comparison of absolute Ps-He break-up-cross-section determined with the two scattering cells.

Table 5.4 summarises the experimental quantities determined for the new scattering cell, compared with the values determined for the old scattering cell. The apertures to the new scattering cell were designed such that the conductance would be the same as for the old scattering cell. In this way, the same pressure range could be achieved in the new scattering cell. The effective cell length for the new scattering cell was determined as described in section 3.3.3. As can be seen from table 5.4, the effective cell lengths determined for the two cells are very close to each other as expected.

	New Scattering Cell	***Old Scattering Cell***
Effective Cell length (cm)	6±1	7±1
Total-cross-section @ 18eV ($10^{-20}m^2$)	4.4±0.5	5.0±0.3
Total-cross-section @ 33eV ($10^{-20}m^2$)	3.9±0.3	3.4±0.2

Table 5.4 Comparison of measurements performed with the new and old scattering cells.

5.3 Discussion on the Uncertainties on the Determination of the Absolute Scale of the Ps-He Break-up Cross Section

As discussed in section 1.6, absolute experimental Ps-He break-up cross-sections have long been desired in the hope that they might aid in separating the different theoretical models for Ps-He scattering. In order to compare our experimental absolute break-up cross-sections with theory, a measure of the uncertainty in the determination of $\varepsilon_{Ps}/\varepsilon_{+}$ is required. Given the range of values for the re-emitted positron fraction and Ps formation fractions used in correcting the equivelocity positron detection efficiencies in section 4.6, a maximum and minimum and average value for $\varepsilon_{Ps}/\varepsilon_{+}$ may be calculated. A value for $\varepsilon_{Ps}/\varepsilon_{+}$ may also be calculated using both the raw and corrected Ps detection efficiencies determined in chapter 4. Table 5.5 shows the values of F_e and F_{Ps} used in each case for determining ε_{Ps} and ε_{+}, and hence of $\varepsilon_{Ps}/\varepsilon_{+}$.

	$(\varepsilon_{Ps}/\varepsilon_{+})_{RawPs}$	$(\varepsilon_{Ps}/\varepsilon_{+})_{CorrPs}$	$(\varepsilon_{Ps}/\varepsilon_{+})_{Av}$	$(\varepsilon_{Ps}/\varepsilon_{+})_{Max}$	$(\varepsilon_{Ps}/\varepsilon_{+})_{Min}$
ε_{+}	250eV positron, $F_e = 0.135$, $F_{Ps} = 0.145$.	250eV positron, $F_e = 0.135$, $F_{Ps} = 0.145$.	250eV positron, $F_e = 0.135$, $F_{Ps} = 0.145$.	250eV positron, $F_e = 0.2$, $F_{Ps} = 0.14$.	250eV positron, $F_e = 0.07$, $F_{Ps} = 0.15$.
ε_{Ps}	Raw Ps.	Corrected Ps.	Equivelocity positron, $F_e = 0.20$, $F_{Ps} = 0.20$.	Equivelocity positron, $F_e = 0.18$, $F_{Ps} = 0.35$.	Equivelocity positron, $F_e = 0.35$, $F_{Ps} = 0.25$.

Table 5.5 Values of F_e ad F_{Ps} used in the various determinations of the detection efficiency ratio.

Figure 5.9 shows a comparison of the absolute break-up cross-sections obtained using the average positron, the raw and the corrected Ps detection efficiencies. The corrected Ps detection efficiency has been taken as the weighted mean of the corresponding values given in section 4.5.7 as (13±2)%. The absolute break-up cross-sections presented here are a weighted mean of the values obtained with the two scattering cells.

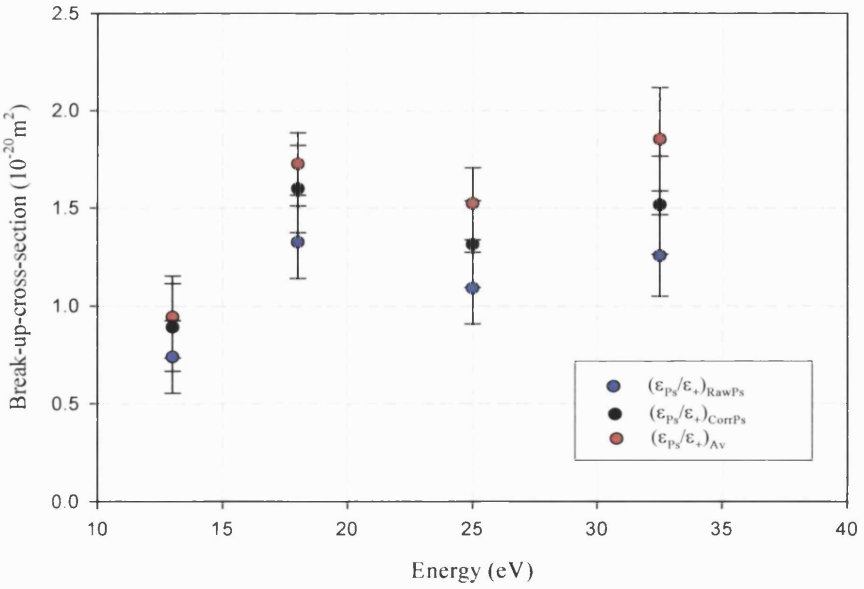

Figure 5.9 The Absolute break-up cross-sections determined using the detection efficiencies as in table 5.5.

As can be seen in figure 5.9, the absolute break-up cross-section values obtained using the detection efficiencies determined using the average positrons and corrected Ps agree within errors, although those determined with the corrected Ps detection efficiency are between 6% to 20% lower than those for equivelocity positrons. The absolute break-up cross-sections obtained with the raw Ps detection efficiency are between 20-30% lower than those obtained with the average positron detection efficiency values. As the raw Ps detection efficiencies do not contain any elastic scattering corrections they are a lower limit to the absolute magnitude of the break-up cross-section.

Figure 5.10 shows a comparison of the absolute break-up cross-sections obtained using the maximum and minimum values of $\varepsilon_{Ps}/\varepsilon_{+}$ determined using equivelocity positrons, see table 5.5.

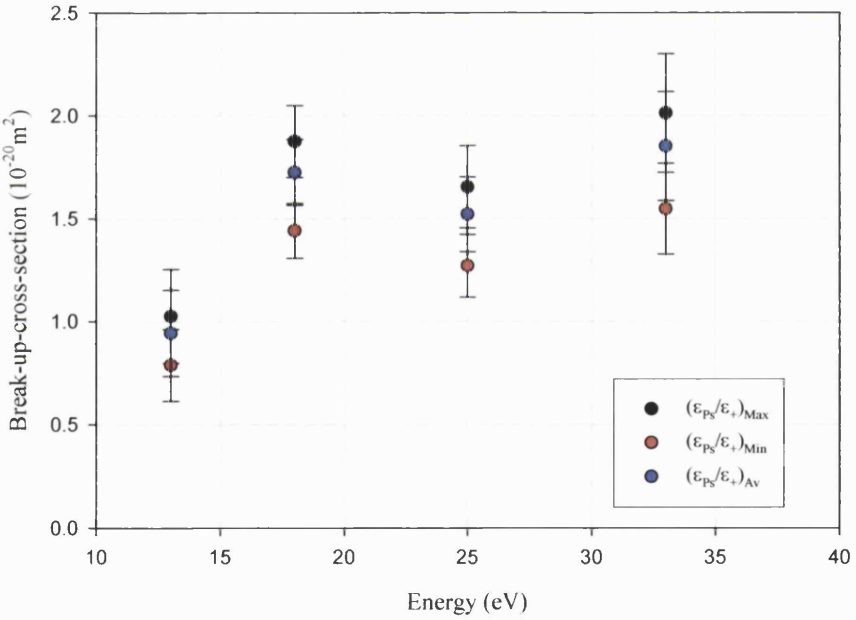

Figure 5.10 Variation of the break-up cross-section with the range of corrected positron detection efficiencies.

As shown in figure 5.10, the maximum and minimum absolute break-up cross-sections are (+8/-10)% of those obtained with the average positron detection efficiencies.

Given the two technique used to determine the Ps detection efficiency, the uncertainty in the break-up cross-section due to the estimates of the elastic scattering

fraction, Ps formation fraction and Ps break-up fraction is given by +8% (maximum equivelocity positron) to –(20-30)% (raw Ps).

5.4 Comparison with Theory

Figure 5.11 shows a comparison between the break-up cross-section values determined in this study to theoretical calculations by Blackwood *et al* (1999) and Biswas and Adhikari (1999). The experimental break-up cross-section values, plotted in figure 5.11, were determined with the average positron detection efficiency values.

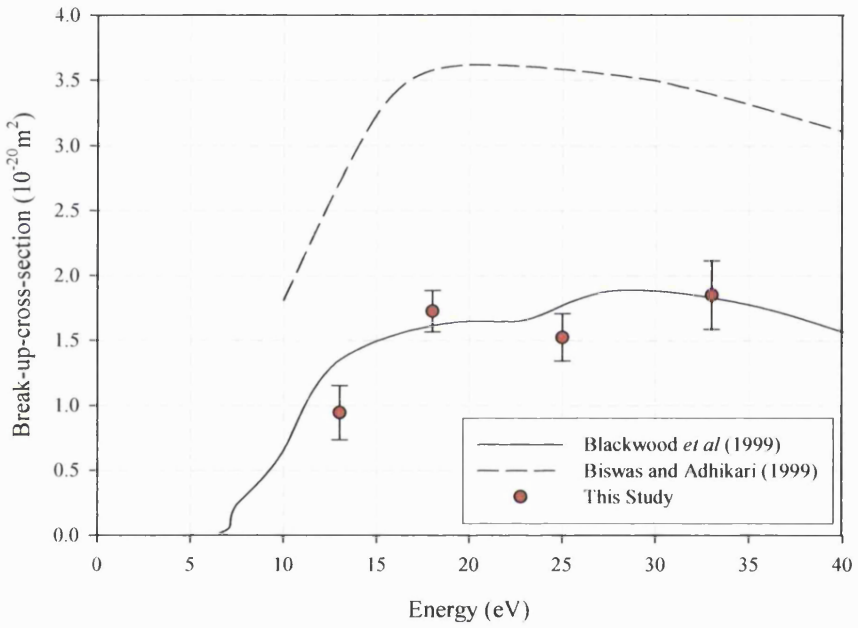

Figure 5.11 The Absolute break-up cross-sections determined in this work compared to available theories.

As can be seen in figure 5.11, the present absolute Ps-He break-up cross-section data are in good agreement with the coupled-state theory of Blackwood *et al* (1999). However, in the case of the total cross-section, a significant discrepancy exist with this theory, with Blackwood *et al* underestimating the beam total cross-section measurements above 10eV by up to 30% (see section 1.5.3). Although the predicted total-cross-sections of Biswas and Adhikari (1999) are in much better agreement with the beam measurements, the break-up cross-section overestimates the measurements made in this study by roughly a factor of two.

It is hoped that these new measurements will assist theories towards an improved understanding of the Ps-He collision system.

5.5 Residual Positron Longitudinal Energy Spreads

In this and the next sections, the method for converting the residual positron time spectra into longitudinal energy spreads is given. The residual positron longitudinal energy spreads are compared to the Ps energy spreads and systematic timing resolutions are calculated in order to understand the intrinsic energy spreads associated with these measurements.

Using the energy calibration technique, described in section 3.2.4, the analysis may be extended to calculate the longitudinal energy spreads of the residual positrons, E_{bu}, from the time-of-flight spectrum using

$$E_{bu} = \frac{1}{2} m \left(\frac{L_{bu}}{t_{bu}} \right)^2 , \tag{5.11}$$

where m is the mass of a positron, L_{bu} is the residual positron flight-length and t_{bu} corresponds to the residual positron flight-time, given by

$$t_{bu} = (t0 - chn_{bu}) \times t_{ch} - t_{e^-} + t_{e^+} - t_{cell} - t_{Ps} + t_{rets} , \tag{5.12}$$

where the symbols are as of Equations 3.7 and 3.8, chn_{bu} is the corresponding residual positron time-of-flight channel number, t_{Ps} is the time for Ps to reach the middle of the scattering cell and t_{rets} is the acceleration time through the retarding arrangement in front of CEMA2 for the residual positrons.

Figure 5.12 shows the longitudinal energy spreads for the residual positrons, determined from the time-of-flight spectra. Each distribution is the average of all the residual positron longitudinal energy spectra. The respective incident Ps energy is shown down the left hand side of the page and the magnetic field strength, at which the measurements were taken, across the top of the page. The maximum of each longitudinal energy distribution has been normalised to one for comparison of the distribution shapes.

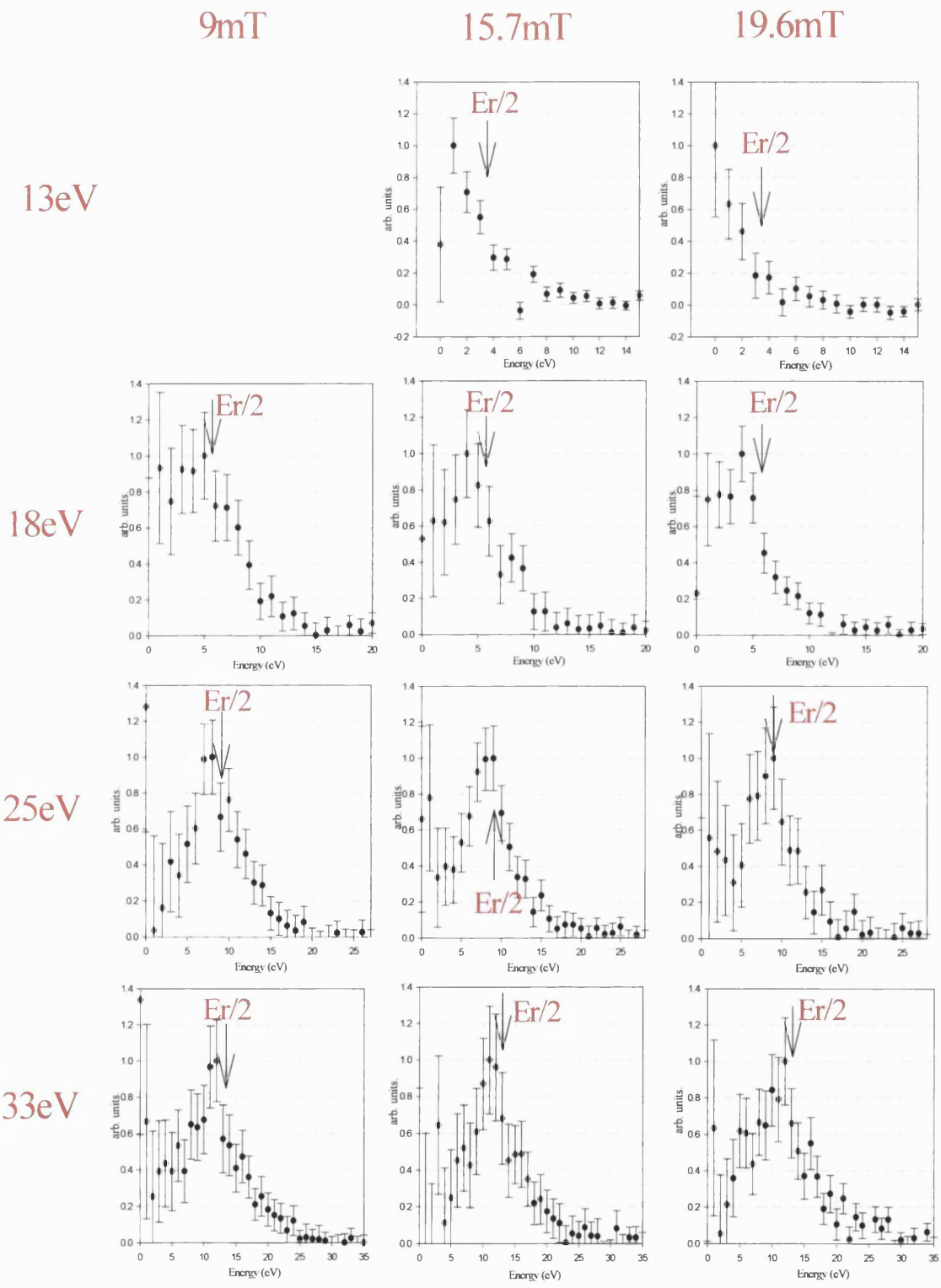

Figure 5.12 Longitudinal energy spreads of the residual positrons. The incident Ps energy is shown down the left hand side and the magnetic field through the scattering cell across the top of the page ($E_r/2 = (E_{Ps}-B)/2$).

Marked on each plot is half the residual energy E_r (where $E_r=E_{Ps}-B$, i.e. Ps kinetic energy minus half of its ground state binding energy (6.8eV)). As can be seen, the residual positron distributions are peaked just below half of the residual energy. A peak would be expected at this position if both the residual particles have $E_r/2$ and are emitted at a small angle with respect to the beam axis. The shape of the residual positron longitudinal energy distributions appear not to be significantly dependant on the **B**-field through the scattering region, suggesting that the residual particles are indeed emitted at small angles.

5.6 Timing Resolution of the Time-of-Flight System

In order to further our understanding of the longitudinal energy distributions of the remoderated positrons, Ps and residual positrons, a measure of the intrinsic time-of-flight timing resolution and systematic time spreads are required. The timing resolutions have been determined by approximating the respective positron and Ps time-of-flight peaks to Gaussian distributions, although in practice the time-of-flight peaks are asymmetric. The analysis presented in the next subsections has been performed on 33eV Ps and its corresponding residual positrons.

5.6.1 Intrinsic Time-of-Flight Timing Resolution

The intrinsic timing resolution of the time-of-flight system, ΔT_0, is a measure of the spread in times associated with a coincidence between the Tagger and CEMA2. A simple measure of the timing resolution can be taken directly from the time spread of the $t=0$ peak on the time of flight spectrum, see section 2.7.1. ΔT_0 is given by the time-of-flight $t=0$ peak full-width-half-maximum (FWHM), $T0_{FWHM}$, multiplied by t_{ch}, as determined in section 3.2.2. $T0_{FWHM}$, taken from a time-of-flight spectrum, is 4.4±0.4 channels. Therefore, ΔT_0, is given by

$$\Delta T_0 = 4.2\pm0.4 \text{ ns.} \qquad (5.17)$$

5.6.2 Positronium Formation Point

An extra time spread, ΔT_{form}, is associated with the range of positron/Ps flight lengths arising from the different Ps formation points along the production cell. This spread is given by the difference in times for a positron and a Ps atom to traverse the production cell, i.e,

$$\Delta T_{form} = \left(\frac{m}{2}\right)^{\frac{1}{2}} L_{Prod}\left(\left(\frac{1}{E_{e^+}}\right)^{\frac{1}{2}} - \left(\frac{2}{E_{Ps}}\right)^{\frac{1}{2}}\right) \approx 3\,\text{ns}, \tag{5.18}$$

where L_{Prod} is the length of the production cell (approximately 2cm, see section 2.6.2) and E_{e^+} and E_{Ps} are the incident positron and Ps energies respectively.

5.6.3 Positronium Break-Up Point

As Ps atoms can break-up anywhere along the length of the scattering cell, a similar calculation can be made for the time spread associated with the break-up point within the scattering cell, ΔT_{bu}. This spread is the time difference between a Ps atom and a residual positron to traverse the length of the scattering cell, i.e.

$$\Delta T_{bup} = \left(\frac{m}{2}\right)^{\frac{1}{2}} L_{Scatt}\left(\left(\frac{2}{E_{Ps}}\right)^{\frac{1}{2}} - \left(\frac{1}{E_{e^+}}\right)^{\frac{1}{2}}\right) = 3.7\,\text{ns}, \tag{5.23}$$

and L_{Scatt} is the effective length of the scattering cell E_{Ps} and E_{e^+} are the incident Ps and residual positron (taken as $E_r/2$, see section 5.5) energies respectively.

5.6.4 Discussion on the Ps and Residual Positron Energy Distributions

The FWHM of the incident Ps energy distributions was calculated in section 3.2.4 to be 6.0±0.2eV, double that of the remoderated positron FWHM value quoted in section 3.2.3. This is somewhat greater than would be expected from the time-spread associated with the Ps formation point and the intrinsic timing-resolution. If no

further systematic effect can account for the extra broadening and the shift in the peak energy (with respect to that expected from the lowest thresholds) then an additional inelastic effect might be occurring simultaneously to the formation of Ps. A recent investigation into three-body dynamics for single ionisation of H_2 by 50 and 100eV incident positrons by Fiol and Olsen (2002) has shown that the shift observed in the ejected-electron-energy-distribution (Kövér *et al,* 2001 see section 3.2.4) can be attributed to the recoil of the residual target ion. If target recoil effects are significant also in Ps formation in a bound state, then both a shift in the energy and a spread in the FWHM will be apparent. It should be noted that the energy distributions of the Ps beams obtained from He and Ar are comparable to those of H_2, suggesting that the width of the Ps energy spread obtained from H_2 is not due to molecular degrees of freedom.

As can be seen from figure 5.12, the FWHM for the residual positrons is comparable to that of the incident Ps beam. From a consideration of the timing resolutions inherent with these measurements, systematic effects alone would not account fully for the width of the longitudinal energy distributions. Hence, a non-negligible fraction of this spread would seem to arise from the intrinsic energy spread of the residual positrons themselves.

5.7 Summary

The results of Ps-He break-up cross sections, σ_{bu}, in a range of Ps energies (13 to 33eV) have been presented and found to be in good agreement with the theoretical calculation of Blackwood *et al* (1999).

A measure of the residual positron longitudinal energy distributions has also been obtained, which show a peak just below half the residual energy. This signifies the release of positrons from the break-up of Ps with half of the residual energy and at a small angle with respect to the incident beam axis. This indicates that a strong correlation exists between the positron and electron in the final state, in analogy with the electron-loss-to-the-continuum process in atom-atom collisions (Crooks and Rudd, 1970), where the ejected electron has a low relative velocity with respect to the scattered projectile.

Chapter 6

Conclusions and Suggestions for Future Work

6.1 Summary and Conclusions

A detailed study has been carried out, into both positron and Ps detection efficiencies of a channel electron multiplier array (CEMA2), in order to obtain the absolute magnitude of the Ps break-up cross-section. Two methods have been used in this study: the first employed positrons whose velocity matched that of the Ps beam. In this way, the positron detection efficiency as a function of impact velocity was determined, and found to increase by 12% with increasing impact velocity. The second method measured the Ps detection efficiency directly, the measurements however rely on the estimation of a number of associated branching ratios. A good agreement has been found between the two (equivelocity positron and Ps) methods once elastic scattering of the slow positron/Ps atoms, Ps formation from the residual positrons and break-up of the incident Ps at the surface of the channel plates are taken into account. This indicates that for these two projectiles the impact velocity is the dominant factor in determining their detection efficiency.

Absolute cross-sections have been measured for the first time for Ps break-up in collision with He atoms, in the energy range 10-40eV, using the detection efficiency values determined for both Ps and positrons. The present results are found to be in good agreement with the theory of Blackwood *et al* (1999) and roughly a factor of two lower than the theory of Biswas and Adhikari (1999). A comparison of our cross-sections, with calculations for the total and partial cross-sections of Blackwood *et al* is given in figure 6.1. As can be seen from figure 6.1, apart from the lowest energy, the calculation by Blackwood *et al* underestimates the measured total cross-section, suggesting either an underestimate of the elastic cross-section and/or of target inelastic effects, across the energy range shown. Estimates of the cross-sections for He excitation and ionisation have been made by Blackwood *et al* (1999) within the

First Born Approximation and found to be negligible at these energies. A rigorous study into target inelastic effects would now seem to be urgently needed in order to progress with the understanding of the Ps-He collision system.

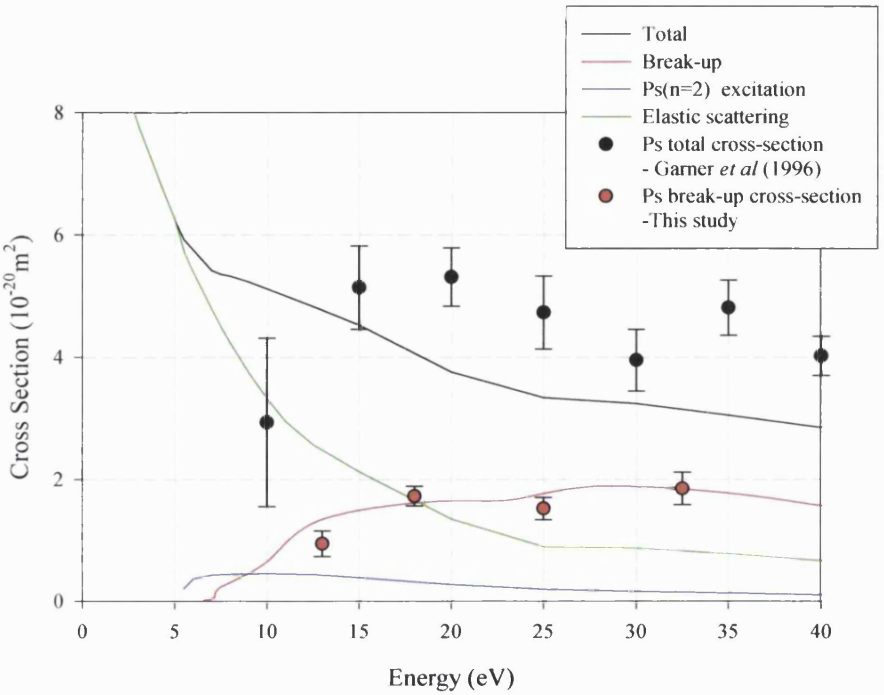

Figure 6.1 Comparison of experimental Ps-He cross-sections with the calculations of Blackwood et al (1999).

From the time-of-flight spectra, a measure of the longitudinal energy distributions of the residual positrons from Ps break-up has been obtained. A peak is observed, at each incident Ps energy, just below half of the residual energy. This is suggestive of the occurrence of a process similar to electron-loss-to-the-continuum (Crooks and Rudd, 1970) in ion/atom-atom collisions.

6.2 Outlook and Future Work

Several new developments are planned as an extension to this study. A new Ps detector is being developed which will attempt to make use of the fraction of the undetected Ps atoms due to elastic reflection. This new detector comprises sphere-plates (rather than channel) in the hope that the Ps atoms may be trapped within the detector, where extra surfaces are available for any elastically scattered Ps atoms to be detected.

Further work is required to quantify the positron elastic scattering probability from the surface of the channel plates at 250eV. Increasing the separation of the grids in front of the channel plates should allow higher resolution of the coincidence rate correlated to positron annihilation on each respective grid, such that the fraction of elastically scattered positrons may be determined. Increasing the separation between the respective grids may also serve to give a measure of the Ps formation from the backscattered positron beam, especially at low energies where Ps formation is thought to be close to 50% (Howell, 1987). This technique may also be applied to Ps scattering from surfaces to give a measure of the elastically backscattered Ps fraction. In the first instance, this would be applied to the channel-plates used in this study and may be extended to targets such as Al, Au, Cu and Ni.

The Ps break-up study is to be extended into looking at the electrons emitted through Ps break-up. In this way, the cross-section for target ionisation will be determined through subtraction of the Ps break-up cross-section, determined by measuring the residual positrons. These measurements are important for the partitioning of the Ps-He total cross-section and to resolve current discrepancies between theory and experiment, as target inelastic effects may become dominant at energies above 30eV.

Further work is required in reducing the experimental uncertainty in the Ps-He total cross-section at 10eV. As stated in chapter 3, the low energy total cross-section value obtained in this study tends to increase the likelihood of a down turn in the total cross-section at lower energies. This is contrary to the results of Blackwood *et al,* whereby the total cross-section increases at lower energies. Considering the consistency between the break-up cross-section values determined in this study and the calculation of Blackwood *et al*, accurate low energy total cross-section

measurements are required to aid the understanding of the current discrepancy with corresponding theoretical results.

In order to improve the time-of-flight energy distributions, a higher incident positron energy may be used in order to reduce the epithermal contribution to the remoderated beam constitution. An improvement in the remoderated positron energy distribution should aid the understanding of the Ps energy distributions. Only by improving the systematic timing resolution may any contribution to the Ps energy spread from the recoil of the target atoms/molecules be inferred using this detection system.

Protocol for the Removal or Installation of Radioactive Sources on the Magnetic Beam in B15

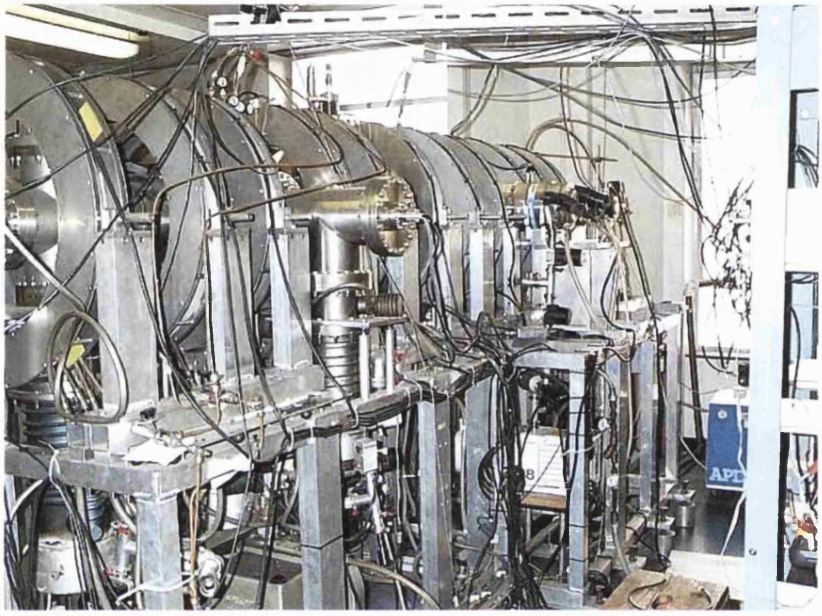

LIST OF CONTENTS

1. Who is allowed to carry out the procedure

This booklet provides guidance on a specific beamline and is in addition to general rules concerning work with ionising radiation. Persons may carry out the procedure if they are registered radiation workers, carry a valid and current radiation monitoring film badge and if they have familiarised themselves with the procedure as set out in this protocol booklet to the satisfaction of the RPO, who must have observed the worker's technique on a practice run without a radioactive source. A record must be made under Section 6 of where the person is registered and, if outside UCL, of the name and address of their Radiation Protection Officer. Temporary registration and issue of film badge for a visitor may be carried out at UCL if necessary. Two people are necessary to carry out this particular procedure.

Please note the following

1) Departmental RPO,	Q A Pankhurst,	ext3514
2) Deputy departmental RPO,	G Laricchia,	ext3470
3) College RPA,	P Marsden,	Should be contacted through 4.
4) Safety Advisory Unit,	E Clarke,	ext6944

2. Tool list and description

2.1 List of tools

Assemble the following tools:

a) Cup jig.
b) Source Jig.
c) Jig Cradle with lead shield.
d) Extended tongs and Gripper.
e) Lead Pot Source Container.
f) Large Yellow Lead Pot/Medium Grey Lead Pot.
g) Pneumatic trolley.
h) Mirrors.
i) 48 Leads Bricks.
j) Geiger counter, film badges, TLDs, gloves, goggles, long tweezers.
k) Barrier stands.

2. 2 DESCRIPTION OF TOOLS

a) The Cup Jig.

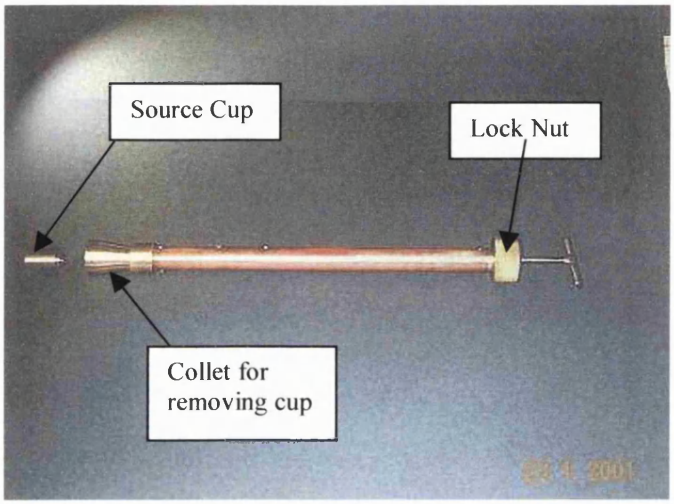

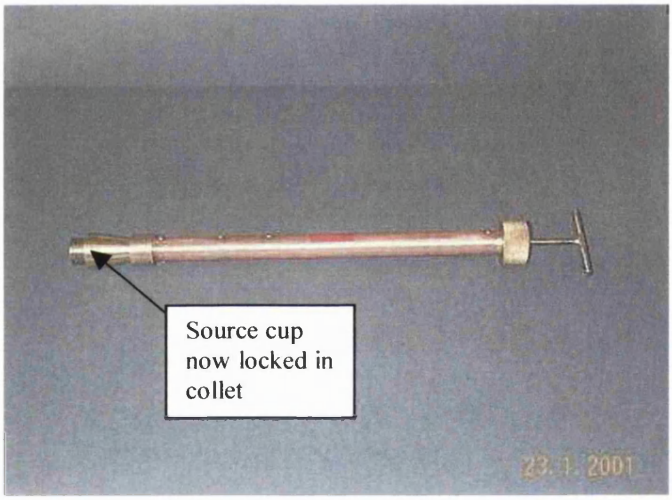

The **Cup Jig** is used to remove the cup from the cryostat cold head. With the cullet loose, the jig is placed over the cup. Once placed over the cup, the **Lock Nut** is tightened to grab the cup. When tight, the whole jig can be rotated such that the cup is unscrewed from the cold head. ONLY rotate the jig by the handle and not by the **Lock Nut** as this will undo the cullet and let go of the cup.

The cullets for both cup and source jig are made from brass. After a few uses the cullets have a tendency not to spring back to there original position. When this happens the cup/source gets harder to let go from the cullet and in extreme cases can become locked into the cullet. Before using, the cullets should be tested as to there springiness and in cases where cup/source are getting stuck, or are difficult to release, the cullet should be manually opened apart a little until cup/source is easily released.

b) The Source Jig.

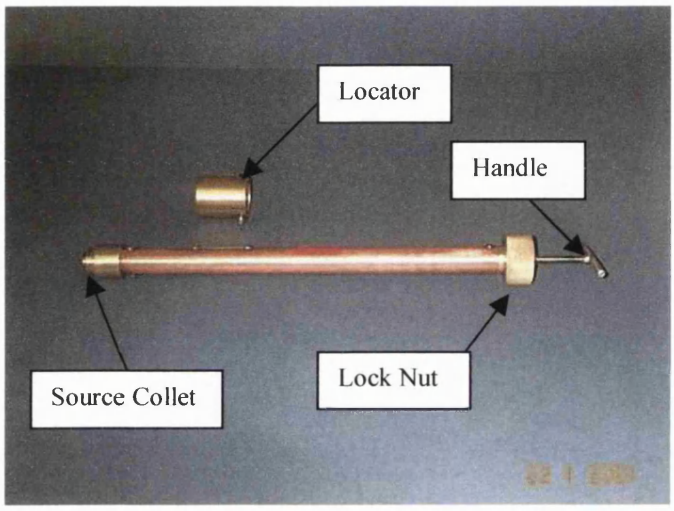

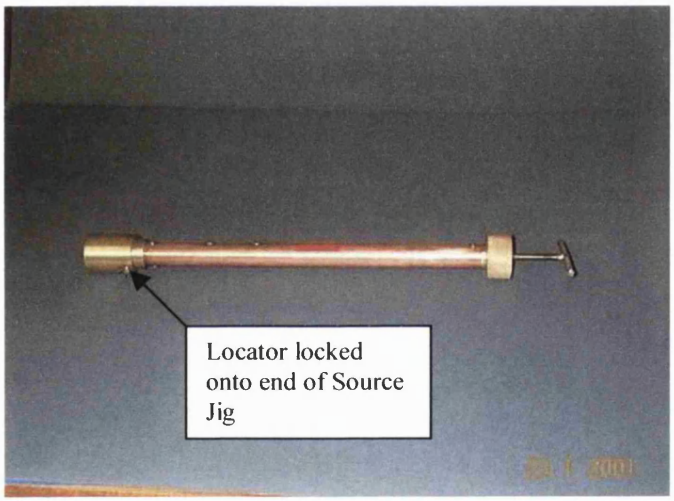

The **Source Jig** is used to remove the radioactive source from the cold head of the cryostat. The **Locator** is used to guide the source cullet over the source.

The **Locator** is placed over the cullet end of the **Source Jig** and held in place with two screws. The **Locator** slides over the source holder on the cold head such that the cullet is inline with the source.

Once the cullet is over the source, the **Lock Nut** is tightened such that the cullet grips onto the source. Rotating the whole jig thus unscrews the source such that it can be removed.

When rotating the jig do not use the **Lock Nut** as this can unscrew the source. ONLY use the **Handle** to turn the jig when the source is locked into the cullet.

c) Jig Cradle with Lead Shield.

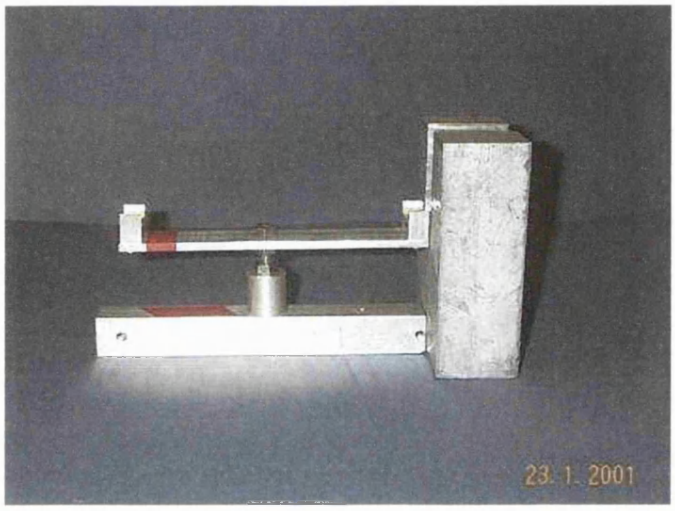

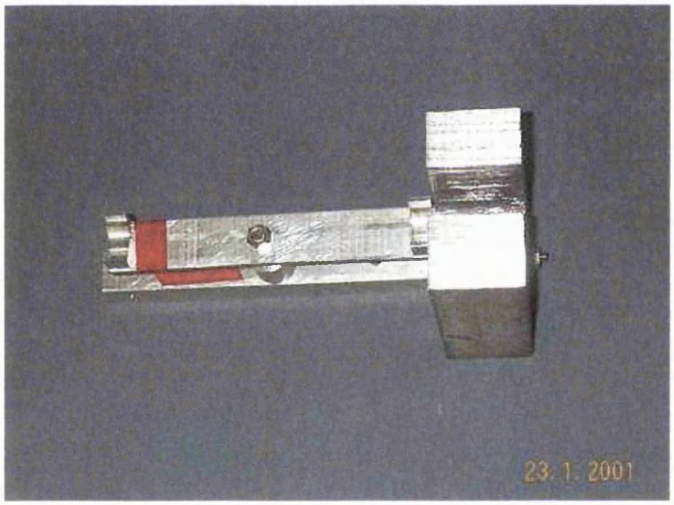

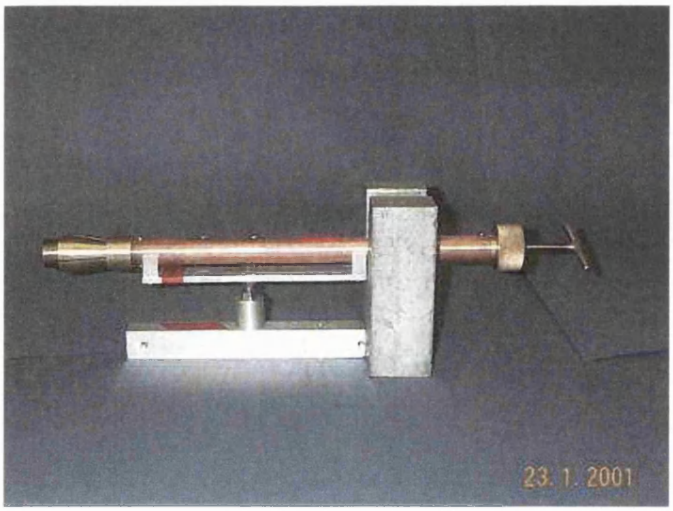

The **Jig Cradle with Lead Shield** is used to support the **Source/Cup Jig** such that the jig will slide directly onto the cold head. The cradle is set at a height such that the jig is directly in line with the cryostat cold head. Once the jig has been placed on the cradle, it only has to be slid along to locate over the source/cup.

The cradle has a groove along the bottom exactly the same size as the rail on which the cryostat sits. With the cradle sitting on the rail, the **Source/Cup Jig** will be in line with the cold head.

The cradle is screwed directly into a U-shaped lead brick such that hands are shielded from the source at all times when putting the cradle in place or using either of the jigs.

The U-shaped lead brick has a groove cut into the bottom as well as the cradle such that it will sit on the rail directly in line with the source.

d) Extended Tongs and Grippers.

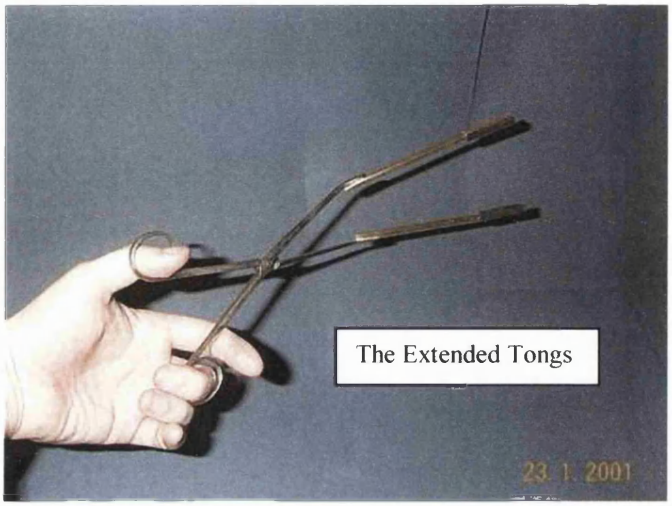

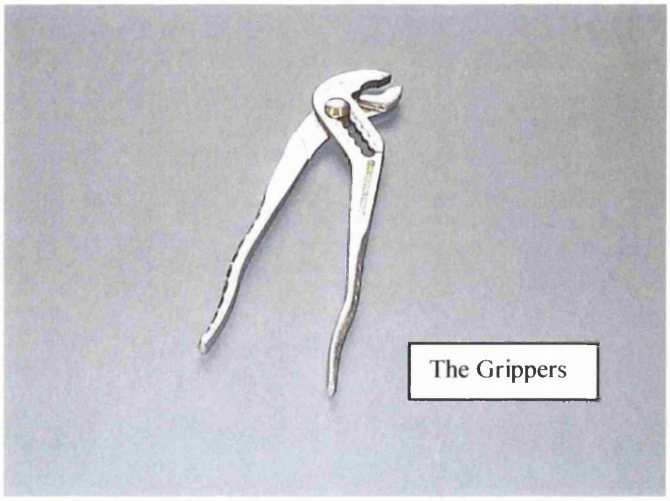

The **Extended Tongs** are utilised to hold the source holder on the cold finger to stop it from unscrewing whilst removing source /cup.

They have been made at an angle so your hand can stay behind the lead wall built either side of the cryostat and still reach the cold head (see section 3b).

Sand paper has been glued onto the extensions to get a better grip of the source holder on the cold head.

The process of removing the source requires two people: One to use the tongs and one to use the jig (see section 3b for positions).

The **Grippers** are used to hold the heat shield whilst the cryostat is being pulled back.

e) Lead Pot Source Container.

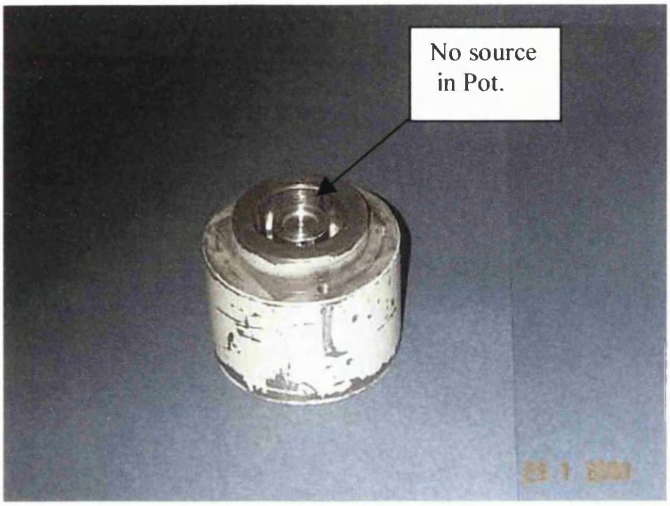

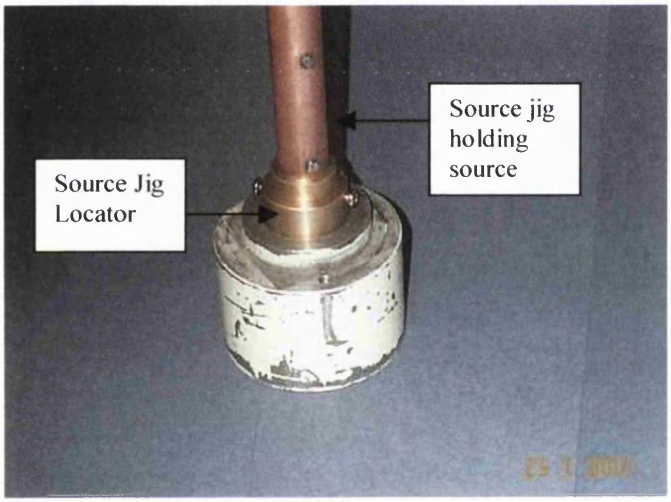

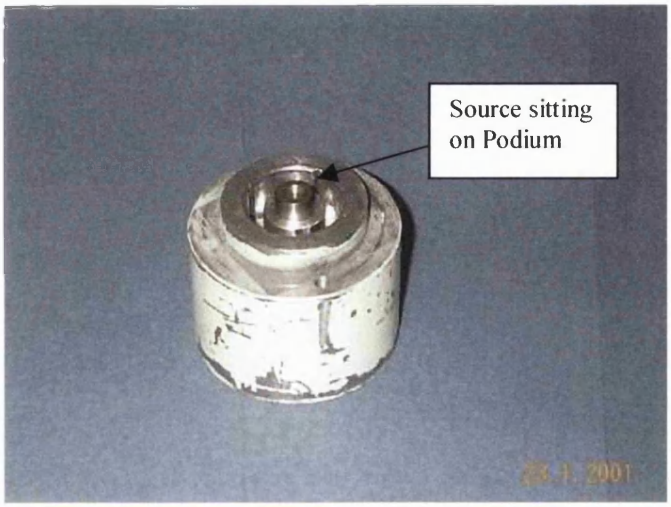

The **Lead Pot Source-Container** is placed in the centre of a much larger lead container (see section f). So that, once the source is out of the system, it may be contained safely within the pot.

With the source safely clamped into the cullet of the **Source Jig**, the **Source Jig** is lowered source-end first into the pot. The pot is designed to accept the **Locator** such that when the **Locator** is inside the pot the source is sitting on the podium in the middle of the pot. Undoing the lock nut on the jig and withdrawing will leave the source safely inside the pot.

To remove the source from the pot, the **Source Jig** is lowered into the pot until it sits there. Tighten the lock nut and remove the jig. The source will now be locked in the cullet ready to be put back onto the cryostat cold head.

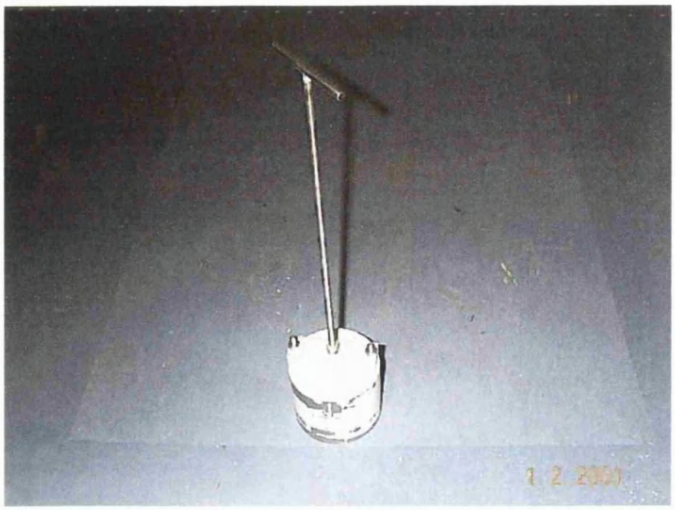

The **Lead Pot Source Container** lid is attached to an aluminium bar. The bar is threaded such that a piece of threading can be screwed into the lid to lower into the **Large Yellow Lead Pot.** Once the lid is inside the thread can be unscrewed and the lead plug dropped in to seal the **Large Yellow Lead Pot.**

To remove the lid from the **Lead Pot Source Container** the plug is removed and the threaded bar is screwed back into the aluminium bar. The bar has a chamfer to help locate the thread on the bar.

f) Large Yellow Lead Pot/Medium Grey Lead Pot.

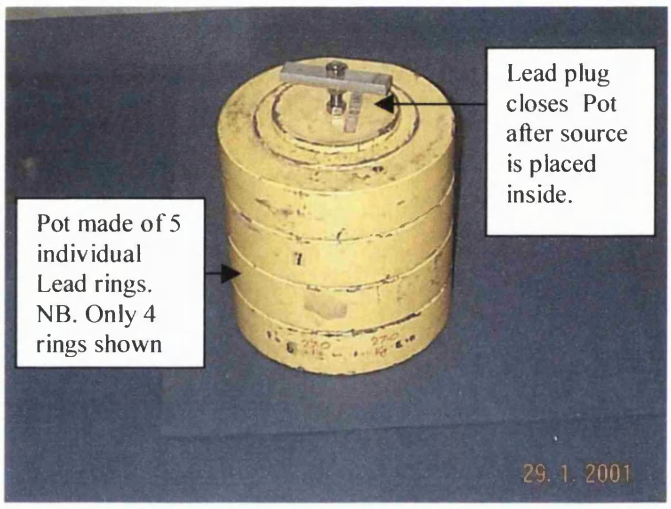

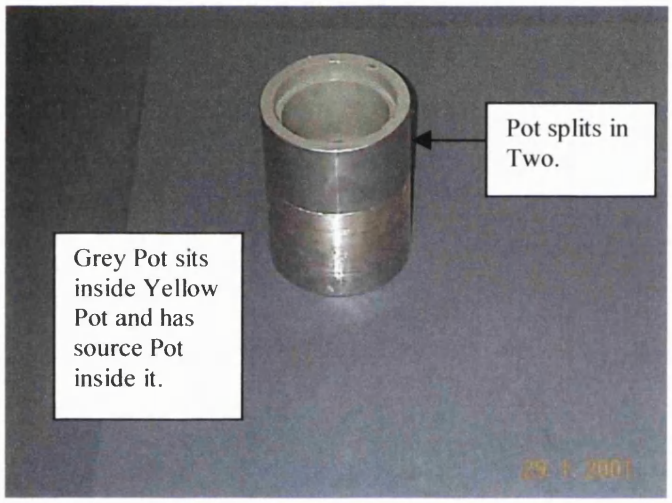

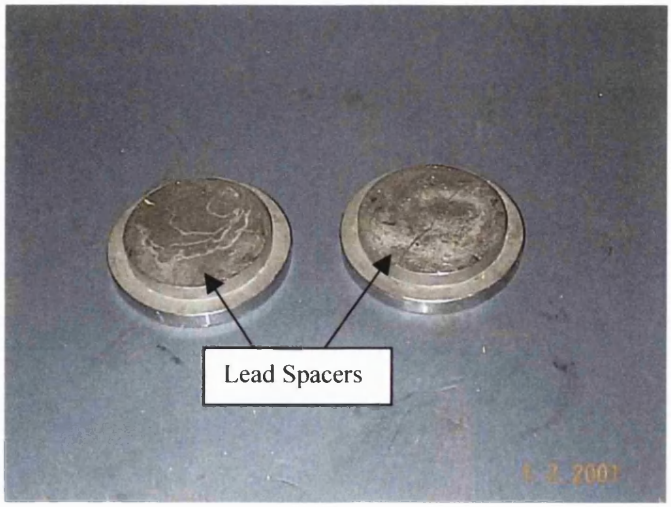

The **Large Yellow Lead Pot** consists of 5 large lead rings. The rings are placed on top of each other to make a large lead cylinder. Inside this sits a **Medium Grey Lead Pot** in which the Lead **Pot Source Container** is located. The **Complete Lead Cylinder** has to have a layer of 2 lead bricks surrounding it to make sure its safe (see section 3c).

The dose measured at the outer surface of the lead surrounding the **Complete Lead Pot** should not be higher than 1.2 $\mu Svhr^{-1}$. With a source activity of 2.9×10^{9} Bq (78mCi) on 5/2/01, we need at least 10cm of lead around the source to achieve this dosage. This will require about 20 Pb Bricks (see section 3b)

Once inside the **Large Yellow Lead Pot** the **Medium Grey Pot** sits on two **Lead Spacers** to lift the source up such that its sits in the middle of the complete lead pot. For a complete diagram of the lead pot configuration see section 3c.

Once the source is inside the **Complete Lead Cylinder** a lead plug fits into the top to completely enclose it.

A spare lead pot should be kept on standby should the cup be contaminated. In this case place the cup inside the spare grey pot and carry on with the procedure. With both the cup and source secure check whether any other part of the system is contaminated and seek advice from the RPO in the first instance.

The **Complete Lead Pot** sits on a pneumatic trolley (obtained from PA stores). The trolley is raised to its full height such that the **Complete Lead Pot** is around waist height. If the source needs to be stored, then it can be wheeled into the radiation cupboard where it can remain safely until required.

3. SCHEMATICS

a) Cryostat Schematic

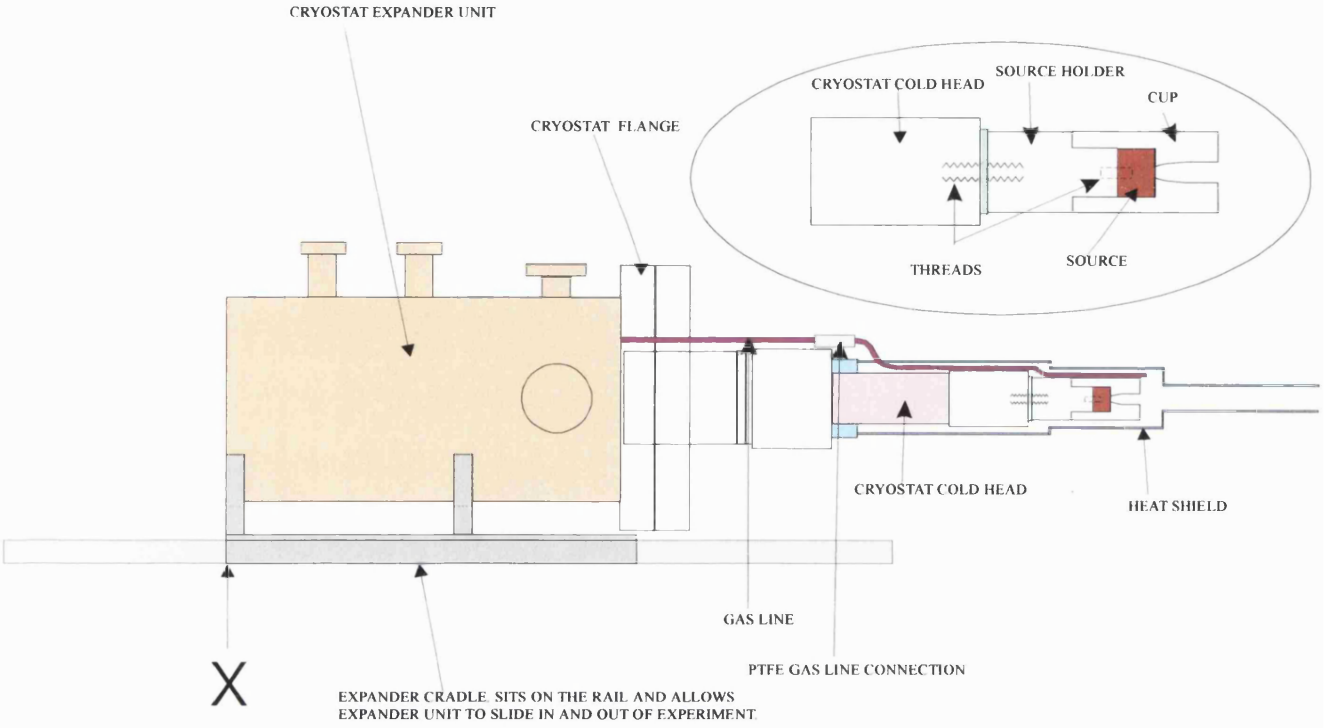

PROCEDURE FOR WITHDRAWING CRYOSTAT.

1) Lead Brick Wall has to be built up before removing cryostat (see section b).
2) Unscrew Cryostat Flange.
3) Pull back until PTFE Gas Line Connection Shows.
4) Pull back PTFE connection until gas lines are disconnected.
5) Unscrew Heat Shield (the thread is at the same position as PTFE gas line connection)
6) Hold Heat Shield in right hand with grippers and pull back cryostat with left hand. When the cryostat is clear of the heat shield, leave heat shield in the chamber.
7) Pull cryostat back until the cryostat cradle reaches mark X, 9.5cm from end of the rail (such that the source will be 7 cm in from end of experimental bench, and is located behind the lead wall).

b) Layout Schematic

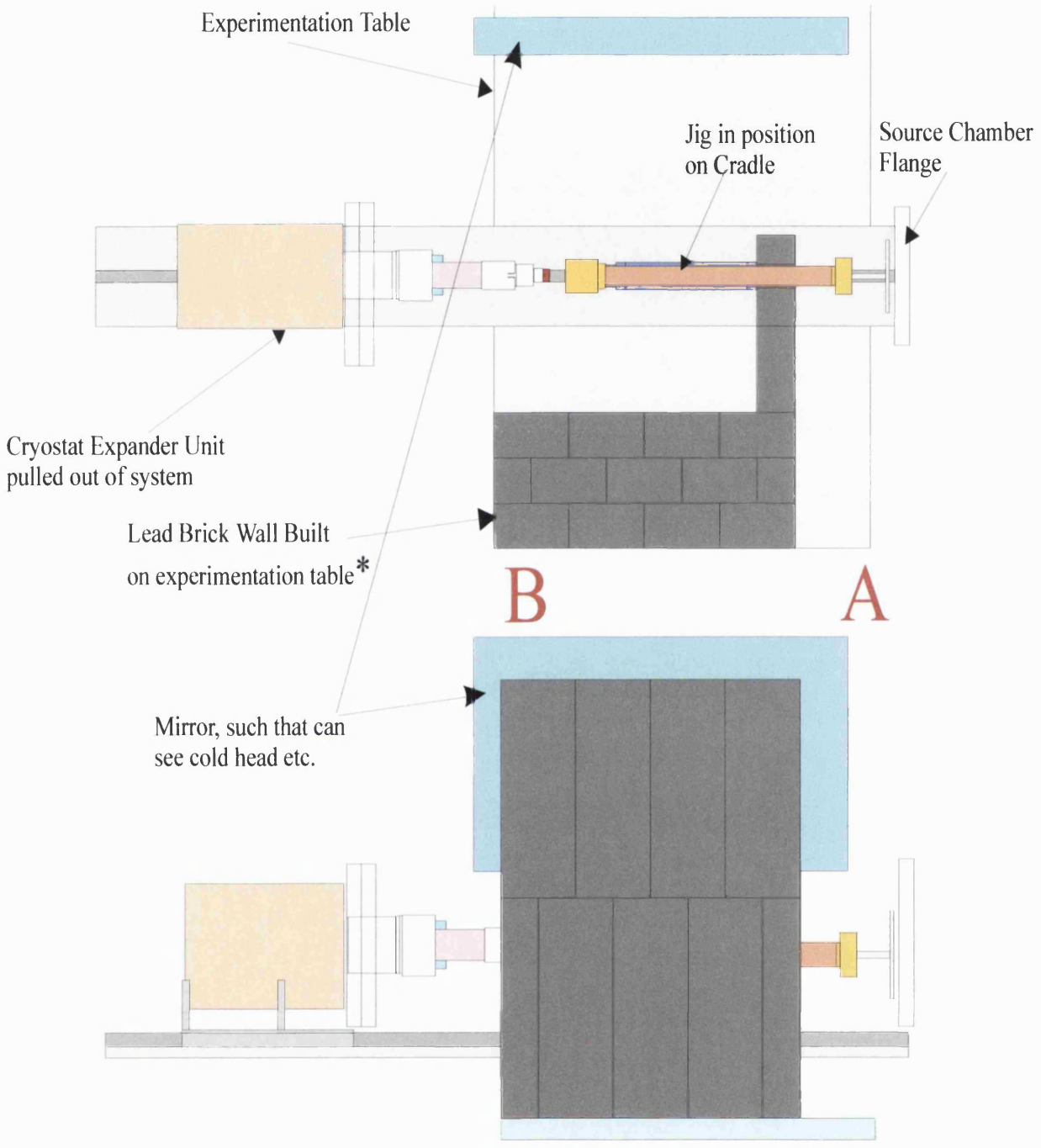

*The lead Brick Wall requires 28 Pb bricks, three of which have been specifically machined in half to fit into the corners of the wall. These three machined Pb bricks can be found on the table underneath the rail.

NOTES:-

- Place three lead bricks under the rail.
- Put mirror in position, so both positions **A** and **B** can see cold head with having to directly look at the source.
- Once cryostat has been pulled back, the person in position **A** is responsible for
  a) Placing **Jig Cradle with lead shield** onto the rail.
  b) Removing cup/source with jig.
  c) Putting source into **Complete Lead Pot,** see section 3c.

  -Apart from c) all the tasks are done behind the right hand side of the lead brick wall.

- The person in position **B** is responsible for using the **Extended Tongs** to stop the source holder, on the cold head, from rotating. This task is done behind the left hand side of the lead brick wall.

c) Complete Lead Pot Schematic

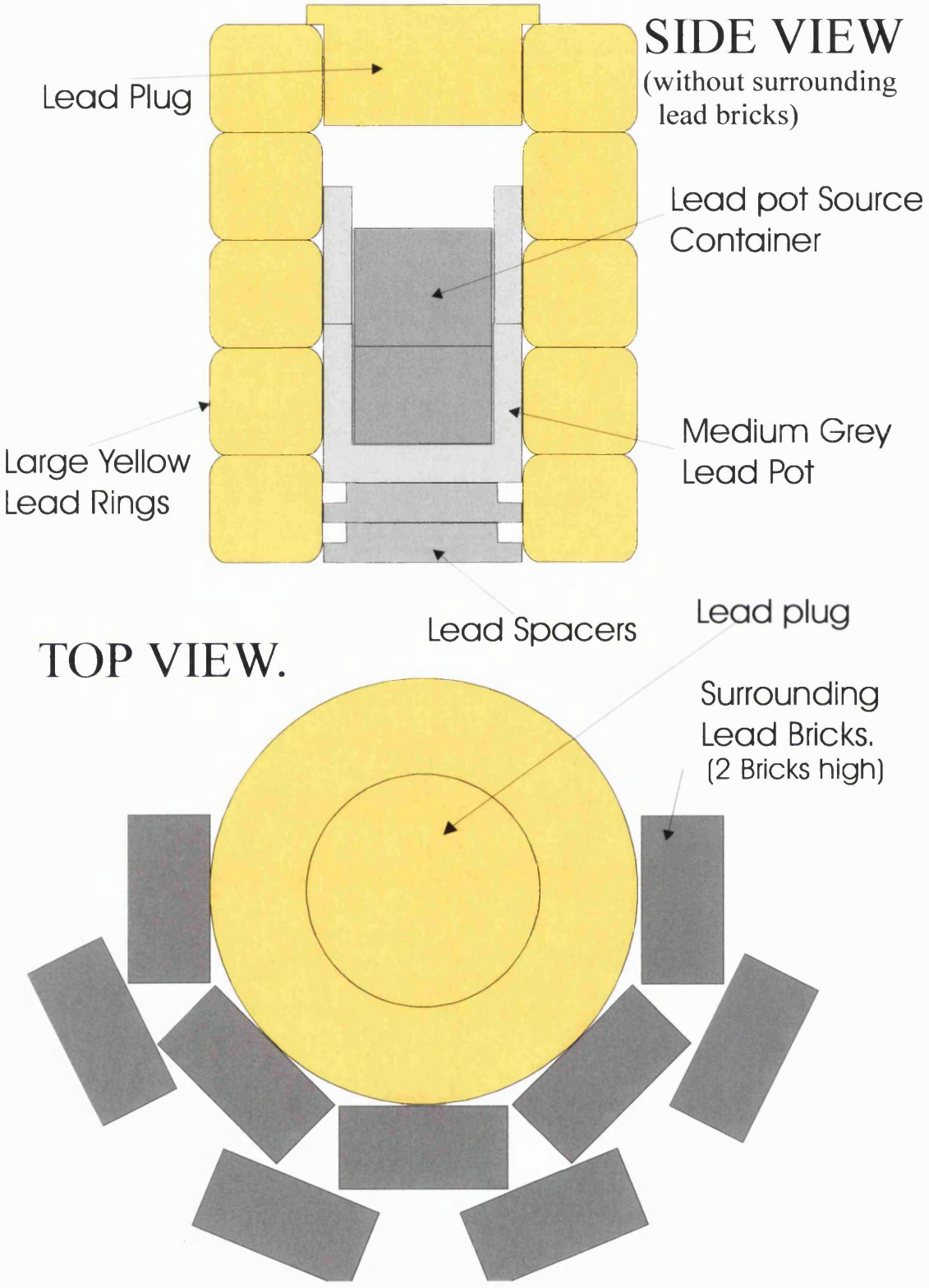

4. METHOD

Before starting to remove source make sure that

a) You are wearing your radiation badge and goggles.
b) Place TLD's over fingers and cover with lab gloves.
c) Lock lab door. Outside you should have positioned a barrier to prevent others, who have keys, from accidentally entering during the procedure.

You may now start to remove the source.

1) Put together **Complete Lead Pot** on the pneumatic trolley and position lead bricks around it, see section 3c.

2) Position the **Geiger Counter** in a well shielded area to reduce the background from the source once it is pulled out of the system. You will need the low background level to check for contamination of the cup.

3) Remove all cables from cryostat expander unit. (leave lead where it is around cryostat expander unit).

4) Flush source end with N_2 to bring to atmosphere.

5) Disconnect gas line from system side of needle valve.

6) Remove needle valve and gas line from system (keep needle valve closed so as not to open to atmosphere).

7) Position Lead Brick wall on the experimentation table by the side of the cryostat, see section 3b.

8) Position mirror, see section 3b.

9) Withdraw the cryostat, see section 3a.

10) Place **Jig Cradle and Lead Shield** into position, see section 3b.

11) Remove cup using **Cup Jig**, see section 2.2. Check for contamination using the **Geiger Counter**. Remove Source using **Source Jig**, see section 2.2. Once the source is unscrewed the person in position B can retire to safe position.

12) Quickly place source in **Complete Lead Pot**, where the source will sit until removed by **Source Jig**. When **Source Jig** is being removed from the **Cradle** always keep it at arms length with the source end as far away from your body as possible.

5. In case of emergencies

Should the *source be dropped*, a quick assessment should be made regarding whether the source can be picked up safely i.e. within about 10 seconds, with e.g. the extended tongs or long tweezers and placed in the Pb container or pushed safely in a corner (e.g. with a broom) where Pb shielding may be placed. If in doubt, exit the room, lock the door and ask for assistance of the RPO.

In case the *Fire Alarm* should sound whilst carrying out the procedure, you should aim at leaving the source in a safe place (e.g. push it back in the beamline or placing it in the Pb container, whichever is faster) if this can be done promptly. Follow the usual Fire Alarm procedure but lock the door and leave the barrier in front of the door if the procedure is not completed. Inform the Fire Officer promptly.

Should you find the moderator cup to be *Contaminated*, place the cup in the spare grey pot and continue with the procedure. With both the cup and source safely housed, check whether any other part of the system is contaminated and seek the advice of the RPO.

In general, if any problem should arise, first quickly assess the situation and decide on the quickest way to make the situation safe. If the source is still attached to the cryostat cold head then the safest thing to do is quickly remove **Jig Cradle and Lead Shield** and slide cryostat back into the system. Then seek advice from the RPO. If the source is off the cryostat then the safest place for it is inside the **Complete Lead Pot.** All actions should be taken as quickly and safely as possible and the department and RPO should be informed of any problems.

6. People Allowed to Carry Out the Procedure

Name	Affiliation	Approved by	Date

7. Record of procedures carried out and doses received

Date: .....
Carried out by: .....
Name and Address of RPO: .....
Comments (please note especially if anything different from the expected procedure occurred):

Dose (enter when known)

Date: .....
Carried out by: .....
Name and Address of RPO: .....
Comments (please note especially if anything different from the expected procedure occurred):

Dose (enter when known)

Appendix B - The full fitting equation used in the determination of |W| + C.

As stated in chapter 3, the time between the tagger and CEMA2 pulses is given by

$$t_+ = t_{const} - t_{e^-} + t_{e^+} + t_{rets},$$

where

$$t_{const} = \left(\frac{m}{2eE_{e^+}}\right)^{\frac{1}{2}} D,$$

and D is the positron flight length between the tagger earth grid (see section 2.6.1) and the grid R1 (see section 2.6.3) and E_{e^+} is the positron kinetic energy and is given by the remoderator potential, V_m, and the workfunction and contact potential $|W| + C$ as

$$E_{e^+} = V_m + |W| + C$$

The time for secondary electrons, released from the remoderator by positron impact, to be accelerated to the tagger channel-plates is

$$t_{e^-} = d1\left(\frac{2m}{e}\right)^{\frac{1}{2}} \Delta V^{-\frac{1}{2}},$$

where $d1$ is the separation of the remoderator and channel-plates and ΔV is the potential difference between them. The time for the remoderated positron to be accelerated to the tagger earth grid is given by

$$t_{e^+} = d2\left(\frac{2m}{e}\right)^{\frac{1}{2}} \frac{\left((V_m + W)^{\frac{1}{2}} - W^{\frac{1}{2}}\right)}{V_m},$$

where $d2$ is the remoderator-earth grid separation and W is the remoderator workfunction.

The time taken for the positron to be accelerated through the grids in front of CEMA2 is given by

$$t_{rets} = t_{R1} - t_{R2} - t_{R3},$$

where

$$t_{R1} = d3\left(\frac{2m}{e}\right)^{\frac{1}{2}}\left(\left(E_{e^+} + 400\right)^{\frac{1}{2}} - \left(E_{e^+}\right)^{\frac{1}{2}}\right),$$

is the time for the positron to be accelerated from R1 to R2 and $d3$ is the grid separation. Similarly for R2 to R3,

$$t_{R2} = d4\left(\frac{2m}{e}\right)^{\frac{1}{2}}\left(\left(E_{e^+} + 300\right)^{\frac{1}{2}} - \left(E_{e^+} + 400\right)^{\frac{1}{2}}\right)$$

and d4 is the grid separation. Finally, between R3 and the CEMA2 channel plates (separated by $d5$),

$$t_{R3} = d5\left(\frac{2m}{e}\right)^{\frac{1}{2}} \times \left(\left(E_{e^+} + V_F\right)^{\frac{1}{2}} - \left(E_{e^+} + 300\right)^{\frac{1}{2}}\right)$$

where V_F is the potential applied to the front of the channel-plates.

Appendix C

The following plots are the residual positron yield, taken for different He pressures, as discussed in section 5.2.2

13eV 7A

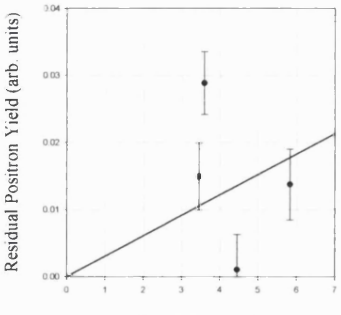

13eV 9A

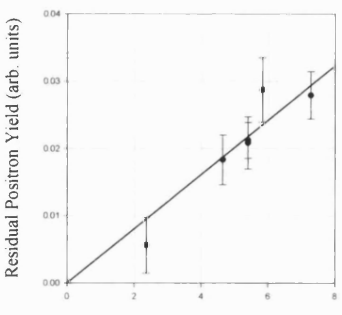

18eV 3.9A

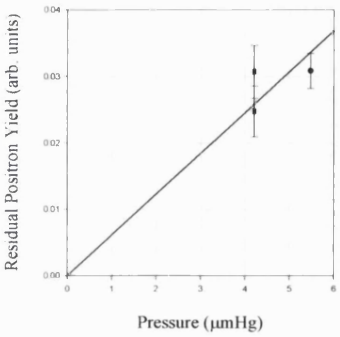

18eV 7A

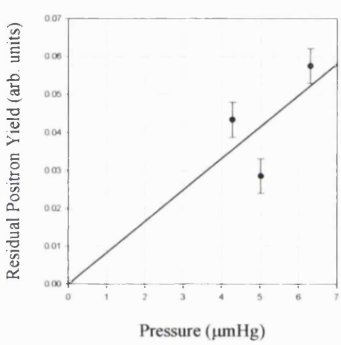

18eV 9A

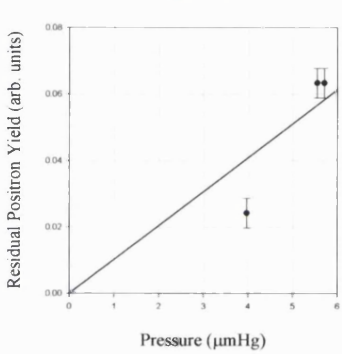

25eV 3.9A

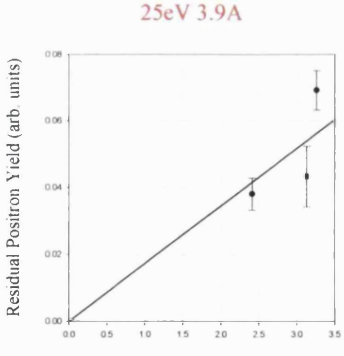

25eV 7A

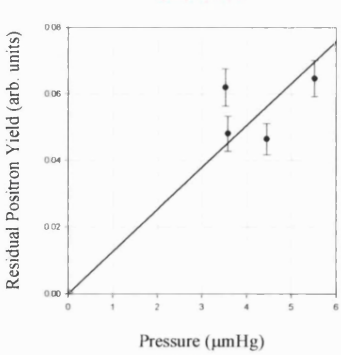

25eV 9A

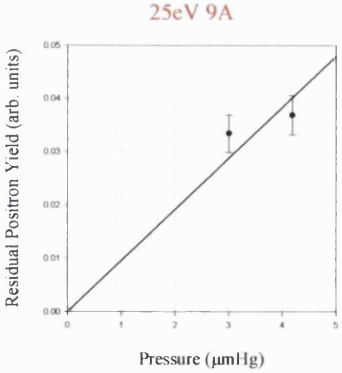

35eV 3.9A

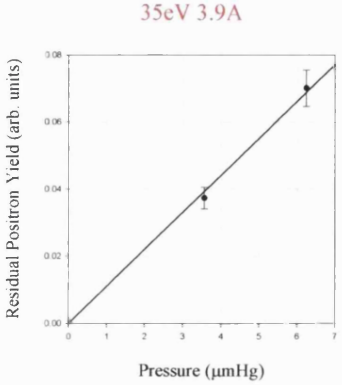

35eV 7A

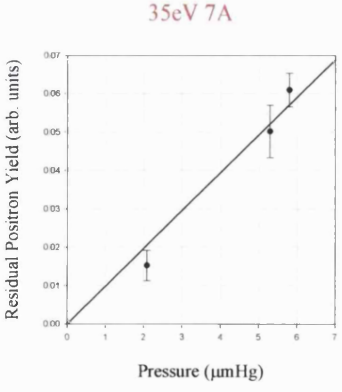

35eV 9A

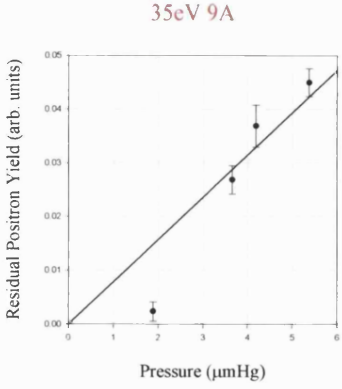

References

Adachi S, Chiba M, Hirose T, Hagayama S, Nakamitsi Y, Sato T and Yamada T, *Phys Rev Lett* ***65*** *(1990) 2634*

Adhikari S K, *Phys Rev A* ***64*** *(2001) 022702*

Adkins G S, *Ann Phys (NY)* ***146*** *(1983) 18*

Adkins G S, Salahuddin A A and Schalm K E, *Phys Rev A* ***45*** *(1992) 7774-7781*

Al-Ramadhan A H and Gidley D W, *Phys Rev Lett* ***72*** *(1994) 1632-1635*

Anderson CD, *Science* ***76*** *(1932a) 238*

Phys Rev ***41*** *(1932b) 405*

Phys Rev ***43*** *(1933) 491*

Asai S, Orito O and Shinohara N, *Phys Lett B* ***357*** *(1995) 475*

Baille P and Darewych J W, *Journal de Physique Lettres* ***35*** *(1985) 243*

Baker J A, Touat M and Coleman P G, *J Phys C* ***21*** *(1988) 4713-4720*

Baluja K L and Jain A, *Phys Rev A* ***46*** *(1992) 1279-1290*

Basu A, Sinha P K and Ghosh A, *Phys Rev A* ***63*** *(2001) 052503*

Belloti E, Corti M, Fiorini E, Liguori C, Pullia A, Sarracino A, Sverzellati P and Zanotti L, *Phys Lett B* ***124*** *(1983) 435*

Bennani A L, Pebay B and Nguen B, *J Phys E* ***6*** *(1973) 1077*

Berakdar J, *Phys Rev Lett* ***81*** *(1998) 1393*

Blackett P M S and Occhialini G P S, *Proc Roy Soc A* ***139*** *(1933) 699*

Blackwood J E, Campbell C P, McAlinden M T and Walters H R J, *Phys Rev A 60 (1999) 4454*

Blackwood J E, McAlinden M T and Walters H R J, *J Phys B (2002) in press*

Biswas P K and Adhikari S K, *Phys Rev A 59 (1999) 363*

Biswas P K and Adhikari S K, *J Phys B* ***33*** *(2000) 1575-1584*

Bransden B H, *"Case Studies in Atomic Collisions" eds. McDaniel and McDowell (North Holland) (1969) 171*

Brown B L, *Bull Am Phys Soc* ***30*** *(1985) 614*

Brown B L and Leventhal M, *Astrophys J* ***319*** *(1987) 637-642*

Brown B L, *"Positron (Electron) – Gas Scattering" eds. W E Kauppila, T S Stein and J M Wadehra (Singapore: World Scientific) (1986) 212*

Campbell C P, McAlinden M T, MacDonald F G R S and Walters H R J, *Phys Rev Letts.* ***70*** *(1998) 5097*

Campbell L, Brunger M J, Nolan A M, Kelly L J, Wedding A B, Harrison J, Teubner P J O, Cartwright D C and McLaughlin B, *J Phys B* ***34*** *(2001) 1185-1199*

Canter K F, Coleman P G, Griffith T C and Heyland G R, *J Phys B* ***5*** *(1972) L167*

Chang T, Li Q, Wang Y and Li Y, *"Positron Annihilation" eds. P Coleman, S C Sharman and L M Diana (North Holland: Amsterdam) (1982) p32*

Chang T, Li Q, Wang Y and Li Y, *"Positron Annihilation" eds. P C Jain, R M Singru and K P Gopinathan (Singapore: World Scientific) (1985)p 212*

Charlton M, *Rep Prog Phys* ***48*** *(1985) 737*

Charlton M and Laricchia G, *Comm At Mol Phys* ***26*** *(1991) 253*

Charlton M and Humberston J W, *"Positron Physics" (Cambridge University Press, 2000)*

Cherry W, *PhD Thesis (1958) Princeton University*

Chutjian A and Cartwright D W, *Phys Rev A* ***23*** *(1981) 2178*

Coleman P G, Hutton J T, Cook D R and Chandler C A, *Can J Phys* ***60*** *(1982) 584*

Coleman P G, Rayner S, Jacobsen F M, Charlton M and West R N, *J Phys B* ***27*** *(1994) 981*

Costello D G, Groce D E and Zecca A, *Phys Rev B* ***5*** *(1972a) 1433*

Costello D G, Groce D E, Herring D F and McGowan J W, *Can J Phys* ***50*** *(1972b) 23*

Crooks G B and Rudd M E, *Phys Rev Lett* ***25*** *(1970) 1599*

Czernin J and Phelps E P, *Annu Rev Med* ***53*** *(2002) 89-112*

Davies S A, *PhD Thesis* (1987) *University College London*

Dale J M, Hulett L D and Pendyala S, *Surf Sci Anal* ***2*** *(1980) 199*

DeBenedetti S, Cowan C E and Konnecker W R, *Phys Rev* ***76*** *(1949) 440*

DeBenedetti S, Cowan C E, Konnecker W R and Primakoff, *Phys Rev 77 (1950) 205*

Deutsch M, *Phys Rev* ***82*** *(1951) 455*

Dirac P A M, *Proc Roy Soc A* ***126*** *(1930a) 360*

Dirac P A M, *Proc Camb Phil Soc* ***26*** *(1930b) 361*

Dupasquier A, *inPOS81 (1981) 510*

Dupasquier A and Zecca A, *Rivista Del Nuovo Cimento* ***8*** *(1985) 2276*

"Electron Multipliers", Phillips Components (1991) p16

Fiol J, Rodríguez V D and Barrachina R O, *J Phys B* ***34*** *(2001) 933*

Fiol J and Olsen R E, *J Phys B* ***35*** *(2002) 1173-1184*

Fulton T and Martin P C, *Phys Rev* ***95*** *(1954) 811*

Garner A J and Laricchia G, *Can J Phys* **74** (1996) 518

Garner A J, Laricchia G and Özen A, *J Phys B* ***29*** *(1996) 5961*

Garner A J, *PhD Thesis* (1997) *University College London*

Garner A J, Laricchia G and Özen A, *NIMB* ***143*** *(1998) 155*

Garner A J, Özen A and Laricchia G, *J Phys B* ***33*** *(2000) 1149-1157*

Gianturco F A, Murkherjee T and Paioletti P, *Phys Rev A* ***56*** *(1997a) 3638*

Gianturco F A and Murkherjee T, *J Phys B* ***30*** *(1997b) 3567*

Gidley D W, Rich A, Sweetman E and West D, *Phys Rev Lett* ***49*** *(1982) 525*

Gidley D W, McKinsey D N and Zitzewitz P W, *J Applied Phys* ***78*** *(1995) 1406*

Gilbert S J, Kurz C, Greaves R G and Surko C M, *Appl Phys Letts* ***70*** *(1997) 1944*

Gilbert S J, Barnes L D, Sullivan J P and Surko C M
Phys Rev Lett ***88*** *(2002)043201*

Goodyear A, Knight A P and Coleman P G, *J Phys E* ***6*** *(1994) 9601-9611*

Gramsch E, Throwe J and Lynn K G, *Appl Phys Lett* ***51*** *(1987) 1862*

Greaves R G, Tindle M D and Surko C M, *Physics of Plasmas* ***1*** *(1994) 1439*

Greaves RG and Surko C M, *Can J Phys* **74** *(1996) 445*

Gribakin G F, *Phys Rev A* ***61*** *(2000) 022720*

Griffith T C and Heyland G R, *Phys Rep* ***39*** *(1978) 169-177*

Groce D E, Costello D G, McGowan J W and Herring W F,
Bull Am Phys Soc ***13*** *(1968) 1397*

Gullikson E M and Mills A P Jr, *Phys Rev Lett* ***57*** *(1986) 376*

Harris I and Brown L, *Phys Rev* ***105*** *(1957) 1656*

Hautojärvi P, *"Positrons in Solids" Topics in Current Physics* ***12***
(Springer, Berlin) (1979)

Heyland G R, Charlton M, Griffith T C and Wright G L, *Can J Phys* ***60*** *(1982) 503*

Hodges C H, *Phys Rev Lett* ***25*** *(1970) 284*

Howell R H, Rosenberg I J and Fluss M J, *Phys Rev B* ***34*** *(1986) 3069*

Howell R, *"Atomic Physics with Positrons", eds J W Humberston and E A G Armour 1987, Vol. 169, p215*

Howell R H, Rosenberg I J and Fluss M J, *Phys Rev B* ***34*** *(1986) 3069*

Hutchins S M, Coleman P G, Stone R J and West R N, *J Phys B* **20** *(1986) 282*

Ivanov I A, Mitroy J and Varga K, *Phys Rev Letts 87 (2001) 063201*

Iwata K, Greaves R F and Surko M C, *Phys Rev A* ***55*** *(1997) 3586*

Iwata K, Gribakin G F, Greaves R G and Surko C M. *Phys Rev A* ***61*** *(2000) 022719*

Jacobsen F M, Charlton M, Chevallier J, Deutch B I, Laricchia G and Poulsen M R, *J Appl Phys* ***67*** *(1990) 575*

Jääskeläinen J, Laine T, Fallström K, Saarinen K, and Hautojärvi P, *Appl Surf Sci* ***116*** *(1997) 73*

Jain A, *J Phys B* ***19*** *(1986) L379*

Kauppila W E, Stein T S and Jeison G, *Phys Rev Lett* ***36*** *(1976) 580*

Kauppila W E, Stein T S, Smart J H, Dababneh M S, Ho Y K, Downing J P and Pol V, *Phys Rev A* ***24*** *(1981) 725*

Khatri R, Charlton M, Sferlazzo P, Lynn K G, Mills A P Jr and Roellig L O, *Appl Phys Lett* ***57*** *(1990) 2374*

Khriplovich I B and Yelkhovsky A S, *Phys Lett B* ***246*** *(1990) 520-522*

Kimura M, Takekawa M and Itikawa Y, *Phys Rev Lett* ***80*** *(1998) 3936*

Klein M L and Venables J A, *Rare Gas Solids (Academic Press, 1977) ch. 10*

Klemperer O, *Proc Camb Philos Soc* ***30*** *(1934) 347*

Knights A P and Coleman P G, *Surf Science* ***367*** *(1996) 238-244*

Knudsen H and Reading J F, *Physics Report* ***212*** *(Numbers3&4) (1992) 107-222*

Kögel G, Schödbauer D, Trifthauser W and Winter J, *Phys Rev Lett* ***60*** *(1988) 1550*

Kong Y and Lynn K G, *Phys Rev B* ***41*** *(1990) 6179*

Kövér Á and Laricchia G, *Phys Rev Lett* ***80*** *(1998) 5309-5312*

Kövér Á, Paludan K and Laricchia G, *J Phys B* ***34*** *(2001) L219-L222*

Kruit P and Read F H, *J Phys E* ***16*** *(1983) 313*

Lang N D and Kohn W, *Phys Rev B* ***3*** *(1971) 1215*

Laricchia G, Charlton M, Griffith T C and Jacobsen F M, *"Positron (Electron) – Gas Scattering" eds. W E Kauppila, T S Stein and J M Wadehra (Singapore: World Scientific) (1986) 313*

Laricchia G, Charlton M, Davies S.A, Beling C D and Griffith T C,
J Phys B **20** *(1987) L99*

Laricchia G, Davies S A, Charlton M and Griffith T C, *J Phys E* **21** *(1988) 886*

Laricchia G and Zafar N. *Solid State Phenom* **28/29** *(1992) 347*

Laricchia G, and Moxom J, *Phys Lett A* **174** *(1993) 255*

Laricchia G and Charlton M, *Philos T Roy Soc A* **357** *(1999) 1259-1277*

Laricchia G, *in press, (2002) "Proceedings of the XXIIth International Conference on the Physics of Electronic and Atomic Collisions "*

Lino J L S, Germano J S E and Lima M A P. *J Phys B* **27** *(1994) 1881*

Lynn K G, Frieze W E and Schultz P J, *Phys Rev Lett* **52** *(1984) 1137*

Lynn K G, Nielsen B and Quateman J H, *App Phys Lett* **47** *(1985) 239*

Lynn K G, Gramsch E, Usmar S G and Sferlazzo P, *App Phys Lett* **55** *(1989) 87*

Lynn K G and Jacobsen F M, *Hyp Int* **89** *(1994) 19*

Madansky L and Rasetti F, *Phys Rev* **79** *(1950) 397*

McAlinden M T, MacDonald F G R S and Walters H R J,
Can J Phys **74** *(1996) 434*

Merrison J P, Charlton M, Deutch B I and Jørgenson L,
J Phys Condens Matter **4** *(1992) L207*

Mills A P JrPlatzman P M and Brown B L, *Phys Rev Lett* **41** *(1978) 1076*

Mills A P Jr, *Appl Phys* **22** *(1980) 273*

Mills A P Jr and Gullikson E M, *Appl Phys Lett* **49** *(1986) 1121*

Mil'stein A I and Khirplovich I B, *JETP* **79** *(1994) 379-383*

Mitroy J, Bromley M W J and Ryzhikh G C, *J Phys B* **32** *(1999) 2203*

Mohorovic S, *Astron Nachr* **235** *(1934) 94*

Mondal N N and Hamatsu R, *Mat Sci Forum* **363-365** *(2001) 682-685*

Mori S and Sueoka O, *J Phys B* **27***(1994) 4349*

Murkherjee T, Sur S and Ghosh A. *J Phys B* **24** *(1991) 1449*

Murkherjee T and Ghosh A S, *J Phys B* **32** *(1999) 1385-91*

Murray C A and Mills A P, *Solid State Commum* **34** *(1980) 789*

Nagashima Y, Kakimoto M, Hyodo T and Fujiwara K, *Phys Rev A* **52** *(1995) 258*

Nagashima Y, Hyodo T, Fujiwara K and Ichimura A, *J Phys B* **31** *(1998) 329*

Nieminen R M and Oliva J, *Phys Rev A* **32** *(1985) 2640*

Olsen J O, *J Phys E* **12** *(1979) 1106*

Ore A and Powell J L, *Phys Rev* ***75*** *(1949) 1696*

Özen A, Garner A J and Laricchia G, *NIMB* ***171*** *(2000) 172-177*

Özen A, *PhD Thesis* (1999) *University College London*

Palathingal J C, Asoka-Kumar P,Lynn K G, Posada and Wu X Y, *Phys Rev Lett* ***67*** *(1991) 3491*

Perkins A and Carbotte J P, *J Phys B* ***1*** *(1970) 101*

Petkov M P, Lynn K G, Roelling L O and Troev T D, *Appl Surf Sci* ***116*** *(1997)*

Phelps M E, Hoffman E J, Mullani N A and Te-Pogossian M M, *J Nucl Med* ***16*** *(1975) 210-210*

Rice-Evans P, Haynes C E, Al-Qaradawi I, El Khagni F A R, Evans H E and Smith D L, *Phys Rev B* ***46*** *(1992) 14178*

Ruark A E, *Phys Rev* ***68*** *(1945) 278*

Ryzhikh G C and Mitroy J, *Phys Rev Lett* ***79*** *(1997) 4124*

Parcell L A, McEachran R P and Stauffer A, *NIMB* ***171*** *(2000) 113*

Sarkar N K and Ghosh A S, *J Phys B* ***30*** *(1997) 4591-4597*

Schrader D M, *inSLO85 (1985) 166*

Schultz P J and Lynn H G, *Phys Rev A* ***38*** *(1988) 1866*

Seah M P, *J Electron Spectrosc Related Phenom* ***50*** *(1990) 137*

Shearer J W and Deutch M, *Phys Rev* ***76*** *(1949) 462*

Skalsey M, Engbrecht J J, Bithell R K, Vallery S and Gidley D W, *Phys Rev Lett* ***80*** *(1998) 3727*

Smith P M and Paul D A L, *Can J Phys* ***48*** *(1970) 2984*

Stein T S, Kauppila W E and Roellig L O, *Rev Sci Inst* ***45*** *(1974) 951*

Sullivan J P, Gilbert J and Surko C M, *Phys Rev Lett* ***86*** *(2001a) 1494*

Sullivan J P, Gilbert S J, Buckman S J and Surko C M, *J Phys B* ***34*** *(2001s) L467-L474*

Sullivan J P, Marler J P, Gilbert J, Buckman S J and Surko C M, *Phys Rev Lett* ***87*** *(2001c) 073201*

Sur S and Ghosh A S, *J Phys B* ***18*** *(1985) L715*

Surko C M, Passner A, Leventhal M and Wysocki F J, *Phys Rev Letts* ***61*** *(1988) 1831*

Surko C M, Leventhal M and Passner A, *Phys Rev Letts* ***62*** *(1989) 901*

Tong B Y, *Phys Rev B* **5** *(1972) 1436*

Vallarta M S and Feynman R, *Phys Rev* **55** *(1939) 506*

Van Veen A, Schut H and Mijnarends P E,
"Positron Beams and their applications" ed. P Coleman (World Scientific, 1999) p191

Varella M T N, Carvalha C R C and Lima M A,
"New Directions in Antimatter Chemistry and Physics" eds. C M Surko and F A Gianturco (Amsterdam: Kluwer) p 463

Vehanen A, Lynn K G, Schultz and Eldrup M, *Appl Phys A* **32** *(1983) 163*

Walters H R J, Blackwood J E, McAlinden M T,
"New Directions in Antimatter Chemistry and Physic" (kluiver, New York, 2001) p173

Weber M H, Tang S, Berko S, Brown B L, Canter K F and Lynn K G,
Phys Rev Letts **61** *(1988) 2542*

West R N, *Adv Phys* **22** *(1973) 263*

Weyl H, *Grouppentheorie und Quantenmechanik (1931) 2nd ed. p234*

Wheeler J A, *Ann N Y Acad Sci* **48** *(1946) 219*

Yang C N, *Phys Rev* **77** *(1950) 242*

Zafar N, Laricchia G, Chevallier J and Charlton M, *J Phys D* **22** *(1989) 868*

Zafar N, *PhD Thesis (1990) University College London*

Zafar N, Laricchia G, Charlton M and Griffith T C, *J Phys B* **24** *(1991) 4461*

Zafar N, Laricchia G, Charlton M and Griffith T C, *Hyp Int* **73** *(1992) 213*

Zafar N, Laricchia G, Charlton M and Garner A, *Phys Rev Lett* **76** *(1996) 1596*